

**SYNTHESIS AND CHARACTERIZATION OF
OXIDE NANOSTRUCTURES**

NURULAIN BINTI SAMAT

**FACULTY OF SCIENCE
UNIVERSITY OF MALAYA
KUALA LUMPUR**

2014

**SYNTHESIS AND CHARACTERIZATION OF
OXIDE NANOSTRUCTURES**

NURULAIN BINTI SAMAT

**DISSERTATION SUBMITTED IN FULFILLMENT OF
THE REQUIREMENTS FOR THE DEGREE OF
MASTER OF SCIENCE**

**DEPARTMENT OF PHYSICS
FACULTY OF SCIENCE
UNIVERSITY OF MALAYA
KUALA LUMPUR**

2014

Abstract

This dissertation presents the report on a study of synthesis and characterization of oxide nanostructures. The nanostructures of SiO₂ are synthesized using carbothermal reduction method. SiO₂NWs formed on the silicon substrate in the variation of growth temperature and deposition time for both undoped and Cu-doped SiO₂. The nanowires are then characterized by FESEM and EDX analysis. Using the same method, ZnO nanostructures are synthesized at difference growth temperature. It is found that the temperatures have changed the ZnO nanostructures from uniform crystal films to sharp ellipsoidal shape. Meanwhile, the Al-doped ZnO changed the structure into highly density ZnO nanorods. Field electron emission studies show slightly increment in the average field enhancement factor, β values if the temperature increases. The β also increases in the Al-doped ZnO nanorods. The average current did not drop when tested for about 20 minutes for all samples. ZnO nanostructures are also synthesized *via* sol gel method using *C.Aurantifolia* extracts at different concentration and pH values. The nanostructures are characterized using FESEM, XRD and PL. When the concentration of the solution increases from 0.05M to 0.20M, crystalline ZnO-NPs are fabricated. PL reveals all nanostructures emit the visible PL spectra in the range of 450-591 nm. The broad yellow band is referred to hydroxyl group, which is confirmed also in the XRD analysis. The changes in pH values also give significant effect on the formation of ZnO nanostructures. The samples show highly crystalline nanorods formed when the samples are further heated to 300°C at longer time.

Abstrak

Disertasi ini membentangkan laporan mengenai kajian sintesis dan pencirian nanostruktur oksida. Nanostruktur SiO_2 disintesis menggunakan kaedah pengurangan carbothermal. SiO_2NWs akan terbentuk pada substrat silikon jika terdapat perubahan suhu pertumbuhan dan pembedapan masa bagi kedua-dua yang tidak didop dan SiO_2 didop Cu. Nanowayar tersebut kemudian dicirikan oleh FESEM dan EDX analisis. Menggunakan kaedah yang sama, nanostruktur ZnO disintesis pada perbezaan pertumbuhan suhu. Ia didapati bahawa suhu telah menukarkan nanostruktur ZnO dari filem kristal seragam kepada ellipsoidal berbentuk tajam. Sementara itu, ZnO didop Al bertukar struktur menjadi ZnO nano rod yang berketumpatan tinggi. Bidang kajian pancaran electron menunjukkan sedikit kenaikan dalam purata nilai faktor peningkatan medan, β jika terdapat kenaikan suhu. Nilai β juga meningkat dalam ZnO nano rod yang didopkan Al. Purata arus elektrik tidak jatuh apabila diuji selama kira-kira 20 minit bagi semua sampel. Nanostruktur ZnO juga disintesis menggunakan kaedah solgel yang menggunakan ekstrak *C.Aurantifolia* pada perbezaan nilai kepekatan dan pH. Nanostruktur tersebut dicirikan menggunakan FESEM, XRD dan PL. Apabila kepekatan cecair meningkat dari 0.05M kepada 0.20M, Kristal ZnO-NPs difabrikasi. PL mendedahkan semua struktur-struktur nano memancarkan PL spektrum yang boleh dilihat dalam lingkungan 450-591 nm. Jalur kuning yang luas merujuk kepada kumpulan hidroksil, yang disahkan juga dalam analisis XRD. Perubahan dalam nilai pH juga memberi kesan yang besar terhadap pembentukan struktur-struktur nano ZnO. Sampel menunjukkan Kristal nano rod terbentuk apabila sampel ini seterusnya dipanaskan kepada 300°C dan pada masa yang lebih lama.

Acknowledgment

My foremost thanks go to my dissertation supervisor Assoc. Prof. Dr. Roslan Md.Nor. I thank him greatly with regards for his patience and encouragement that carried me on through difficult times and for his insights and suggestions that helped to shape my research skills. I owe him gratitude for having me shown this way of research especially when I came with zero and nothing. Besides of being an excellent supervisor, Dr. Roslan was as close as relative and good friend.

Many thanks and regards to few peoples who are really supportive moral or emotionally. Special thanks to beautiful lady, Ms. Nurul Rozullyah for helping me with the data and nice suggestions from time to time. I am grateful to her for being so helpful and was always available when I needed her. I wish to express my warm and sincere thanks to Mrs. Hartini, the PhD student, also my ex-senior, who always motivate me. I am delighted to have work with her during my project. I am also thankful to few research officers from Physics Department for helping me in the data collection.

I would like to express my gratitude to my family especially my parents, friends and many others, all of who gave me the possibility to complete this dissertation. In the end, I would also like to show my love and appreciations to my husband Syahmi for giving me encouragement and support during my day as student and working women.

TABLE OF CONTENT	
ORIGINAL LITERARY WORK DECLARATION	ii
ABSTRACT	iii
ABSTRAK	iv
ACKNOWLEDGMENT	v
LIST OF FIGURES	viii
LIST OF TABLES	xi
LIST OF ABBREVIATIONS	xii
1.0 INTRODUCTION	
1.1 Introduction	1
1.2 Research Objectives	3
1.3 Layout of the Thesis	4
2.0 LITERATURE REVIEW	
2.1 Introduction	5
2.2 Properties of Silicon	6
2.2.1 Introduction	6
2.2.2 Review of SiO ₂ Nanostructures.	8
2.3 Properties of Zinc Oxide	11
2.3.1 Introduction	11
2.3.2 Doping of ZnO Nanostructures	12
2.3.3 Field Emission Theory	15
2.4 Synthesis Methods of Oxide Nanostructures	
2.4.1 Introduction	20
2.4.2 Carbothermal Reduction Method	24
2.4.3 Sol-gel Method	26
2.4.4 Biosynthesis approach in nanostructured materials.	28
2.5 Summary	32
3.0 METHODOLOGY	
3.1 Introduction	34
3.2 Substrate preparation	35
3.3 Carbothermal Reduction Synthesis of SiO ₂	37
3.3.1 Cu-doped SiO ₂ nanostructures	38
3.4 Carbothermal Reduction Synthesis of ZnO	40
3.4.1 Al-doped ZnO Nanostructures	40
3.5 Sol-gel synthesis of ZnO nanostructures using Citrus Aurantifolia	41

extract	
3.5.1	Variation of Zinc Acetate concentration 41
3.5.2	Variation of Reaction Solution pH 43
3.6	Characterization Methods 44
3.6.1	Field Emission Scanning Electron Microscopy (FESEM) 44
3.6.2	X-Ray Diffraction (XRD) 47
3.6.3	Photoluminescence Microscopy (PL) 49
3.7	Field Electron Emission Properties Measurements 50
3.8	Summary 53
4.0 RESULTS AND DISCUSSIONS	
4.1	Introduction 54
4.2	Characterizations of SiO ₂ nanostructures synthesized using carbothermal reduction technique. 55
4.2.1	Morphology and structural properties of SiO ₂ Nanowires 55
4.2.2	Morphology and structural properties of Cu doped SiO ₂ Nanowires 58
4.3	Characterization of ZnO nanostructures synthesized using carbothermal reduction technique. 58
4.3.1	Morphology and structural properties of ZnO Nanostructures 60
4.3.2	Field electron emission of ZnO Nanostructures 64
4.3.3	Morphology and structural properties of Al-doped ZnO Nanostructures. 74
4.3.4	Field electron emission of Al-doped ZnO Nanostructures. 77
4.4	Characterization of ZnO nanostructures synthesized using sol-gel technique 80
4.4.1	Effect of concentrations on the fabricated ZnO nanoparticles. 81
4.4.2	Optical Properties of ZnO nanoparticles 83
4.4.3	Effect of pH values on the fabricated ZnO nanorods 86
4.5	Summary 91
5.0 CONCLUSIONS 93	
References 96	

LIST OF FIGURES

Figure 2.1	Optical fibers are made from silica.	7
Figure 2.2	The use of silicon in electronics chip and transistors.	8
Figure 2.3	Structure of SiO ₂	9
Figure 2.4	Three stages of proposed mechanism	10
Figure 2.5	Different crystal structure of ZnO.	12
Figure 2.6	Schematic diagram to show the simplified model in the Fowler-Nordheim theory. The dashed line indicates the tunneling region.	16
Figure 2.7	Two main methods of synthesis of nanomaterials.	21
Figure 2.8	Types of synthesis under liquid-phase, gas-phase and vapor-phase methods.	24
Figure 2.9	Plants used for biosynthesis of nanostructured materials.	29
Figure 2.10	Limonene's structure.	31
Figure 2.11	The common types of citrus	32
Figure 3.1	The schematic diagram of the sputter coater.	35
Figure 3.2	The plasma sputter coater and SPI control	36
Figure 3.3	The sequential steps of cleaning the substrate before coating with gold	36
Figure 3.4	Experimental set up image of Carbothermal reduction method.	37
Figure 3.5	A temperature gradient inside the furnace	37
Figure 3.6	Experimental set-up of carbothermal reduction method	38
Figure 3.7	Process of peeling the <i>Citrus</i>	41
Figure 3.8	The sequential steps with images to prepare <i>C.Aurantifolia</i> extract and preparing the precipitates.	42
Figure 3.9	The solution after addition of NaOH	43
Figure 3.10	Electrons interact with sample's atoms to produce scattered, secondary electron to form images and X-ray gives chemical composition.	46
Figure 3.11	FESEM images taken using FEI Quanta 200F.	46
Figure 3.12	Some of the uses of X-Ray diffraction.	47
Figure 3.13	The schematic diagram of the XRD	48
Figure 3.14	Schematic diagram of photoluminescence of atom from valance to conduction band.	50
Figure 3.15	Schematic of the planar diode configuration arrangement in a vacuum chamber.	52
Figure 4.1	FESEM micrographs of SiO ₂ nanowires fabricated on gold coated silicon substrate at three different temperatures (a) 900 ⁰ C, (b) 1000 ⁰ C and (c) 1100 ⁰ C. The growth time is at 2 hours.	56
Figure 4.2	The SEM images of SiO ₂ NWs fabricated on gold coated silicon substrate at (a) 1 hour and (b) 2 hours at constant temperature of 1100 ⁰ C.	57

Figure 4.3	The EDX spectrum on the SiO ₂ NWs.	58
Figure 4.4	(a) SEM image of Cu doped SiO ₂ NWs and (b) EDX analysis.	59
Figure 4.5	SEM micrographs of ZnO structures fabricated on gold coated silicon substrate at (a) 900 ^o C, (b) 1000 ^o C and (c) 1100 ^o C for 2 hrs synthesis time.	62
Figure 4.6	XRD spectrum of the as grown samples (a) 900 ^o C, (b) 1000 ^o C and (c) 1100 ^o C.	62
Figure 4.7	The field emission current density <i>J</i> on the applied electric field <i>E</i> of the samples at 900 ^o C. Inset is the F-N relationship of $\ln(J/E^2) - 1/E$ plot.	68
Figure 4.8	The field emission current density <i>J</i> on the applied electric field <i>E</i> of the samples at 1000 ^o C. Inset is the F-N relationship of $\ln(J/E^2) - 1/E$ plot.	69
Figure 4.9	The field emission current density <i>J</i> on the applied electric field <i>E</i> of the samples at 1100 ^o C. Inset is the F-N relationship of $\ln(J/E^2) - 1/E$ plot.	70
Figure 4.10	Time dependence of the emission current of ZnO nanostructures at constant applied voltage and temperature 900 ^o C.	71
Figure 4.11	Time dependence of the emission current of ZnO nanostructures at constant applied voltage and temperature 1000 ^o C.	72
Figure 4.12	Time dependence of the emission current of ZnO nanostructures at constant applied voltage and temperature 1100 ^o C.	73
Figure 4.13	FESEM micrograph of Al doped ZnO nanorods synthesized at 1100 ^o C for 2 hours.	75
Figure 4.14	EDX analysis of Al doped ZnO nanorods synthesized at 1100 ^o C for 2 hours.	75
Figure 4.15	XRD pattern of Al doped ZnO microstructures.	76
Figure 4.16	The field-emission current density (<i>J</i>) of the Al-doped ZnO nanorods as the function of the applied field (<i>E</i>). Inset is the corresponding F-N curve	79
Figure 4.17	FESEM images of ZnO particles using Zinc acetate at concentrations of (a) 0.05 M, (b) 0.10 M and (c) 0.15 M (d) 0.20 M synthesized at 90 ^o C for 2 hours.	82
Figure 4.18	XRD pattern of ZnO nanoparticles.	83
Figure 4.19	PL spectra in the yellow green region fitted to Gaussian curves for samples synthesized using Zn acetate dehydrate at concentration of a) 0.05M, b) 0.10M, c) 0.15M and d) 0.20M.	84
Figure 4.20	FESEM images of unheated ZnO nanostructures synthesized at (a) pH=5.0 and (b) pH=7.0 and (c) pH=9.0 synthesized at 90 ^o C for 2 hours. The samples were dried at 100 ^o C for 6 hours.	87
Figure 4.21	XRD patterns of unheated ZnO nanostructures synthesized at	88

	pH=7.0 and pH=9.0 at 90 °C for 2 hours.	
Figure 4.22	The FESEM images of ZnO nanorods using Zinc acetate at (a) pH=5.0 and (b) pH=7.0 and (c) pH=9.0 synthesized at 90 °C for 2 hours. The samples were further heated at 300 °C on the magnetic plate for over 6 hours.	89
Figure 4.23	XRD pattern of ZnO nanorods	90

LIST OF TABLES

Table 2.1	Some physical properties of silicon.	7
Table 2.2	Some physical properties of ZnO	11
Table 2.3	Synthesis of metal nanostructures by different plants.	29
Table 3.1	SiO ₂ nanostructures synthesized at different temperature and growth time.	39
Table 4.1:	List of X-ray diffraction peaks of ZnO nanostructures synthesized at 900 ⁰ C, 1000 ⁰ C and 1100 ⁰ C for 2 hours.	63
Table 4.2	Comparison of electric field (E) versus current density (J) for different temperature	67
Table 4.3	Field enhancement factors, β of ZnO nanostructures at different temperatures.	67
Table 4.4	Turn on field and field enhancement factor values from literature.	67
Table 4.5	List of X-ray diffraction peaks of rod-like ZnO synthesized at 1100 ⁰ C for 2 hours.	76
Table 4.6	The PL peaks for ZnO samples synthesized at different zinc acetate concentration.	85

LIST OF ABBREVIATIONS

GaN	Gallium Nitride
SiO ₂	Silicon Oxide
ZnO	Zinc Oxide
CuO	Copper oxide
TiO	Titanium oxide
FESEM	Field Emission Scanning Electron Microscopy
EDX	Energy Dispersed X-ray Spectroscopy
XRD	X-ray Diffractometer
PL	Photoluminescence
FEE	Field Electron Emission (FEE)
Zn(OH) ₂	Zinc hydroxide
NWs	Nanowires
C	Carbon
O	Oxygen
CO	Carbon monoxide
SiC	Silicon carbide
Si	Silicon
H	Hydrogen
SiH ₄	Silane
VLS	Vapor-liquid-solid
Si ₂ H ₆	Disilane
FHD	Flame hydrolysis deposition
Au	Gold
Al	Aluminum
Li	Lithium
K	Potassium
Na	Sodium
Cu	Copper
Ag	Silver
In	Indium
Sn	Tin
GaAs	Gallium Arsenide
AAO	Anodic aluminum oxide
CNT	Carbon nanotubes
VLS	Vapor-liquid-solid
VS	Vapor-solid
WO ₃	Tungsten trioxide
Mo	Molybdenum
KOH	Potassium hydroxide
CTAB	Cetyltrimethylammonium bromide
TiC	Titanium carbide
Ar	Argon
MnO ₂	Manganese dioxide

ZrO ₂	Zirconium oxide
NaOH	Sodium hydroxide
AgNWs	Silver nanowires
H ₂ O ₂	Hydrogen peroxide
CVD	Chemical vapour deposition
PLD	Pulse laser deposition
HF	Hydrfluoric acid
ITO	Indium tin oxide

CHAPTER 1 INTRODUCTION

1.1 Introduction

Today, nanotechnology is operating in various field of science via its operation for materials and devices using different techniques at nanometer scale. Among all various kinds of nanomaterials, ZnO and SiO₂ received highly interest among researches besides other materials such as GaN, CuO and TiO. Therefore this thesis concentrates on the investigations of ZnO and SiO₂ nanostructures by carbothermal reduction methods and ZnO nanoparticles using *C.Aurantifolia* extracts.

This thesis is organized as follows. Chapter one will highlight the main objectives of this study. Thus, it will also describe the overall overview for the other chapters. In chapter two, several reviews on ZnO and SiO₂ nanostructures will be highlighted. These include recent study on ZnO and SiO₂ nanowires, doping of ZnO and SiO₂ nanowires, field emission theory and recent study towards ZnO material. On the last part of chapter two, several synthesis methods of oxide nanostructures will be given.

Then, in chapter three, experimental details are given step by step, including detail discussions of ZnO and SiO₂ growth by carbothermal reduction method and ZnO growth using sol gel process. In short descriptions, ZnO are an attractive material for short wavelength optoelectronic applications owing to its wide band gap 3.37 eV, large bond strength and large exciton binding energy (60 meV) at room temperature. As a wide band gap material, ZnO is used in solid state blue to ultraviolet (UV) optoelectronics including laser developments. Chapter three also includes descriptions of characterization methods used. In carbothermal reduction route, the properties of the nanowires have been varied by

changing the deposition temperatures and deposition time. While in sol gel method, the properties of ZnO nanoparticles have been changed by varying the concentration of initial solution and pH values. Due to its vast areas of applications, various synthetic methods have been employed to grow variety of ZnO nanostructures including nanoparticles, nanowires, nanorods, and other complex morphologies. As mentioned in chapter two, nanoparticle synthesis can be possible via liquid, gaseous, and solid media, but due to several advantages over the other methods biological (liquid) methods are receiving more interest due to their low cost, reliability and environmentally friendly synthetic route. In general, nanoparticles with high surface-to-volume ratio are needed, but the agglomerations of small particles precipitated are the main concern even in the absence of any stabilizer. With all the issues related to nanoparticles, until today, metal nanoparticles, metal oxide nanoparticles and polymer nanoparticles still in current research effort. Most preferentially, among metal oxide nanoparticles, zinc oxide (ZnO) nanoparticles have their own important due to their vast area of applications such as gas sensor, chemical sensor, bio-sensor, optical and electrical devices. Thus, due to the concern towards environmentally approach, this thesis will for the first time contribute a simple sol gel method using *C.Aurantifolia* extracts to grow ZnO nanoparticles. Chapter Three also includes brief descriptions of the instruments, which are used in the laboratory for the synthesis and characterizations of oxide nanostructures.

The thesis is followed by chapter results and discussion. In that Chapter Four, all results are examined using field emission scanning electron microscopy (FESEM) equipped with electron dispersive x-ray (EDX), X-ray diffractometer (XRD), photoluminescence (PL) and field electron emission (FEE). The undoped and Cu-doped SiO₂NWs has been studied using FESEM and EDX analysis. Also, the results of ZnO nanostructures from both

methods are presented in this chapter. In the carbothermal reduction method, it was found that the morphologies of ZnO nanostructures change from uniform crystal film to ellipsoidal nanorods when the deposition temperature increases. The turn on field values does not give so much difference, which is in the range of 40-44 V/ μm and the average field enhancement factor shows the increment in the value.

An interesting green synthesis method has been developed for the preparation of ZnO nanoparticles. This preparatory method is a novel and cost effective method that excludes the use of external stabilizing/capping agents. In the sol gel process, the results of ZnO nanoparticles using *C.Aurantifolia* extracts are presented. It was found, the ZnO nanoparticles are more observable when the concentration of Zn in citrus is increased but the XRD analysis revealed the possibility of Zn(OH)_2 still exist. While the photoluminescence detected the peaks in the range of 450-590 nm occurred. On the other hand, the pH values of the initial solutions are also investigated. Still, the XRD pattern showed the possibility of Zn(OH)_2 exist at pH=7 and pH=9. Afterwards, the samples were re-do, and all samples were further heated at 300 °C on magnetic plate. The FESEM showed crystalline nanorods formed at higher aspect ratio with no characteristics diffraction peaks from other phases or impurities were detected.

1.2 Research objectives

This study has three main objectives:

- a) To investigate the morphologies and structural properties of SiO_2 and ZnO nanostructures by carbothermal reductions method.

- b) To study the field electron emission of doped and undoped ZnO nanostructures by carbothermal reductions method.
- c) To investigate the morphologies and structural properties of ZnO nanostructures by *C.Aurantifolia* extracts, which is fabricated by sol gel process.

1.3 Layout of The Thesis

This dissertation has five main topics. The introduction topic is the overall story of the projects. It includes the objectives of the research. Chapter Two provides the previous studies and literature relevant to the topic. It will focus on the previous studies on SiO₂ and ZnO nanostructures. It also includes recent publication about ZnO nanostructures using biosynthetic approaches mainly in plant extracts. The topic is followed by Chapter Three which is the methods used to synthesis the nanostructures. It will highlight two main synthesis methods, carbothermal reduction of SiO₂ and ZnO nanostructures. Also, Sol gel process of ZnO nanostructures using *C.Aurantifolia* (lime) extracts. In this chapter, all the changes in parameters will be explained in details. Meanwhile, in Chapter Four, all the results will be presented and discussed. The last section, Chapter Five will provide the summary of the research study and possibility of the future work that can be continued.

CHAPTER 2 LITERITURE REVIEW

2.1 Introduction

Oxide nanostructures have attracted much attention because they are fascinating functional materials. The unique properties of the oxide nanostructures, make them suitable for a wide variety of applications, including gas sensors, light-emitting diodes, field emitters, supercapacitors, nanoelectronics, and nanogenerators. As the number of scaled-down components being developed gradually increases, it is apparent that high-quality wide-bandgap one-dimensional (1D) semiconductor nanostructures such as nanowires (NWs) [1-3], nanotubes [4-5] and nano-ribbons [6] will most likely become promising functional components. Therefore, various physical and chemical deposition techniques and growth mechanisms are exploited and developed to control the morphology, shape, size, crystal structure, defects, and stoichiometry of oxide nanostructures to derive benefits for specific application. In this chapter, a comprehensive review of recent developments in novel synthesis and exceptional characteristics of one-dimensional nanostructures of silicon oxides and zinc oxides will be presented. There are three sections, beginning with discussions on the properties of silicon as the most abundance element on earth. Several recent studies about silicon and silicon oxides will be reviewed. The next section will be focused on the ZnO material, which received tremendous interest among researchers due to its novel properties. The latest study of several ZnO-doped nanostructures will be discussed. Synthesis methods of oxide nanostructures also play an important role in making the growth of nanostructures become more elegant. Thus, the last section of this chapter will review several common synthesis methods of nanostructures. The section will focus on two main methods; sol gel processing and carbothermal synthesis. Additionally, the sol gel

process will have supplementary review on the biosynthetic route due to the highly demand in green technology.

2.2 Properties of Silicon

2.2.1 Introduction

Silicon is a nonmetallic, gray, semiconducting element with atomic number 14 and mass 28.086 g/mole. Silicon is one of the most abundant elements in the earth and it exists as oxides and silicates. It is very important semiconducting material due to its atomic structure. Doping with an element like boron, one silicon atom substituted with this element in the crystal structure, but it provides one less valence electron than silicon. Therefore one valence electron of silicon can shift to that hole. Due to that shifting, extrinsic conduction becomes possible. Semiconductors with this type of doping are referred to as p-type semiconductors [7-8]. There is normally no need to make silicon in laboratory as it is readily available commercially. Silicon is readily available through the treatment of silica SiO_2 with pure graphite in an electric furnace.



Under these conditions, SiC can form. However, provided the amount of SiO_2 is kept high, silicon carbide maybe eliminated.



Very pure silicon can be made by the reaction of SiCl_4 with hydrogen, followed by zone refining of the resultant silicon.



Some physical properties of silicon are given in Table 2.1. As a semiconductor, silicon is most widely used among other semiconductors, due to its unique advantages. It is easy to

control the composition of elemental silicon and its conduction properties. A large variety of impurity atoms can be used to modify the composition and conduction properties of silicon. In addition, silicon can be used at relatively high temperatures without losing its conduction characteristics.

Table 2.1: Some physical properties of silicon.

Density at 300 K	2.329 g/cm ³
Specific heat (300 K)	0.713 J g ⁻¹ K ⁻¹
Thermal expansion (300 K)	2.6 × 10 ⁻⁶ K ⁻¹
Thermal conductivity (300 K)	1.5 W cm ⁻¹ K ⁻¹
Melting point	1687 K
Boiling point	3504 K
Band gap (300 K)	1.126 eV
Latent heat of fusion	50.66 kJ/mol
Heat of evaporation	385 kJ/mol

Silicon dioxide is also known as silica with the chemical formula of SiO₂. It is most commonly found in nature as sand or quartz, and is the major compound in sandstone. The sand on a beach is made mostly of silicon dioxide. The used of silica are primarily found in the production of glass to make windows or beverage bottles. Figure 2.1 shows the fiber optic bundles that are made from silica.



Figure 2.1: Optical fibers are made from silica.

Portion of silicon that is used for the semiconductor industry is small. This is due to the small scale of parts in electronic industry. However, its technical importance is crucial. Silicon is widely used in electronics industry due to excellent electronic properties. Mass production of electronic chips and photovoltaic cells are almost based on silicon. There are other uses in solid state electronics such as in production of transistors, liquid crystal displays, diodes, etc. In addition to these, silicon carbide is widely used as an abrasive material. The compounds of silicon with a metal, which is called as silicides, can be used for different applications.

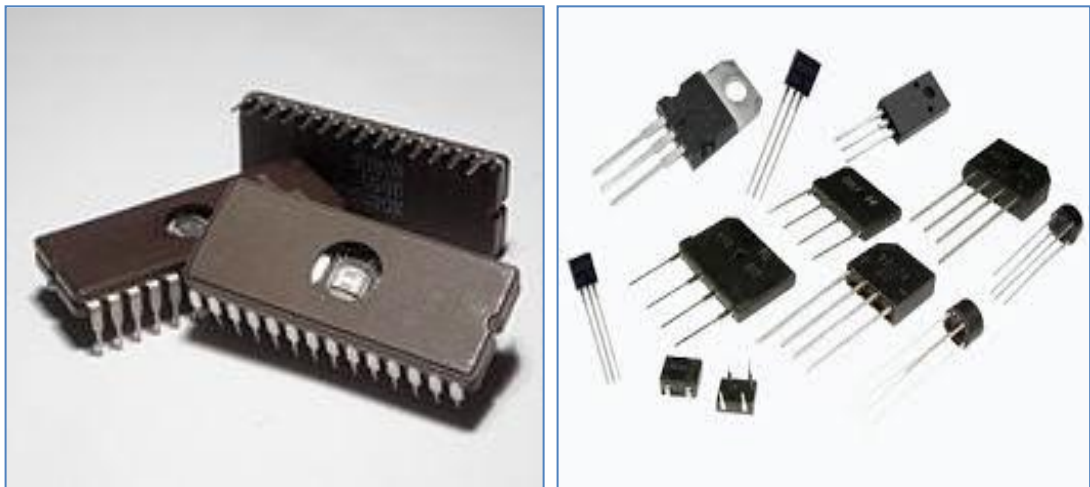


Figure 2.2: The use of silicon in electronics chip and transistors.

2.2.2 Review of SiO₂ nanostructures.

In the chemical structure of silicon dioxide, silicon does not form double bond with oxygen. There are various structures for silicon dioxide. One of them is shown in Figure 2.3. Each silicon atom is covalently bonded to four oxygen atoms. Each oxygen atom is covalently bonded to two silicon atoms. This means that, overall; the ratio is two oxygen atoms to each silicon atom, giving the formula SiO_2 .

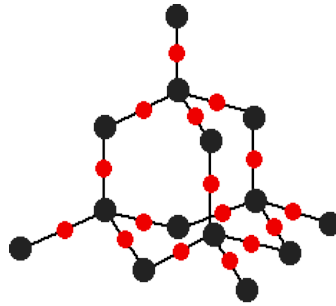


Figure 2.3: Structure of SiO_2

Silicon oxide nanowires are attracting great attention due to their intense and stable blue light emission at room temperature. It is an electrically insulating material. Silicon oxide nanowires can be synthesized using various methods including heating silicon wafers under high temperature [9] and thermal evaporation of silicon based powder, such as Si, SiO_2 , SiC and their mixtures. Some other works done includes the presence of catalysts such as Au and transition metal [10-11]. Zheng *et.al* [12] studied gallium-catalyzed silicon oxide with SiO and silane (SiH_4) as silicon source via VLS process. The as grown products tend to assemble with different morphologies such as comet-like and carrot-like in different growth temperature. Other popular Si source in the SiO_2 nanostructures is disilane (Si_2H_6). The characteristics of silicon oxide film were studied using plasma enhanced chemical vapor deposition [13]. Another successful highly aligned vertical silicon oxide nanowires was fabricated without any additional source of silicon. The effect of annealing temperature

and time was studied [14]. While, Zhang *et.al* [15] was successfully demonstrated high quality SiO₂ using flame hydrolysis deposition (FHD) method which proves FHD is an excellent technology applied in planar optical waveguides. However, thermal annealing is the simplest method for the amorphous SiO_x nanowires growth. During the thermal annealing, a thin layer of gold on the silicon substrate is heated at high temperature (~1000 °C) in the presence of inert gas environment. At this temperature, some amount of gold diffuses into the silicon substrate. This reduces the density of gold nanoparticles on the Si surface and is resulted into a low density of amorphous SiO_x nanowires [16]. To enhance the nanowire density, the gold diffusion into the Si substrate must be retarded. The gold diffusion into the Si substrate can either be retarded by reducing the growth temperature or by inserting a barrier layer in the Au/Si substrate layer system. Figure 2.4 shows the general process or procedure of the proposed mechanism.

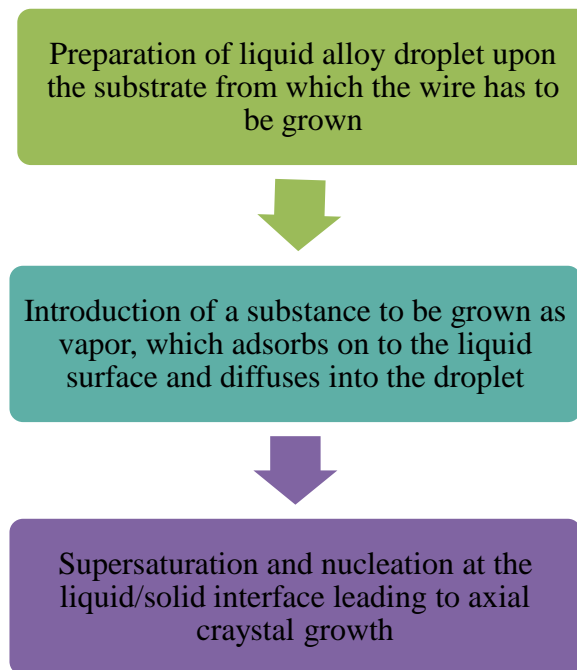


Figure 2.4: Three stages of proposed mechanism

2.3 Properties of Zinc Oxide

2.3.1 Introduction

Partial lists of the properties of ZnO are shown in Table 2.2. ZnO is a very promising material for semiconductor device applications. It has a direct and wide band gap. The band gap of ZnO is 3.44 eV at low temperatures and 3.37 eV at room temperature [17]. For comparison, the respective values for wurtzite GaN are 3.50 eV and 3.44 eV [18]. Compare with GaN (25 meV) and ZnSe (22meV), the free-exciton binding energy in ZnO is 60 meV [19-20]. This large exciton binding energy indicates that efficient excitonic emission in ZnO can persist at room temperature and higher [19] and the large exciton binding energy makes ZnO a promising material for optical devices that are based on excitonic effects. In piezoelectric materials, an applied voltage generates a deformation in the crystal and vice versa. These materials are generally used as sensors and transducers. Piezoelectric ZnO films with uniform thickness have been grown on variety of substrates using different deposition techniques, including sol-gel processing, spray pyrolysis, chemical vapor deposition, molecular beam epitaxy and sputtering [21-24]. Due to a strong luminescence in the green-white region, ZnO is also a suitable material for phosphor applications. The n-type conductivity of ZnO makes it appropriate for applications in vacuum fluorescent displays and field emission displays.

Table 2.2: Some physical properties of ZnO

Molecular mass	81.389 g/mole
Specific heat (300 K)	$0.713 \text{ J g}^{-1} \text{ K}^{-1}$
Thermal conductivity	$0.54 \text{ W cm}^{-1} \text{ K}^{-1}$
Melting point	2250 K
Band gap energy at room temperature	3.37 eV
Exciton binding energy	60 meV

ZnO has a crystal structure of wurtzite (B4), zinc blend (B3) and rock salt (B1). The structures are shown in Figure 2.5. Generally, ZnO are composed of alternate layers of zinc and oxygen atoms disposed in wurtzite hexagonal closed-packed structure with a longitudinal axis (c-axis). In this crystal structure, both zinc and oxygen ions are coordinated with four ions of the opposite charge, and the binding is strong ionic type.

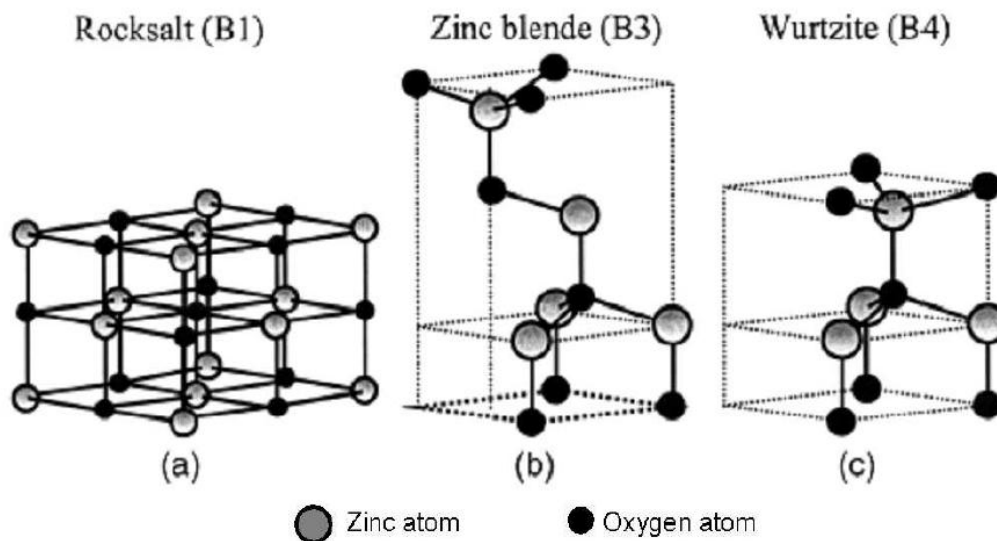


Figure 2.5: Different crystal structure of ZnO.

2.3.2 Doping of ZnO Nanostructures.

As early as the 1960s [25], synthesis of ZnO nanostructures was an active field because of applications in sensors, transducers and as photocatalysts. With reduction in size, novel electrical, mechanical, chemical and optical properties are introduced resulting from surface and quantum confinement effects. Doping in semiconductor with selective elements offers an effective approach to adjust the electronic (p-type or n-type), optical, and magnetic

properties, which is crucial for practical applications. But, one of the common problems with doped nanostructures is that the introduction of dopant during growth often results in the change of morphology. Morphological difference between the undoped and Cd-doped ZnO nanostructures is presented by Liu and coworkers [26]. Under different growth condition, the undoped ZnO products could be pure nanowires, pure nanobelts and microcombs. While the Cd-doped ZnO nanostructures were nanowires with small amount of nanobelts appeared on the substrate. Zinc oxide nanofibers doped with aluminum oxide were prepared by sol-gel processing and electrospinning techniques [27]. The average diameters of the nanofibers were found to decrease with the increase of aluminum (Al^{3+}) content in the precursor solution. Oriented low dimensional ZnO nanostructures were fabricated on Si and Al substrates by hydrothermal route at 95 °C without any surfactant [28]. On Si substrate, aligned ZnO nanorods were perpendicularly grown and ZnO nanoplates were formed on Al substrate. Another problem in doping ZnO semiconductor is the accurate determination of electronic properties, so that many of the studies of doped ZnO are confined to the effect of dopant on the optical properties. The prospect of using ZnO as a complement or alternative to GaN in optoelectronics has motivated many research groups worldwide to focus on its semiconductor properties, trying to control the unintentional n-type conductivity and to achieve p-type conductivity. Therefore, understanding the native point defects (i.e. vacancies, interstitials, and antisites) and the incorporation of impurities is the key toward controlling the conductivity in ZnO.

Obtaining p-type doping in ZnO has proved to be a very difficult task. The two strong reasons make it difficult are because ZnO has a tendency toward n-type conductivity and another one is the fact that there are very few candidate shallow acceptors in ZnO [29]. Elements like Li, Na and K are compensating towards p-types conductivity. While elements like Cu, Ag and Au do not contribute to p-type conductivity because they are classified

under deep acceptors. Quite a few research groups have reported observing p-type conductivity in ZnO. Na-doped ZnO nanowires with an average diameter of 40 nm have been fabricated by a thermal calcination method. The nanowires prepared here exhibited excellent photocatalytic activity for organic pollutants in water, which also showed their potential application in wastewater treatment [29]. Co-doping to achieve p-type conductivity has also been proposed. Chen and coworkers [30] reveal the diffraction angle of Co-doped ZnO is closest to that of undoped ZnO. Another promising candidate for p-type doping in ZnO is arsenic. Since arsenic contained defect complexes, it can form shallow acceptor levels. As:ZnO nanowires have also been reported and their optical properties have been studied [31]. The result shows a feasibility of doping of ZnO nanowires with arsenic by post-annealing treatment of nanowires grown on GaAs substrate, as in the case of As-doped *p*-type ZnO thin films reported elsewhere. While nitrogen was commonly regarded as a relatively better choice, which was also confirmed theoretically [32]. Unfortunately, the efficiency of the p-type doping as well as the quality of the nitrogen-doped film still remained an obstacle to the development of ZnO.

On the other hand, common n-type dopants in ZnO are group-III elements such as Ga, Al, In as Zn substitution and group-VII elements as O substitution. For a long time, it has been postulated that the unintentional n-type conductivity in ZnO is caused by the presence of oxygen vacancies or zinc interstitials [33]. Undoped and In-doped ZnO thin films were deposited by the spray pyrolysis method at 450 °C substrate temperature. The indium contents give significant effect on the surface thin film. While the electrical characteristics showed In-doped ZnO thin film is suitable for the solar cell applications [33]. The effect of Sn concentration on the optical properties of ZnO thin films was studied by Chahmat and coworkers [34]. They proved that the Sn:ZnO thin films have an excellent transparency in the visible region. While the optical gap is reduced with increased in Sn/Zn doping ratio.

The high conversion efficiency of nanostructured ZnO films based on Al-doped crystallites [35, 36] triggered investigations of novel synthesis techniques for fabrication of nanocrystalline ZnO for efficient solar cells. Thus, it has been demonstrated that doping results in changes in conductivity of ZnO nanostructures and that the introduction of various dopants frequently had an effect on the optical properties. However, it is often difficult to establish whether the observed changes are a consequence of the introduction of an impurity or simply a consequence of the change in native defect densities which can occur with the doping.

2.3.3 Field Emission Theory

In this sub-chapter, an account of development in theory of field emission, basic methodology; and a brief review of the recent field emission studies reported in the literature will be presented. The materials of interest from field emission point of view are carbon nanotubes, graphene, nanomaterials of wide band gap such as SiC, GaN, ZnO and other semiconductors such as Si.

In the phenomenon called field emission, electrons tunnel out from metal or semiconductor surface into the vacuum under the action of high electrostatic field which is approximately 10^6 V/cm to 10^7 V/cm. The quantum mechanical tunneling emission current – field strength relation was derived by Fowler and Nordheim in the year 1928 [37]. Apart from the usefulness of field emission in surface science, field emission sources are routinely used in scanning electron microscopy and electron beam lithography because of their small optical size. In fact, a high density two dimensional array of emitters can be fabricated by a variety of techniques into emitters suitable for flat panel displays and for electron tube devices [38].

The basic formulation of quantum mechanical tunnelling of conduction electrons from a plane metal surface into vacuum was conceived by Fowler and Nordheim [37]. In the case of the semiconductors, the field electron emission theory is complex. Various aspects such as the contribution of the effective electron mass, field penetration, surface states, doping with n type or p type impurities and band structure have to be taken into account.

In early 1962, *Stratton* [39] who first deals with field emission from semiconductor considered the effect of the field penetration and surface states on electron emission. He pointed out that the field emission characteristic dominated by the surface states should be strongly temperature dependent while that dominated by field penetration is not. In 1971, *Baskin et. al* [40] have analysed field electron emission behaviour of an n-type semiconductor based on the field emission from conduction band. Recently, there have been efforts to revisit the theory of Fowler-Nordheim tunneling. The standard theory has been reformulated by *Forbes and Deane* [41] leading to an insight into linearity of F-N plot. In this theory, the system is simplified as a one-dimensional structure along the direction of the external field. The emission tip is modelled as a semi-infinite quantum well with the work function of ϕ , and the local electric field (F) is approximated as a linear potential (Figure 2.6).

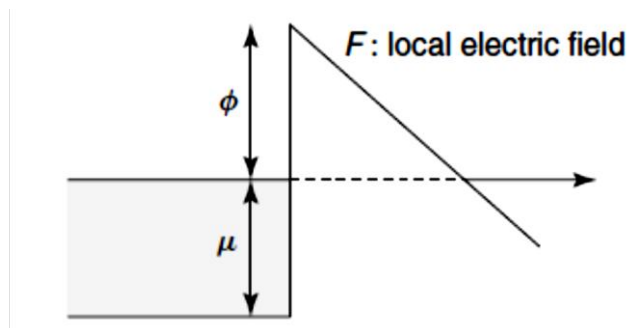


Figure 2.6: Schematic diagram to show the simplified model in the Fowler-Nordheim theory. The dashed line indicates the tunneling region.

In the case of nanometrials, the F-N theory primarily considers tunneling of electrons from flat planar surface of metals. The following FN equation was applied:

$$J = A \left(\frac{\beta^2 E^2}{\phi} \right) \exp \left(\frac{-B \phi^{3/2}}{\beta E} \right) \quad (2.4)$$

A and B are constants with values of $1.5 \times 10^{-10} \text{ A/V}^2/\text{eV}$ and $6.83 \times 10^3 \text{ V/eV}^{3/2}/\mu\text{m}$, respectively. J is the emission current density and ϕ is the work function of the field material. The electric field E is the local electric field (surface field). The electric field (applied or macroscopic field) between the cathode and the anode separated by a distance d with a potential difference V is given by,

$$\mathbf{F} = \frac{V}{d} \quad (2.5)$$

However, local electric field \mathbf{F} at the surface of a nanoparticle can be much higher than \mathbf{E} by a factor, β ,

$$\mathbf{E} = \beta \mathbf{F} \quad (2.6)$$

Here, β is the field enhancement factor. The factor β is related to the emitter geometry. The emission performance of an emitter can be enhanced by increasing the ‘aspect ratio’, where for the elongated, cylindrical emitters the height to diameter (thickness) ratio is called the ‘aspect ratio’. The value of β can be calculated from the slope of the F-N plot, but the value obtained may be physically unrealistic. For the nanotubes, β typically ranges between hundreds and thousands [42]. Many of the field emission studies on nanomaterials have been motivated from the electron sources point of view. Therefore, the current stability for

a long duration operation, the effect of residual gas pressure, effect of adsorption and desorption causing local work function variations become important parameters [42].

An excellent account of early work on carbon based film emitters and other nanostructured heterogeneous materials and also hypotheses about emission mechanism have been reported by Forbes [43]. Recently a detailed analytical treatment of field emission from nanowall emitter has been attempted by Qin *et. al* [44]. The theory is very complex. The authors have shown that the F-N equation will not describe the electron emission from a nanowall of very small width (less than $\approx 2\text{nm}$).

Carbon nanotubes (CNT) were grown in anodic aluminum oxide (AAO) and used as field emitters in a triode structure was successfully fabricated by Lin *et.al*. Field-emission characteristics of the CNT emitters have been studied and an anode turn-on electric field of $\sim 8.05 \text{ V}/\mu\text{m}$ was measured [45]. The field emission capability of zinc oxide nanorods made by a new hydrothermal synthesis have been studied Chen *et. al* [46]. The field enhancement factor β is 2510. The low maximum current density is tentatively ascribed to a low emission site density. Future work is necessary to determine whether the resistivity of the ZnO-nanorods or the contact resistance between nanorods and cathode substrate is the important properties on controlling the emission current density. The areal density of emitters on a cathode surface plays an important role in controlling the local electric field at the surface of an emitter. Higher density leads to a screening effect and density reduces this screening and causes rise in the local field at each emitter. These were agreed by Zhang *et. al* where they studied field emission property of ZnO nanoneedle arrays with different morphology. All the samples exhibited FE behavior compatible with the FN theory. A clear relation between the morphology and the FE performance was observed which demonstrates the tip shape of the nanoneedles is important for determining the FE properties [47].

Nanowires of different materials are of immense interest due to their one dimensional structures. Such structures are known to show quantum confinement effects. In particular, nanowires with low threshold and low operating voltage have become potential candidates for field emission display (FED) application. Aligned nanowires with a high packing density can significantly enhance the field emission behaviour. Final aim is to form regular array of nanowires with a good uniformity in their aspect ratio (length to radius). ZnO nanowires with hexagonal wurtzite structure have been grown on zinc foil by using a simple evaporation thermal method [48]. The turn-on voltage for ZnO nanowires was found to be about $9.1\text{V}/\mu\text{m}$ at a current density of $0.001\ \mu\text{A}/\text{cm}^2$. In this study, the author noted that the length distribution of the nanowires is not uniform with respect to their heights; therefore it is very difficult to determine the areas that are really responsible for the field emission. Another study reported field emission measurement of the tapered ZnO nanowires arrays fabricated by the electrochemical self-assembly technique [49]. The screening effect caused by major length variation in nanowires has direct impact on the emission current. It reduces the field enhancement factor and thus also reduces the emission current density.

The F-N behaviour of nanomaterials is important from the basic point of view. However, field emission from nanomaterials has been very attractive field of research due to its technological importance. The current density obtainable for lower and lower turn-on voltage, stability of the current, and life are the main considerations of the study. Ease of synthesis, size and shape, electrical conductivity are also important consideration for a material to be a candidate as an emitter. Finally, ease of fabrication of array of emitters on lithographically patterned substrate decides the applicability of such sources in electronic devices. Obtaining sharp and robust materials capable of delivering high emission current densities at lower operating voltages is still an on-going effort.

2.4 Synthesis Methods of Oxide Nanostructures.

2.4.1 Introduction

Oxide nanostructures can be grown in a variety of morphologies and by a number of different methods. It can be well accomplished by two main approaches: top down and bottom up. Top down approach refers to slicing or successive cutting of bulk material to get nanosized particles. While bottom up approach refers to method where small building blocks are produced and assemble into larger structure. Milling and lithography is a typical top down method. Recently, aligned ZnO nanorods were fabricated by interference lithography [50]. The enhancements in optical properties are considered very useful for manufacturing a wide variety of highly efficient low cost optoelectronic devices. Regardless of the surface imperfections and other defects that top down approaches may introduce, with slightly modifications, they will continue to play an important role in the synthesis and fabrication of nanostructures and nanomaterials.

These technical approaches can also be grouped according to the growth media. Figure 2.7 shows the two main media that are commonly describe among researches. They are vapor phase growth and liquid (solution) phase growth. Vapor phase techniques are governing by vapor-liquid-solid (VLS) and vapor-solid (VS) mechanisms. On the other hand, solutions-phase growth methods provide more flexible synthesis process and an alternative to achieve lower cost. Although there are numbers of techniques to grow

nanostructures, this section will focus on two main routes which is sol-gel and carbothermal reduction routes. The other methods will be explained briefly.

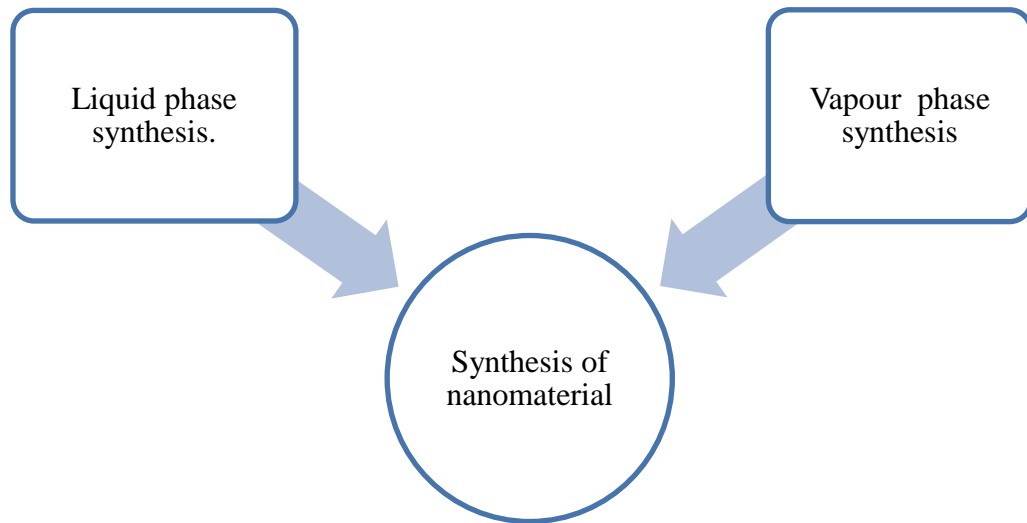


Figure 2.7: Two main methods of synthesis of nanomaterials.

Figure 2.8 list several examples of liquid phase and vapour phase synthesis. One useful way of classifying vapour-phase synthesis is by using solid precursors. One of the methods using solid precursors are pulse laser ablation [51]. Among researchers, laser ablation is believed to be an effective way for fabricating various doped nanocrystal. Even though this method can generally only produce small amount of nanoparticles, but it can vaporize materials that cannot readily be evaporated. Cu doping of ZnO quantum dots (QDs) was carried out by laser ablation. A large amount of Cu doped ZnO QDs were produced with ultrafine size, good dispersibility and high quality [52]. Some other recent example includes the field emission properties of ZnO nanostructures deposited by pulse laser ablation source in silicon substrate [53]. In this study, for a given laser wavelength, the samples grown at 10^{-6} mBar have higher enhancement factors than the samples grown at 10^{-2} mBar. Various

morphologies of nano and microstructures were obtained for laser wavelengths of 1064 and 355 nm.

Another popular method under vapour-phase synthesis is ion sputtering. Sputtering is the process of using ions to knock atoms or molecules out from a target. Although there are more sputtering process developed, the fundamental of sputtering process are more or less the same. In other study, ZnO thin films have been deposited on Si (100) substrates by ion beam sputtering at room temperature [54]. However, the sputtering process may have few drawbacks and these lead to several modifications to enhance the deposition process. For example, magnetic field has been introduced into sputtering process to increase the growth species in the vapour phase. Such sputtering refers to as magnetron sputtering. Another vapour phase method is spray pyrolysis. However, this technique is very less described among researches. The process can be described as converting micro-sized liquid droplets of precursor or precursor mixture into solid particles through heating. ZnS thin films were prepared by chemical spray pyrolysis [55]. The results presented the formation of thin film conditions have a significant influence on absorption and the PL spectra. The aim of this work was to study the structural and optical properties of ZnS films deposited by spray pyrolysis for application as an antireflective coating in solar cells. The effects of the initial solution on the chemical composition and optical properties were examined by optical spectroscopy. In other study, compact nanocrystalline WO₃ thin films with different concentrations of Mo doping were successfully fabricated [56]. The results revealed Mo has modified their crystallinity, crystallite size, and optical band gap which are suitable in photonics application in future.

Liquid phase synthesis also received high attention among researches. Some of the methods under liquid phase synthesis provide advantages at the first stage such as low cost and synthesized at low temperature. There are several types of liquid phase synthesis.

Among them are co-precipitation, sol-gel processing, micro-emulsions, hydrothermal/solvo-thermal synthesis, microwave synthesis and template synthesis.

Cu-doped ZnO nanopowder has been synthesized by co-precipitation method [57]. The PL study showed the strong UV and weak green bands emphasized that the Cu-doped ZnO has good crystal surface. While hydrogenated samples have good crystalline structure and better optical properties which are suitable for the fabrication of nano-optoelectronic devices such as tunable light emitting diode. Meng *et.al* [58] studied Zn hollow spheres composed of interconnected nanosheets with high porosity fabricated by co-precipitation method. The sensor prepared has high gas-sensing response and short response time at 350 °C implying the potential of practical applications.

Another popular liquid phase synthesis is hydrothermal (water used as solvent) or solvothermal (other solvents) synthesis. Although these two techniques are considered quite popular to synthesize oxide nanostructures, there are several considerations needed to be concerned. Hydrothermal experiments require facilities that must operate routinely and reliably under extreme pressure temperature conditions. Often, hydrothermal process consists of the use of autoclave, reactor or pressure vessel. One should consider when dealing with autoclave, several characteristics should be considered. The autoclave should be easily assembled and disassembled. Other than that, it should be rugged enough to bear high pressure and temperature experiments for long periods with no damage. The other characteristics of autoclave or reactor are its corrosion resistance in the pressure temperature range in a given solvent or hydrothermal fluid. Instead of solvothermal, hydrothermal synthesis received much attention and studies among researchers especially to grow oxide nanostructures. Many works have been reported to synthesize ZnO nanorods by using wet chemical hydrothermal approaches [59-61]. Spindle-like ZnO were successfully synthesized using hydrothermal using KOH as reactants [62]. The results

indicated that the concentration of starter solution has an important effect on the particles morphology and higher concentration of precursor led to smaller particles. Cationic surfactant cetyltrimethylammonium bromide (CTAB) has been used to get ZnO nanorods in a narrow size distribution. The growth process CTAB could serve as a carrier for negative zincate and organize the landing process [63]. Cationic surfactant cetyltrimethylammonium bromide (CTAB), which has been generally used as templating micelle molecule to synthesize mesoporous materials [64-66], is introduced to hydrothermal process to favor the erosion of zinc and control the morphology of ZnO crystals. Comparative experiments show that it is capable of favoring the erosion reaction and inducing the orientation growth of the resultant metal oxide nano-crystals.

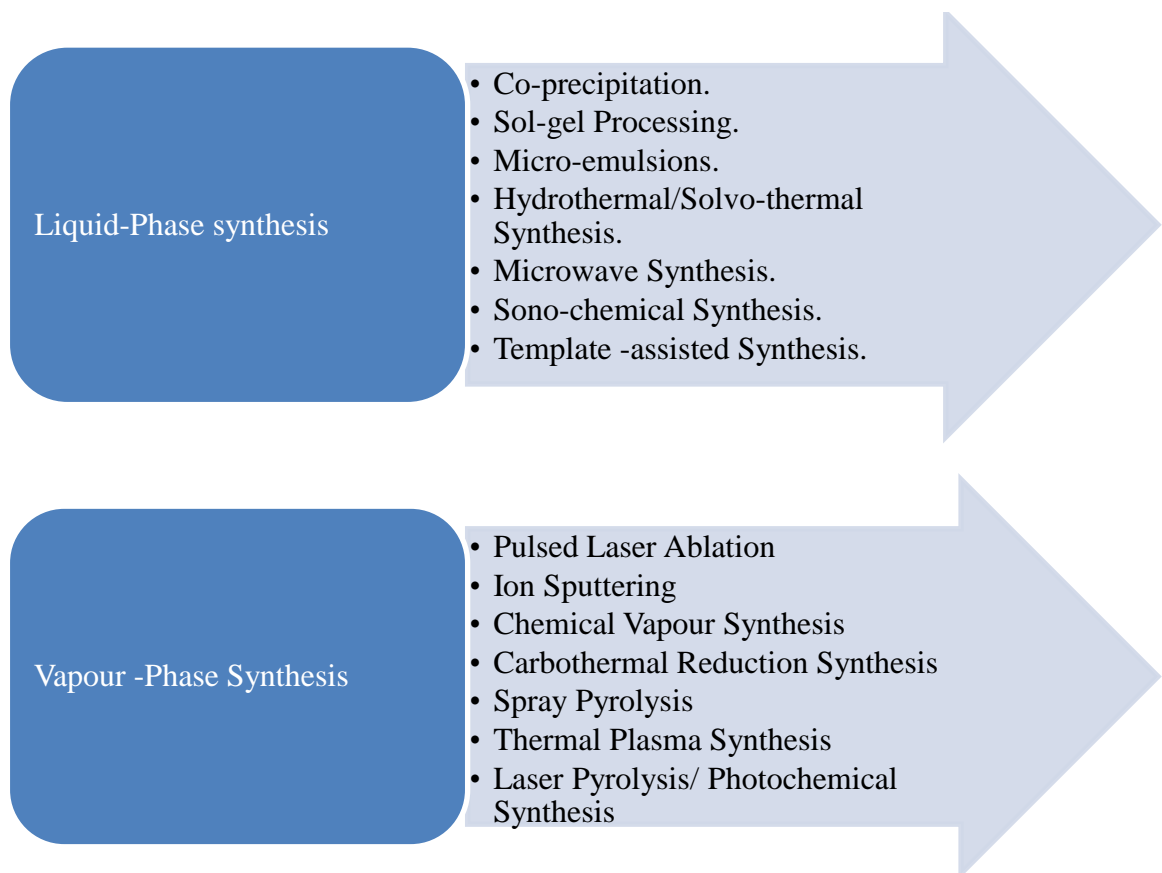


Figure 2.8: Types of synthesis under liquid-phase, gas-phase and vapor-phase methods.

2.4.2 Carbothermal Reduction Method

In this section, a simple method to synthesize most of the 1-D nanostructures will be presented. In the reaction, carbon help to form oxides species, usually containing some sub-oxides in the vapor phase, which then transform to the final products. This method has the advantages of simplicity, rapidity and low cost [67]. Many researches focus on formation of SiC [68] and TiC [69] using carbothermal reduction methods. Only few explained about SiO₂ and ZnO nanostructures.

The carbothermal synthesis of carbides, oxycarbides, carbonitrides and nitrides represents a current field of interest in materials research of ceramics and hard materials.

In the conventional carbothermal reduction process, metal catalysts are generally required for the formation of 1-D nanostructures by the vapor-liquid-solid (VLS) mechanism. In the case of silicon, the nanostructures are grown by dissolution of silicon and carbon carrying vapors in the liquid droplets, which normally formed by an addition of metal sources such as gold. The dissolved silicon and carbon atoms diffuse in metal droplet and then formed precipitation at the desired plane. Sometimes the use of catalysts increases the number of processing step which creates contamination inside the grown nanostructures. For the synthesis of SiO₂ amorphous nanowires, the growth mechanism is proposed here [70]:



At first, the reaction of SiO₂ powder with carbon will form SiO gas. The SiO gas will then accumulates gradually and aggregates to form SiO₂ nanowires as below:



While in the case of ZnO nanostructures using carbothermal synthesis, the mixture of ZnO and carbon powder will be heated up to a reaction temperature, ZnO(s) powder can be reduced into Zn (g) by C (s) through solid–solid reaction [71]. The vaporized Zn (g) can be

deposited on a substrate, resulting in ZnO nanostructure. Modified carbothermal reduction method to synthesize great quantities of ZnO nanowires was studied [72]. The synthesis was done at atmospheric temperature without any catalyst. The result showed that the calculated band gap was about 3.36 eV with length and diameter about 1.8 μm and 33.8 nm respectively. The simple carbothermal synthesis of aligned ZnO nanorods was studied on silicon substrate with polycrystalline ZnO films [73]. It was considered that the ZnO films could offer the nuclei for formation of the nanostructures so that the aligned ZnO could be achieved.

To tailor the properties of ZnO nanostructures, several doping elements have been used and reported in the literature, generally by using vapor phase growth or intentionally by using carbothermal method. There are few reports the growth of Sb doped ZnO nanowires [74, 75]. Recently, the Sb-doped ZnO nanowires were synthesized by using Sb as a catalyst on a sandwich type substrate by carbothermal evaporation method [76]. The strong exciton emission and weak deep-level emission from room temperature PL indicates that such nanowires are of better optical quality than pure ZnO nanowires. In other work, In-doped ZnO nanodisks with a hexagon were grown at 1000 $^{\circ}\text{C}$ in flowing Ar via carbothermal reduction [77]. Furnace cooling in conjunction with introducing a small amount of O_2 , around 1.0%, into flowing Ar during growth significantly enhanced the UV emission of ZnO nanodisks because of reduction of oxygen vacancies and surface defects. Another created challenge among researches is to enhance the carbothermal reduction by using other carbon source rather than graphite. Some of the other carbon sources are graphite, nanotube, carbon black and carbon nanoparticle.

2.4.3 Sol-gel Method

Sol-gel is one of the most commonly selected methods for the synthesis of ZnO nanoparticles because this method produces good homogeneity and optical properties and has easy composition control, low processing temperatures, the ability to coat large areas, and low equipment costs [78, 79]. This technique is considered as a wet chemical route for the synthesis of colloidal dispersions. From such colloidal dispersions, several types of nanostructures can be readily prepared. In general, sol-gel process is associated with a gel composed of sol particles. As the first step, colloidal (sol) suspension of the desired particles is prepared from the solution of precursor molecules. With an appropriate deposition time, sol particles can fill the channels and form structures with high aspect ratio. The final product will be obtained after a thermal treatment to remove the gel. Although the fabrication of different forms of final products requires some specific considerations, the fundamentals and general approaches in the synthesis of colloidal dispersions are the same. MnO₂ [80], ZrO₂ [81], TiO₂ [82], and various multi-compound oxide nanorods [83, 84] had been synthesized based on similar processes. The solution pH is one of the important factors influencing the ZnO properties when ZnO is synthesized by sol-gel. The pH affects the hydrolysis and condensation behavior of the solution during gel formation and therefore influences the morphology of the ZnO. Alias *et. al* [78] studied the influence of pH values on the ZnO powder using sol-gel method. The samples prepared at pH 6 and 7 have no intense ZnO peak. This is because of the high concentration of H⁺ ions and low concentration of OH⁻ ions in the solution. For the neutral condition at pH 7, the number of H⁺ ions reacting with number of OH⁻ from NaOH is equivalent. The ZnO powder peaks for samples with pH \geq 8 show the crystalline nature. The results were comparable with the FESEM images. Another study has synthesized ZnO nanoparticles

using sol gel method by controlling the molar ratio of starting materials, the pH of reactants and the calcinations temperatures [78]. In this study, the control of particle size, morphology and optical properties of the synthesized ZnO nanoparticles could be achieved by optimizing the process parameter conditions. By a careful control of solution preparation and processing, monodispersed nanoparticles of various oxides, including complex oxides, organic inorganic hybrids, and biomaterials, can be synthesized.

2.4.4 Biosynthesis Approach in Nanostructured Materials.

A variety of chemical and physical procedures have been used to synthesize metal nanostructures. Although these methods could be used effectively to produce metal nanostructures, they entail of expensive input, toxic solvents and hazardous chemicals.

Therefore, there is increasing need to develop a reliable, nontoxic, cost-effective and eco-friendly approach. Biological approach is timely a promising approach to synthesize metal nanostructures. Therefore, this special review delivers an overview on the biosynthesis of metal nanostructures mainly by plants. Figure 2.9 shows some of the popular plants used in biomaterials. The current application and prospects of biological synthesis of metal nanostructures are also presented. Biosynthetic method employing plant extracts, compared with microorganisms, has received much attention in recent years. This is because, it is a simple and viable alternative to chemical procedures and physical methods by synthesizing metal nanoparticles. Jose-Yacaman *et al.* firstly reported the formation of gold (Au-NPs) and silver nanoparticles (Ag-NPs) by living plants [85, 86]. While Sastry *et al.* reported biosynthesis of metal nanoparticles by plant leaf extracts and their potential applications in several studies [87-89].



Figure 2.9: Plants used for biosynthesis of nanostructured materials.

Compared to the extravagant process of maintaining cell cultures, using plants for synthesis of metal nanostructures have more advantages, such as low cost, easily available, easy to scale-up, non-pathogenic, etc. Several recent researches on biosynthesis of metal nanostructures using plants are summarized in Table 2.3.

Table 2.3: Synthesis of metal nanostructures by different plants.

<i>Plant</i>	<i>Nanomaterials</i>	<i>References</i>
<i>Alfalfa</i>	Zn	Canizal <i>et al.</i> [90]
<i>Aloe vera</i>	Au, Ag	Chandran <i>et al.</i> [91]
<i>Lemongrass</i>	Au	Singh <i>et al.</i> [92]
<i>Soybeans</i>	Au	Shukla <i>et al.</i> [93]
<i>Neem</i>	Au, Ag	Anuradha <i>et al.</i> [94,95]
<i>Cumin</i>	Au	Sneha <i>et al.</i> [96]

Compared to chemical methods, biological method is possibly at a better level to achieve shape control. Recently, Lin *et al.* discovered the silver nanowires (AgNWs) with diameters

in the range of 50-60 nm and the extract of the *Cassia fistula* leaf as reduction and capping agent. The reaction temperature played an important role in the formation of AgNWs, a low temperature was favourable in the formation of AgNWs [97]. Nano-silver particles and spherical shapes were synthesized using *Vitex negundo* leaf extract [98]. The plant plays an important role in the reduction and stabilization of silver to silver nanoparticles. Thus, should be explored further for antimicrobial applications. Another popular plant that received highly interest recently is *Citrus*. This kind of plant comes in many types; the best known examples are the oranges, lemons, grapefruits and limes. Although these plants originated from Southeast Asia [99], the United States and Brazil are the major producers of *Citrus* fruits. *Citrus Microcarpa* is well known as limau kesturi in Malaysia has been widely used for food and beverage purposes. There are many bioactive compounds have been reported from *Citrus* fruits. Thus, Lee *et.al* studied antimicrobial property isolated from the crude extract of *Citrus microcarpa* and its suitability as an antimicrobial agent for aquaculture use [100]. Another type of *Citrus* is *Citrus Aurantifolia*. Loizzo *et.al* studied the replacement of synthetic antioxidants by safe natural using *C. aurantifolia* peel and leaves. The findings of this study suggest a potential use of *C. aurantifolia* peel and leaves for supplements for human health [101]. The main constituents in the extracted citrus are limonene. The structure of limonene is shown in Figure 2.10. Experimentation has shown that only minimal quantities of limonene can be extracted from the white pith of citrus. It is colorless liquid, common in cosmetic products and as a renewably based solvent in cleaning products. Figure 2.11 shows the common types of citrus used in biosynthesis as described previously.

Since biological approach in the synthesis of metal nanostructures has achieved a considerable progress, researchers begin to explore the potential applications of the biogenetical nanostructures. In general, nanostructures application in catalysis, biosensors,

antibacterial effects and medicine depends essentially on the size and shape of the nanostructures. The sensitivity and performance of biosensors have been improved by using nanostructures. Wang *et al.* obtained two kind of Se nanomaterial with high surface-to-volume ratio, good adhesive ability and biocompatibility, and the nanomaterial have been used as enhancing and settled materials for H_2O_2 biosensor [102]. The obtained sensor exhibits good electrocatalytic activity towards the reduction of H_2O_2 due to the good adhesive ability and biocompatibility of Se nanomaterials. The bioreduction method using plants extract for the fabrication of supported metal nanoparticles has been developed during the last few years. Vilchis *et al.* reported the “one-step” bioreduction of synthetic method using *sinensis* extract for the preparation of Au and AgAu catalysts supported on $\text{SiO}_2\text{-Al}_2\text{O}_3$ material [103].

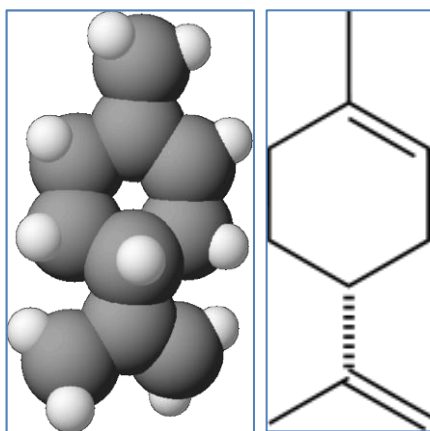


Figure 2.10: Limonene's structure.



Figure 2.11: The common types of citrus fruits

Nevertheless, in order to explore the scale-up biosynthesis of metal nanostructures, there is still a long and hopeful way to march on. Morphology- controlled fabrication of nanostructures has become one of the most important and challenging aspects of modern nanotechnology, a wide range of nanoparticle morphology have been successfully achieved by chemical approach. However, as a newly developing approach, the morphology - controlled fabrication of nanostructure by biological approach still needs much more efforts. Although, the biological approach has already attracted much attention, this area still needs a systematic and oriented research. In a word, the use microorganisms and plants in the biosynthesis of metal nanostructures is a new and eco-friendly area of research with considerable potential for green development. Especially, the elucidation of the mechanism of biosynthesis of metal nanostructures is a very promising area of research.

2.5 Summary

In summary, these reviews described partial studies on oxide nanostructures focusing on silicon and zinc oxide semiconductors. Several recent studies about silicon and silicon oxides have been reviewed. The applications of silicon have been widely proved from medical applications, cookware as well as insulation. The next section described ZnO nanomaterial, which received tremendous interest among researchers due to its novel properties. The latest studies of several ZnO-doped nanostructures have been discussed.

Lastly, this chapter ended with the review on several common synthesis methods of nanostructures focusing on two main synthesis methods which were sol gel processing and carbothermal reduction method. Some of the recent studies on biosynthetic approaches have been discussed. Focus given more towards biosynthesis using plants.

Chapter 3.0 Methodology

3.1 Introduction

Various methods have been reported to produce SiO₂ and ZnO nanostructures. These include chemical vapour deposition (CVD) [104], DC electrochemical deposition [49], thermal evaporation [105], magnetron sputtering [106], pulse laser deposition (PLD) [107] and laser ablation [108]. However, most of these methods involve high cost starting materials use, complicated equipment and low-yield of products which limit their industrial applications. Some of these growth techniques, such as PLD can be used to deposit films and device structures only on the small wafer sizes, up to 1 inch in diameter. While, the solution phase methods like hydrothermal [109] and sol-gel [79] have gained much interest due to their cost effectiveness and flexibility.

In this work, carbothermal reduction method used to growth SiO₂ and ZnO nanostructures and the sol-gel method for the synthesis of ZnO will be presented. The substrate preparation will be presented first, which includes the process of sputtering catalyst gold over the substrate. It is followed by the details discussion of carbothermal reduction method to fabricate SiO₂ and ZnO nanostructures.

For synthesis of ZnO nanostructures using the sol-gel method, biosynthesis process has been investigated as a new way for the production of nanostructures. These biological methods are currently gaining importance because they are eco-friendly, cost effective and do not involve the use of any toxic chemicals for the synthesis of nanoparticles [110]. In the sol gel section, the new synthesis method of ZnO nanoparticles using *C.Aurantifolia* extracts utilizing zinc acetate dehydrate solution at different concentrations and pH values will be presented.

3.2 Substrate preparation

Figure 3.3 illustrates the cleaning process steps for the substrate preparation. Substrates of n-type Si (100) with resistivity of $5.15 \Omega \cdot \text{cm}^{-2}$ were cut into approximately 1 cm x 1 cm in size and it was subjected to standard cleaning prior to process delivery. Then, they were ultrasonically cleaned in acetone for 10 minutes and then immersed in hydrofluoric acid for another 10 minutes to remove protective oxide layers. These substrates were ultrasonically cleaned again in acetone, rinsed with running distilled water and dried in air at room temperature. After that, cleaned substrates were coated with gold for all experiments using a plasma sputter coater. The sputtering variables kept are 2 Torr pressure and the deposition time was maintained at 20 s. This gave a gold layer of about 5 μm . The schematic diagram of the plasma sputter coater is shown in Figure 3.1 and the typical image is shown in Figure 3.2

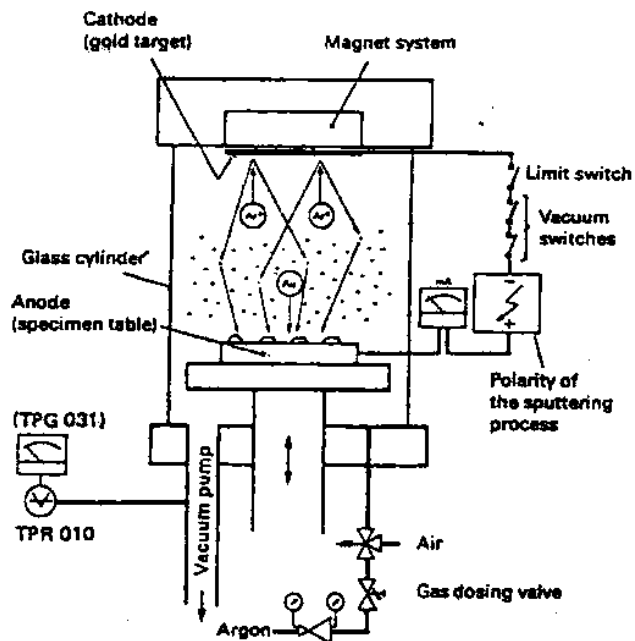


Figure 3.1: The schematic diagram of the sputter coater.



Figure 3.2: The plasma sputter coater and SPI control

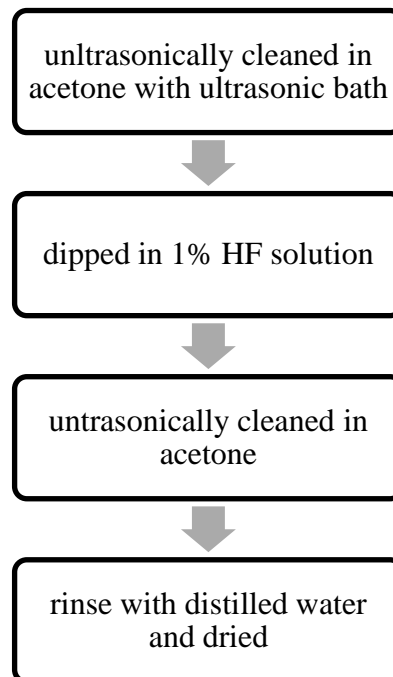


Figure 3.3: The sequential steps of cleaning the substrate before coating with gold.

3.3 Carbothermal Reduction Synthesis of SiO₂

The image of the experimental set-up is shown in Figure 3.4. Carbothermal reduction method was conducted in a tube furnace system with maximum heating capacity of 1200 °C to evaporate the materials needed to be in vapor phase as growth species to accomplish the synthesis process. The temperature of the substrates region may have to be lower than the source location due to the temperature gradient inside the furnace as shown in Figure 3.5.



Figure 3.4: Experimental set up image of Carbothermal reduction method.

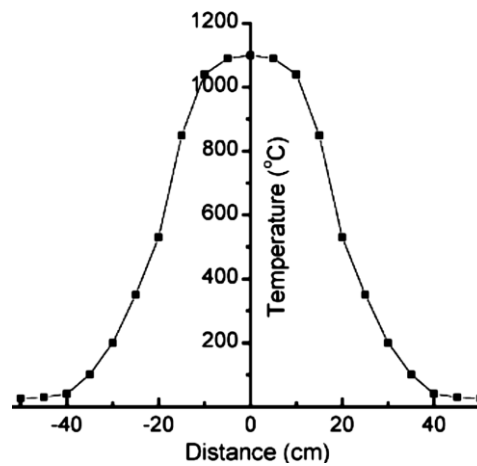


Figure 3.5: A temperature gradient inside the furnace

In the synthesis of silicon oxide nanostructures, SiO₂ powder (0.5 g) and graphite powder (0.5 g) all greater than 99% purity and with 1:1 ratio were mixed together. The source material was loaded into an alumina boat and placed in the centre of horizontal tube furnace. The substrates were horizontally arranged on the back side of another alumina boat. It was placed adjacent to the source material with a distance of 2.5 cm as shown in Figure 3.6. The tube furnace was sealed and heated up to a designated temperature at a heating rate 20 °C min⁻¹ without any carrier gas. The whole system was maintained at the desired growth time and then was cooled down to room temperature. The as-synthesized products were carefully taken out from the furnace and kept before characterized. Experiments were carried with parametric variations of experimental conditions as shown in Table 3.1. When the synthesis temperature was varied three times: 900°C, 1000°C and 1100°C, the synthesis time was maintained at 2 hours. On the other hand, when the growth time was set to be at 1 hour and 2 hours, the temperature and heating rate were set at 1100°C and 20 °Cmin⁻¹ respectively. The composition of the chemicals remained the same throughout the process.

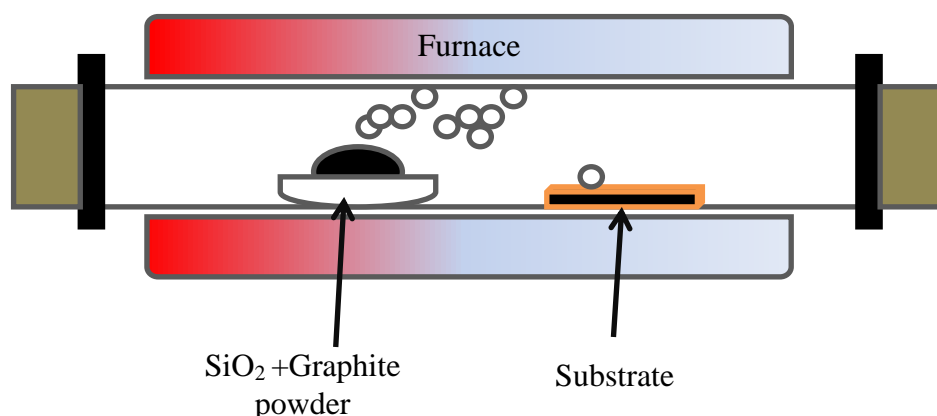


Figure 3.6: Experimental set-up of carbothermal reduction method.

Table 3.1: SiO₂ nanostructures synthesized at different temperature and growth time.

Sample (SiO ₂ +C)	Synthesis temperature / °C (growth time=2hr)
Sample 1	900
Sample 2	1000
Sample 3	1100

Sample (SiO ₂ +C)	Synthesis time (temperature=1100°C)
Sample 1	1 hrs
Sample 2	2 hrs

3.3.1 Cu-doped SiO₂ Nanostructures

In the process of doping SiO₂ nanostructures, 0.1g Cu powder (99%) was used in the mixture of SiO₂ (0.5 g) and carbon (0.5 g). The process of carbothermal reduction route is the same as mentioned in section 3.3. The experiment was performed at one parameter, where the sample was synthesized at 1100°C for 2 hours while the heating rate remained 20 °C min⁻¹ without carrier gas. The sample was allowed to cool at room temperature before characterized.

3.4 Carbothermal Reduction Synthesis of ZnO

The carbothermal reduction of ZnO nanostructures contained a mixture of high purity zinc oxide (99.999%) and graphite powder with (1:1) ratio. The 2g of the ZnO + C mixture was ground for about 10 minutes to increase the homogeneity of the mixture before being loaded evenly in an alumina boat. The boat was pushed exactly to the center of furnace. The Au-coated silicon substrate was placed at the back side of another alumina boat. The gold film acted as catalyst in the reaction. Then, the substrate was placed 2.5 cm away from the source material. The experimental set up of carbothermal reduction of ZnO nanostructures was similar in Figure 3.6. The tube furnace was sealed carefully and screwed tightly. There is no additional carrier gas in the process. Then, the furnace was heated to three different temperatures; 900°C, 1000°C and 1100°C at a heating rate 20 °C min⁻¹. After reaction for 2 hours, the as-grown samples were taken out and kept at room temperature before characterized.

3.4.1 Al-doped ZnO nanostructures.

In the synthesis of Al-doped ZnO nanostructures, 0.1g of Al₂O₃ (99.95%) was used in the mixture of ZnO (1.0g) and carbon (1.0g). The process of carbothermal reduction is the same as in section 3.4. The sample was synthesized at 1100°C for 2 hours while the heating rate remained 20 °C min⁻¹ without carrier gas.

3.5 Sol-gel synthesis of ZnO nanostructures using *Citrus Aurantifolia* extract

3.5.1 Variation of Zinc Acetate concentration

Figure 3.8 summarizes the sequential steps of sol-gel synthesis of ZnO nanostructures using *C. Aurantifolia*. ZnO nanostructures were synthesized by the sol-gel process using *C.Aurantifolia* extract. The *C. Aurantifolia* fruits obtained from the local market were peeled and the pulps were sliced into small pieces and blended in deionized water as in Figure 3.7. The blended pulps were then filtered using muslin cloth to remove solid particles. The liquid obtained was further filtered using syringe filter with a pore size of 200 nm.



Figure 3.7: Process of peeling the *Citrus*.

In the study on the effect of the variation of concentrations to synthesis ZnO nanostructures, the ZnO solution were prepared by adding zinc acetate dehydrate ($\text{Zn}(\text{CH}_3\text{COO})_2 \cdot 2\text{H}_2\text{O}$; purity=99.99%) to 100mL of the filtered *C.Aurantifolia* liquid extracts. The concentrations were varied from 0.05M to 0.20 M. The solutions were heated at 90°C under continuous stirring for 2 hours until a clear solution without turbidity was obtained. For enhancing the reactivity and homogeneity of the reacting solutions, a mechanical stirrer was used. The pH of the solution was ~3.0. After stirring completed, all the samples were

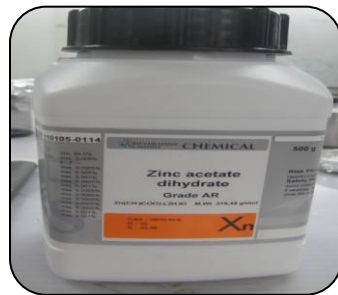
left for 24 hours to allow the reaction process to complete after which wet white precipitates were recovered, thoroughly rinsed in deionized water and dried at 100°C for 6 hours.



C. Aurantifolia –was peeled and sliced
→blended in DI water



- filtered using syringe.
- Prepared 100 mL of liquid extract.



Zinc acetate was dissolved at concentrations of 0.05-0.20M



- heated to 90°C under continuous stirring for 2 h.
- The precipitates were dried at 100°C for 6 h.

Figure 3.8: The sequential steps with images to prepare *C.Aurantifolia* extract and preparing the precipitates.

3.5.2 Variation of Reaction Solution pH

In the synthesis of ZnO nanostructures using *C.Aurantifolia* extracts, the variation of pH values were controlled by adding different amount of NaOH. Using 100 mL of *C.Aurantifolia* solution, 0.2 M Zinc acetate dehydrate, $Zn(CH_3COO)_2 \cdot 2H_2O$ was dissolved in the solution. The addition of NaOH (purity=99.99%) drop by drop changed the pH values of the solution from 5 (acidic condition) to 9 (alkaline condition). The solution transformed into a milky white slurry solution as shown in Figure 3.9. The resulting product was heated at 90°C under continuous stirring for 2 hours. All samples were left for 24 hours to allow the sol-gel. The wet white precipitates were recovered, thoroughly rinsed in deionized water and dried at 100°C for 6 hours.



Figure 3.9: The solution after addition of NaOH

3.6 Characterization Methods

The samples obtained were characterized using field emission scanning electron microscopy (FESEM), energy dispersed X-ray spectroscopy (EDX), X-Ray diffraction (XRD), Field emission electron (FEE). The optical properties were studied using photoluminescence spectroscopy (PL).

3.6.1 Field Emission Scanning Electron Microscopy (FESEM)

Historically, the first scanning microscope was using electrons to demonstrate a resolution higher than a light microscope [111]. Because this early instrument was somewhat difficult to focus and form images too slowly to permit easy evaluation of the specimen, it was unable to compete with contemporary, conventional transmission electron microscopes (TEMs) and was abandoned. In nanotechnology, electron microscopy has strongly driven the development, with demands not only for increasing resolution but also for more information from the sample.

Scanning Electron Microscopy (SEM) is an electron microscope which can produce images of a sample surface with high resolution. It is useful for judging the surface structure of the sample as well as the composition [112]. In a typical SEM, electrons are emitted from the cathode and accelerated towards the anode. Then, the electron beam is focused by lens and as the beam strikes the surface, a large number of signals are generated from (or through) the surface in the form of electrons or photons. These signals emitted from the specimen are collected by detectors to form images and the images are displayed on a cathode ray tube screen.

There are three types of images produced in SEM:

- ✓ Secondary electron (SE) - it is considered to be the electrons resulted from inelastic scattering with atomic electrons and with energy less than 50 eV.
- ✓ Backscattered electron (BSE) – it is considered to be the electrons resulted from elastic scattering with the atomic nucleus and with energy greater than 50 eV.
- ✓ X-ray photons – it occurs after the primary electron beam collides with an atom in the specimen and ejects a core electron from the atom, the excited atom then decays to its ground state and emit a characteristic X-Ray photon.

Figure 3.10 shows a schematic diagram of electrons interact with sample's atoms to produce scattered, secondary electron to form images and X-ray gives chemical composition. An image of the sample can be generated from secondary and backscattered electrons. Scanning electron microscopes are often coupled with X-ray analyzer e.g energy dispersive X-ray spectrometer (EDX or EDS). The X-ray generated will be used to characterize the elements present in the sample.

In this study, the FEI Quanta 200F (FESEM) was used to capture and magnify the sample images operated at 20 kV. The FESEM resolution is at high vacuum and the vacuum used is up to 20 Torr. The ZnO and SiO₂ nanostructures composition and structure were characterized using the FESEM attached with an EDX. Some of the images or pictures taken in this work are presented in Figure 3.11 below.

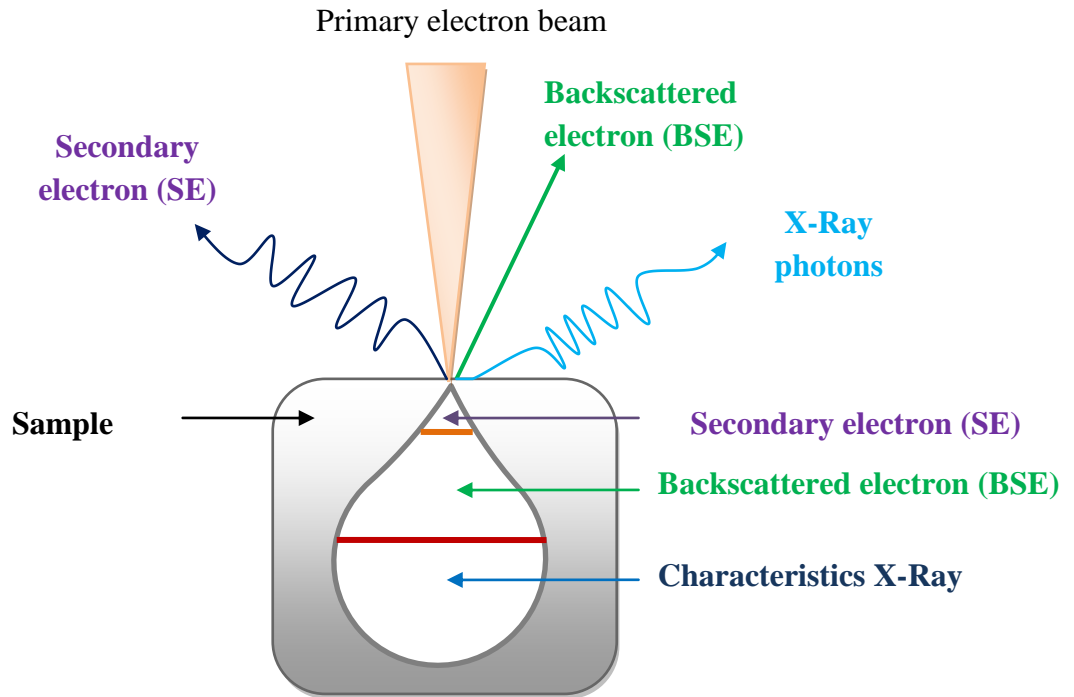


Figure 3.10: Electrons interact with sample's atoms to produce scattered, secondary electron to form images and X-ray gives chemical composition.

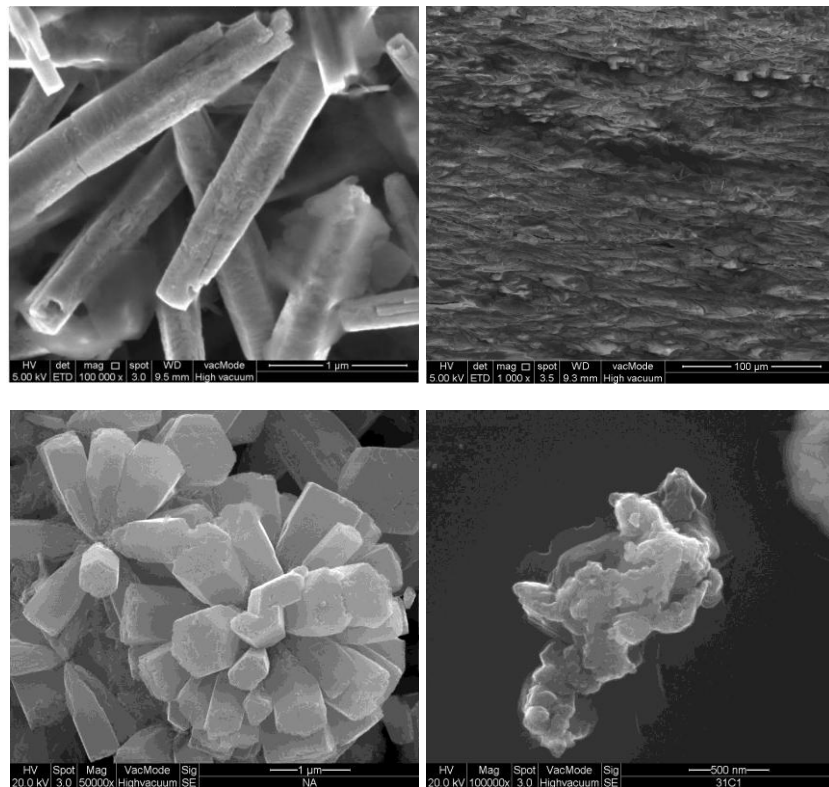


Figure 3.11: FESEM images taken using FEI Quanta 200F.

3.6.2 X-Ray diffraction (XRD)

X-ray diffraction (XRD) is non-contact and nondestructive technique which can be used to determine the crystalline phases present in materials, the structural properties of materials, the thickness of thin films and atomic arrangement of amorphous materials. Figure 3.12 states some of the uses of XRD. One important use of x-ray powder diffractometry is for identifying unknown crystals in a sample. The idea is to match the positions and the intensities of the peaks in the observed diffraction pattern to a known pattern of peaks from a standard sample or from a calculation. There should be a one-to-one correspondence between the observed peaks and the indexed peaks in the candidate diffraction pattern.

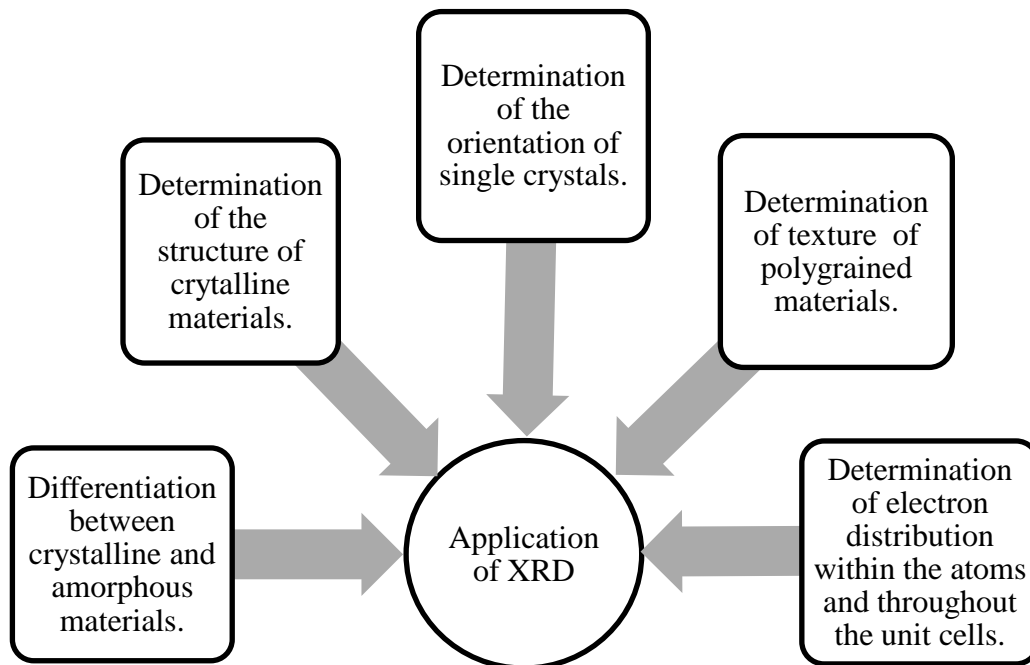


Figure 3.12: Some of the uses of X-Ray diffraction.

In XRD, the electron beams strike the metal target and X-rays are generated. The X-rays are incident on a specimen in an angle θ , if the specimen is crystalline and the distance between the atoms is of the same magnitude as the wavelength of the X-rays, diffraction will occur. The intensity of diffracted X-rays is measured as a function of the diffraction angle, 2θ and the orientation of the specimen. The diffraction pattern is used to determine the crystalline phases and structural properties of the specimen according to Bragg's Law: $n\lambda = 2d\sin\theta$, where λ is wavelength, d is atomic spacing and θ is characteristic angle. If the wavelength is known (depend on the type of x-ray tube used) and the angle can be measured (with camera or diffractometer), the interplanar distance can be calculated from the Bragg's equation. So the reciprocal lattice of the crystal can be directly mapped. In this present work, Siemens D5000 diffractometer was used. It measures the atomic spacing in crystal using diffraction of approximately monochromatic x-radiation. It can be used to characterize solid samples ranging in size from about 1 millimetre square up to four-inch wafer. The radiation used is Cu- K_{α} radiation with a wavelength of 1.5418 \AA from 10° - 80° at a scanning rate of $4^{\circ}/\text{min}$. Figure 3.13 shows the simple schematic diagram of the XRD.

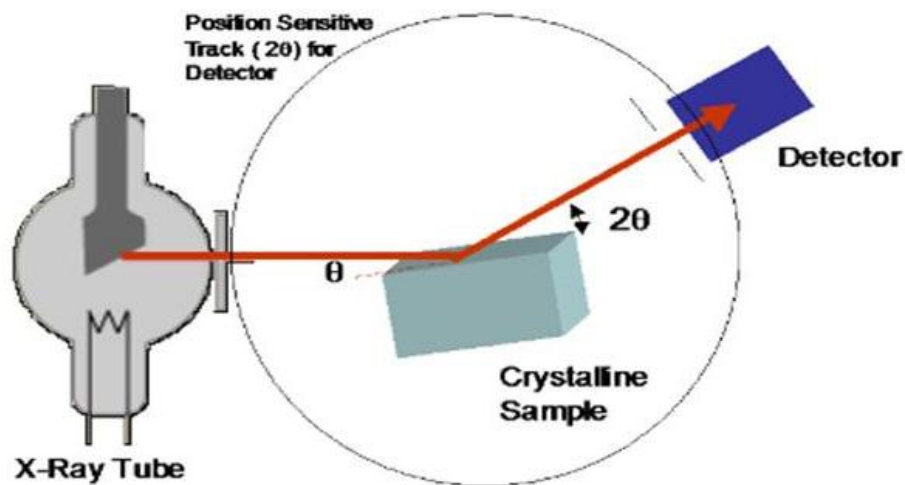


Figure 3.13: The schematic diagram of the XRD

3.6.3 Photoluminescence spectroscopy (PL)

Photoluminescence is a commonly used technique to study the optical properties of materials. It can be used to investigate the composition of a material quantitatively or semi quantitatively, even band gap, crystal quality and defect inside the materials.

In PL, light is shined in the sample; the sample will absorb photons, and upon de-excitation, light is emitted by the sample known as photo-excitation. This mechanism is generally known as photoluminescence. In order to probe the band gap of a material, light of shorter wavelength (greater energy) is desired to excite the material. Photo-excitation causes electron from valance band to move into excited states. The energy will be released when the electrons return to its equilibrium states. This may include the emission of light (a radiative process) or may not (a nonradiative process) as shown in Figure 3.14. The emitted light is detected as photoluminescence. The energy of emitted light (PL) relates to the difference in energy level. The presence of defects in the materials can also be estimated by the PL emission involving defect level transitions, so the quality of materials can be determined. The experimental set up and detailed description can be found elsewhere. The

model used in this study is Jobin Yvon HR 800 UV with energy excitation at 325 nm wavelength.

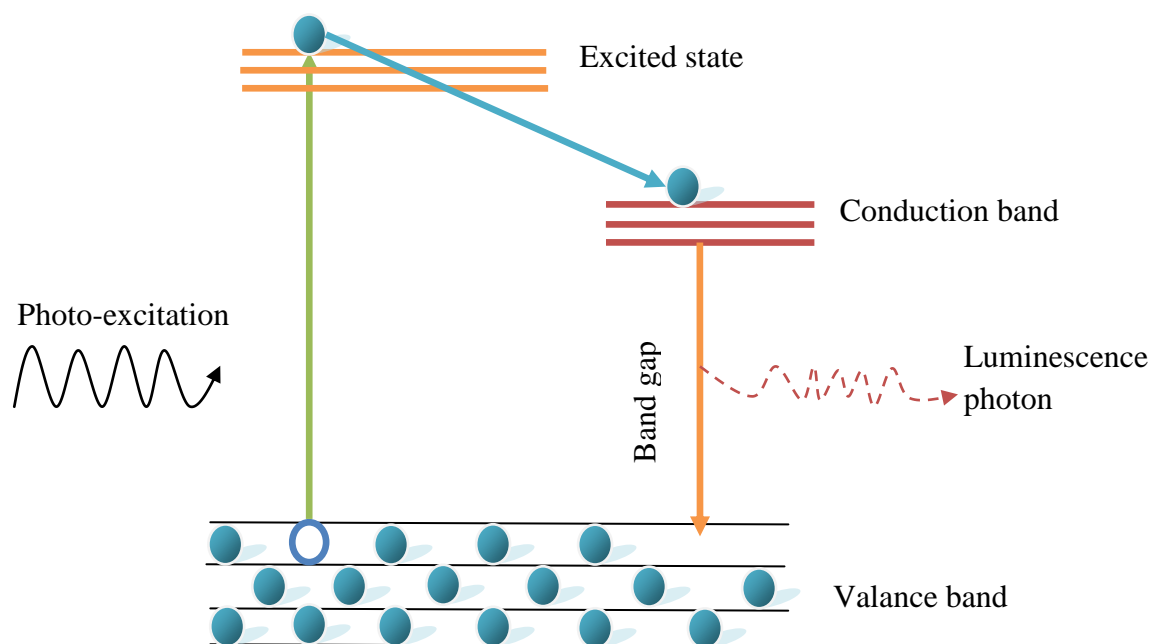


Figure 3.14: Schematic diagram of photoluminescence of atom from valance to conduction band.

3.7 Field Electron Emission Properties Measurements

Field emission property is one of the futures for metal oxide nanostructures. It is well known as Fowler-Nordheim (F-N) tunneling and in a form of quantum tunnelling in which electron pass from an emitting material to the anode through a barrier in the presence of a high electric field. It is very useful in many areas such as displays and other electronic devices [113]. This property has been carried out in many studies of ZnO such as enhanced field emission of well aligned ZnO nanowires [114]; field emission from ZnO nanowires directly from brass [115] and ZnO nanowires based field emitters [49]. Zinc oxide, with the advantage of low manufacturing cost on a large scale and also allowing relatively high

oxygen partial pressure during its operation, has become a good candidate for use in field emission cathode. Normally, field emission tests are carried out in vacuum at room temperature. The ZnO nanotip arrays are placed as the cold cathode, and a counter anode with known size is placed at a defined distance away from the cathode. An electric field is built up between the two electrodes when voltage is applied [116].

In the basic methodology of field emission, most of the nanostructured materials are deposited/coated on flat substrate (nominally 1 cm^2) forming broad area electron emitter. The substrate is an electrical conductor/semiconductor. The method of deposition depends on the properties of the material to be deposited. Amongst the various substrates, Si is most common as it is suitable for integrating with electronic device technology. This forms the cathode. The anode is indium tin oxide (ITO) coated conducting glass plate with or without phosphor coating. The anode-cathode separation is in the range \sim usually a few microns to a few mm. The anode and the cathode are held separated with the quartz or alumina spacer. This is called the diode configuration. A typical anode cathode system is shown in Figure 3.15. A holder carrying the anode and the cathode is then mounted in an ultra-high vacuum chamber which is subsequently evacuated to a pressure $\sim 10^{-7}$ - 10^{-8} mbar. The high voltage (0-10 kV) from stable DC supply is applied across the anode and the cathode. The current is measured by an electrometer amplifier (10^{-9} - 10^{-3} A). The current voltage characteristics are measured over a wide range of voltages. Current stability studies are performed by recording the field emission current (at the pre-set value) at regular time intervals. The field emission pattern is observed on the anode screen and recorded if necessary.

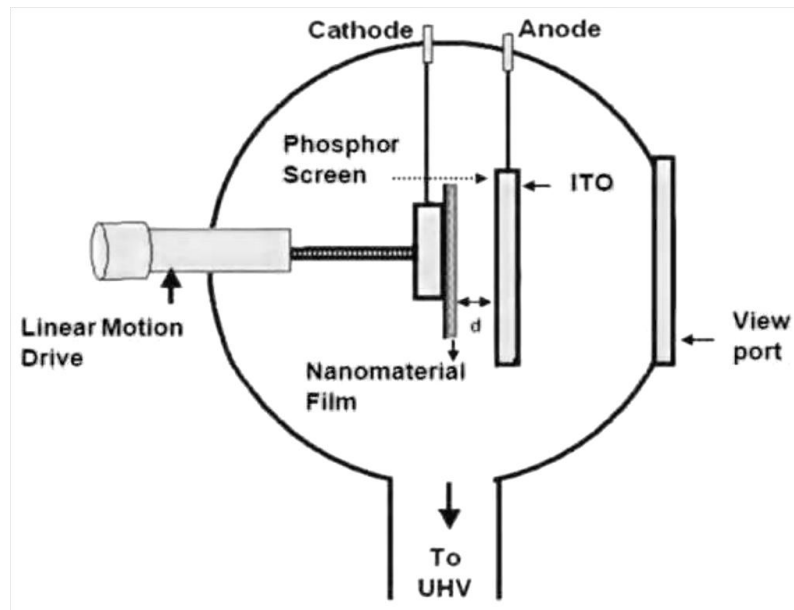


Figure 3.15: Schematic of the planar diode configuration arrangement in a vacuum chamber.

The field emission characteristics of metals can be analysed using F-N theory. The theory is expressed by the following equation:

$$J = A \left(\frac{\beta^2 E^2}{\varphi} \right) \exp\left(\frac{-B\varphi^{3/2}}{\beta E}\right) \quad (3.1)$$

Where J denotes the emission current density; β represents the effective field enhancement factor; E refers to the applied field between the cathode and the anode; φ refers to the work function; A refers to constant value $1.56 \times 10^{-10} \text{ AV}^{-2} \text{ eV}$ and B for the constant $6.83 \times 10^3 \text{ V eV}^{-3/2} \mu\text{m}^{-1}$.

Commonly, there are two graphs plotted to identify the emission characteristics. From the graphs, the turn-on field will be identified. It is defined as the average field between the anode and cathode when the emission current density reaches $1 \mu\text{A}/\text{cm}^2$. Also, the threshold field is defined as the field required getting current density of $1 \text{ mA}/\text{cm}^2$. The low value of turn on fields and threshold fields meet the requirement of superior field emitter [70]. The β value will be obtained from the slope of $\ln(J/E^2)$ vs. $1/E$ curve. The β is known as the field

enhancement factor which quantifies the ability of the emitter to amplify the electric field (E) at the emitting site. This can be determined by the geometry of the tip-morphology effect and the average distance between the emitters. Besides the *J-E* behaviours, the stability of the field emission can be tested. The current-time (*I-t*) curves will be recorded under constant applied voltage for certain times.

3.8 Summary

In this chapter, methods for the synthesis of nanostructures SiO₂ and ZnO using carbothermal reduction and nanostructures ZnO using plant extract based sol gel methods have been described. The nanostructures were analyzed using field emission scanning electron microscopy (FESEM), energy dispersed X-ray spectroscopy (EDX), X-Ray diffraction (XRD), Field emission electron (FEE) and photoluminescence spectroscopy (PL).

4.0 Results and Discussions

4.1 Introduction

In this chapter, the results and discussions on the characterization of the oxide nanoparticles and the field electron emission measurements of ZnO will be presented. The characterization of SiO₂ and ZnO nanostructures synthesized using carbothermal reduction technique will be discussed first. For the SiO₂ nanowires, the effect of temperature and growth time will be examined using FESEM equipped with EDX. In comparison, results from Cu-doped SiO₂ nanowires samples also will be presented. In the synthesis of ZnO nanostructures, the effect of temperatures and Al doping on ZnO nanostructures will be presented. Lastly, results from a study on ZnO nanostructures synthesized by sol-gel method using *C.Aurantifolia* extract will be presented.

4.2 Characterizations of SiO₂ nanostructures synthesized using carbothermal reduction technique.

In this sub-section, the effect of temperature and growth time on the morphology and structural properties of SiO₂ nanowires will be presented. Comparison of pure and Cu doped SiO₂ nanowires will be made.

4.2.1 Morphology and structural properties of SiO₂ Nanowires

SiO₂ nanostructures were synthesized by carbothermal reduction method using a thin layer of gold as catalyst. The effect of temperature on the source-substrate was examined using FESEM micrographs. The growth time was maintained at 2 hours without any carrier gas. The composition of precursor materials was 0.5 g SiO₂ and 0.5 g graphite powder. Figure

4.1 shows the FESEM micrographs of SiO₂ nanowires fabricated on gold coated silicon substrate at different temperatures which are (a) 900⁰C, (b) 1000⁰C and (c) 1100⁰C. It can be seen that the temperature plays an important role on the growth of SiO₂ nanowires. When the growth temperature is at 900⁰C, there is no nanowire formed on the substrate, but when it goes above 1000⁰C, it can be seen the nanowires have grown on the surface. For the SiO₂ nanowires grown at 1000⁰C, the nanowires appear to be inhomogeneous and orientation is not uniform. Then, nanowires with high-distribution density were observed on the surface when the temperature reaches 1100⁰C as shown in Figure 4.1 (c). The same SiO nanowires have been reported in the earlier report [117], but the technique generally requires Ar gas during the entire process. Thus, the flow rates of the flowing gas need to consider carefully. In that work, it was reported that there was no growth occurred at 900⁰C and the most favourable temperature for nanowire growth is at 1100⁰C.

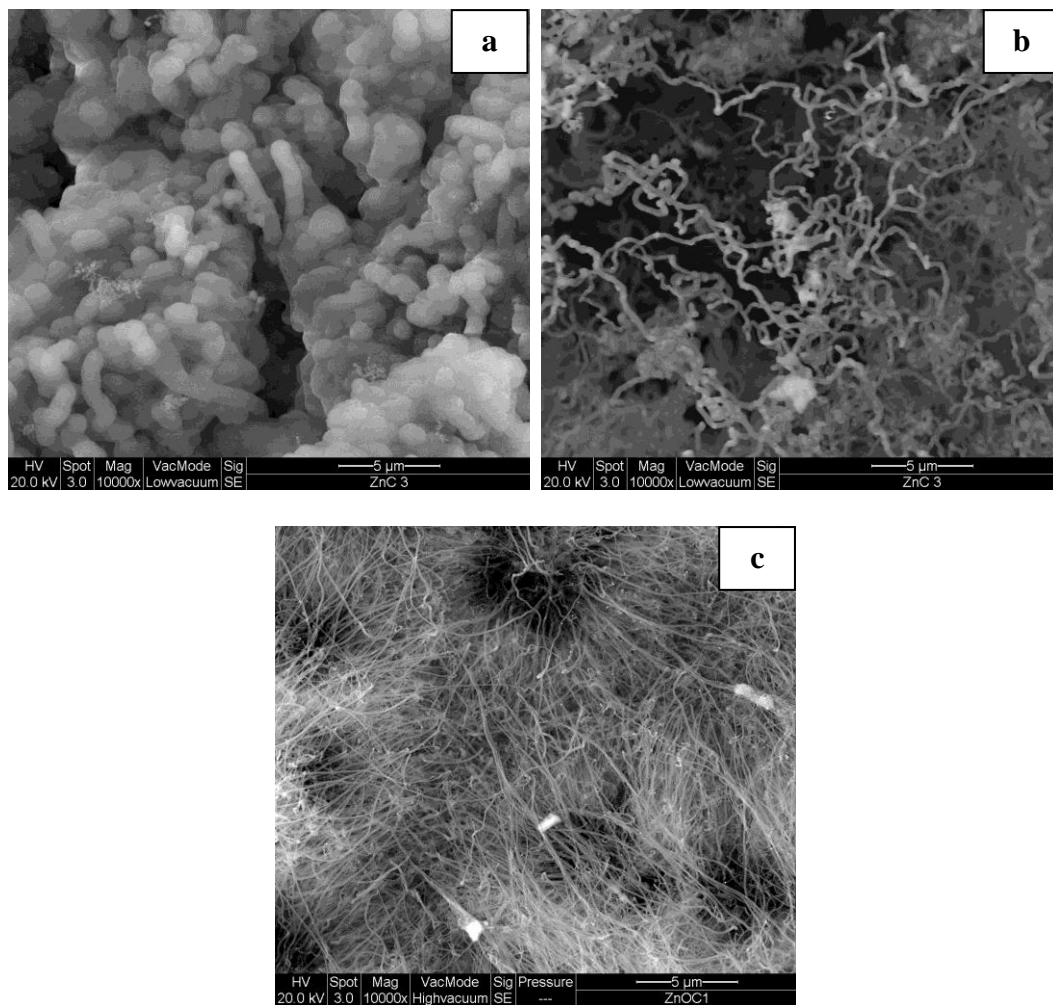


Figure 4.1: FESEM micrographs of SiO_2 nanowires fabricated on gold coated silicon substrate at three different temperatures (a) 900°C , (b) 1000°C and (c) 1100°C . The growth time is at 2 hours.

Figure 4.2 shows the FESEM images on the effect of synthesis time on the fabrication of SiO₂ nanowires using carbothermal reduction route. At first, the nanowires were synthesized at 1 hour. It can be seen that the as-synthesized product consisted of nanowires with relatively low density, curved and random distribution as shown in Figure 4.2 (a). Meanwhile, if the synthesis time was set to be at 2 hours, the as-synthesized products were formed in high density and most nanowires are entangled with one another that make it hard to estimate the length. The diameter of the nanowires ranged from 50 to 150 nm. The EDX analysis in Figure 4.3 reveals that the nanowires contain silicon and oxygen. No other impurities observed. The inset in the Figure 4.3 shows the distribution of weight% of the elements. Silicon percentage is 54.80% and the balance of 45.20% is attributed to oxygen. Conversion to atomic percentage gave 40.9% silicon and 59.1% oxygen. The disparity in the 1:2 ratio of silicon to oxygen to confirm to the stoichiometry of SiO₂ was due to the contribution of the silicon substrate in the EDX measurement. Strangely contribution from gold catalyst was not observed.

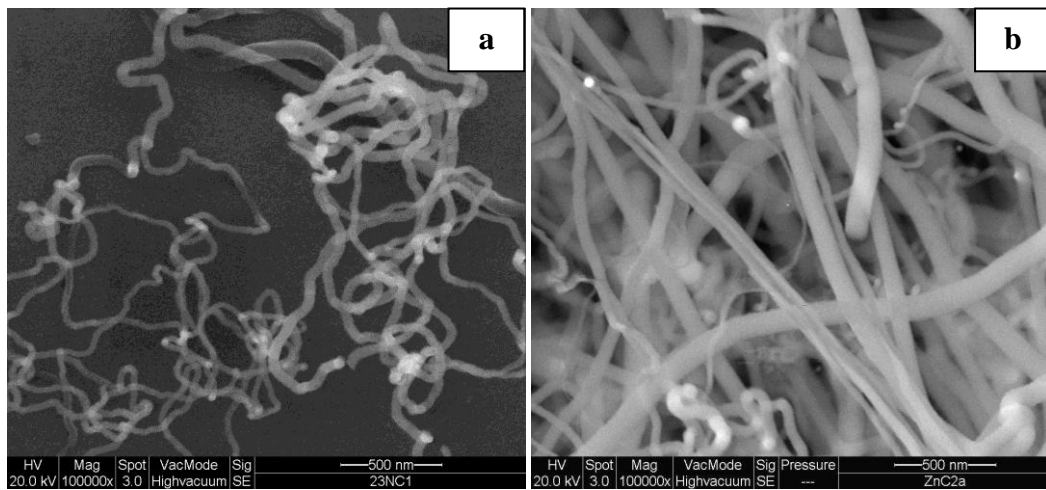


Figure 4.2: The SEM images of SiO₂ NWs fabricated on gold coated silicon substrate at (a) 1 hour and (b) 2 hours at constant temperature of 1100⁰ C.

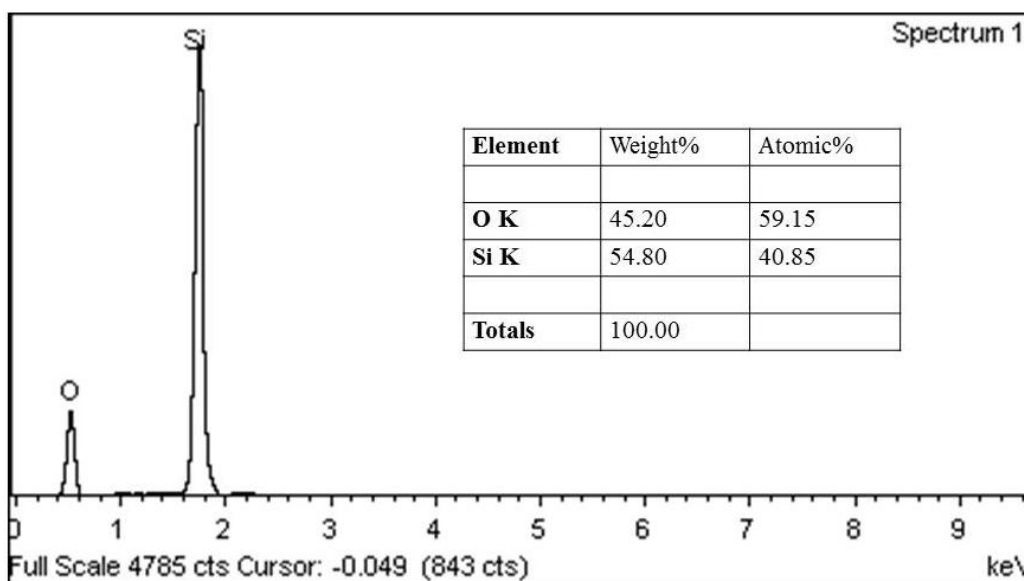


Figure 4.3: The EDX spectrum on the SiO₂ NWs

4.2.2 Morphology and structural properties of Cu doped SiO₂ Nanowires

Figure 4.4 shows the FESEM equipped with EDX of SiO₂ nanowires doped with Cu. The inset in EDX spectrum shows the weight% of the elements present in the experiment. It can be seen from the elemental composition that Si dominates the highest value which is 75.92%, followed by oxygen and carbon which at 9.56% and 9.40% respectively. The lowest weight% is Cu element which is at 0.72% only. Thus, it confirmed that the SiO₂ nanowires consist of Si, O, C and Cu elements. In terms of atomic % the values are 65.66% for Si, 19.00% for C, 14.52% for O, 0.54% for Au and 0.27% for Cu. The percentage for Si at 65.66% included the substrate, and based on the percentage of O, the percentage of Si in the form of SiO₂ was 14.6%. As such, the percentage of Cu incorporation into the SiO₂ nanowires was 1.84%, based on 0.27/14.56 ratio. The existence of Au at 0.54 atomic% was from the coating as catalyst at the beginning of the process. The existence of gold is maybe because of this method is not efficient enough to clean all traces of gold especially in

doping process; the nanowires remain strained and contaminated by catalyst residues. Attempt to remove the catalyst residues were also performed, but are not totally efficient [118]. From the FESEM image, it can be seen that SiO₂ NWs were randomly dispersed on the surface of silicon wafer. Nanowires were entangled with each other, inducing the tips of nanowires oriented towards randomly.

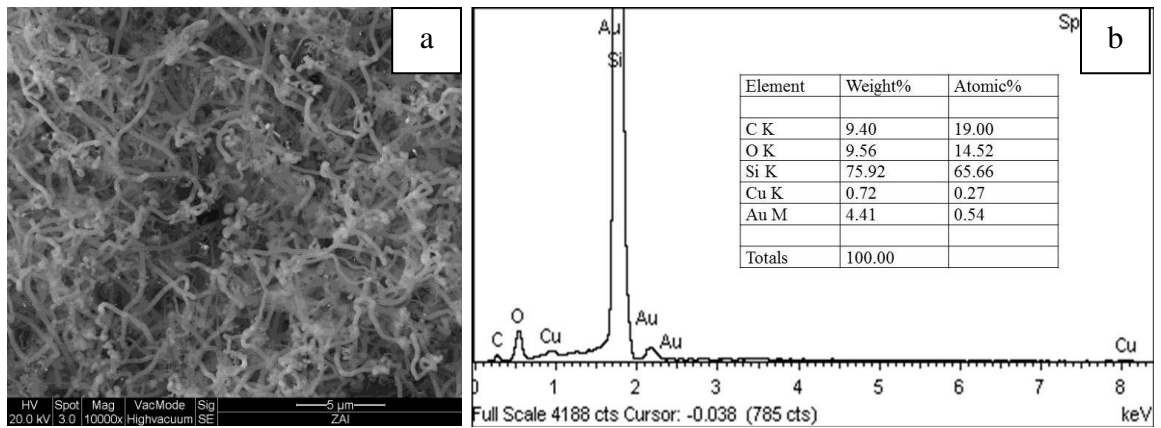


Figure 4.4: (a) SEM image of Cu doped SiO₂NWs and (b) EDX analysis.

4.3 Characterizations of ZnO nanostructures synthesized using carbothermal reduction technique.

4.3.1 Morphology and structural properties of ZnO

Figure 4.5 shows the FESEM images of the ZnO structures fabricated on the gold coated Si substrate at different deposition temperature and 2 hours syntheses time using carbothermal reduction method. It can be seen that three kinds of growth morphologies were evident from the different synthesis temperatures. Figure 4.5 (a) reveals the as-synthesized structures of a uniform crystal film covering the entire substrate surface. At 1000°C as shown in figure 4.5 (b), dense microstructures formed on the substrate. It can be seen the non-aligned nanorods grown at certain places with varying diameter. At 1100°C as shown in Figure 4.5 (c), the FESEM image indicates that the specimens exhibited similar nanorods with ellipsoidal morphology with sharp tips. The difference in the morphology may have resulted from the dynamics of the growth species during the synthesis process. Here, the role of temperature is expected to be crucial during the carbothermal process where ZnO was reduced to Zn and transported to the substrate and absorbed into the gold catalyst used until the point of saturation. Slight fluctuation in the temperature of the gold catalyst and Zn solution results in the condensation of Zn and oxidized to form ZnO. Thus the morphology of the ZnO formed are expected to depend on the amount of Zn vapour transported to the substrate and also the structure of the Au catalyst, both are influenced by the synthesis temperature. The role of Au in the formation of metal oxide nanostructures have been discussed before in literature [119]. As the Au thin film was being raised to the growth temperature, it melted to form isolated surface Au nanoclusters. Not that due to their small size, nanoclusters from Au thin films is excellent catalysts for the growth of nanometer-

scale ZnO wires. Thus, in this case, it can be assumed that the Au catalysts helped the ZnO nanostructures grow from thin films to ellipsoidal shapes when the temperature increased. X-ray diffractometer (XRD) was used to characterize the crystal structure of the as-grown sample. Figure 4.6 shows the XRD patterns of the deposited products on the gold-coated silicon substrate. The typical XRD spectrums were presented without any noticeably changed from varying the growth temperature namely ZnO crystal faces (100), (002), (101), (102), (110), (103) and (112) peaks are observed. Furthermore, the XRD pattern of all samples showed a sharp ZnO(101) diffraction peak. The peaks associated with ZnO are listed in Table 4.1. From the XRD results the samples were all ZnO with the wurzite crystal structure.

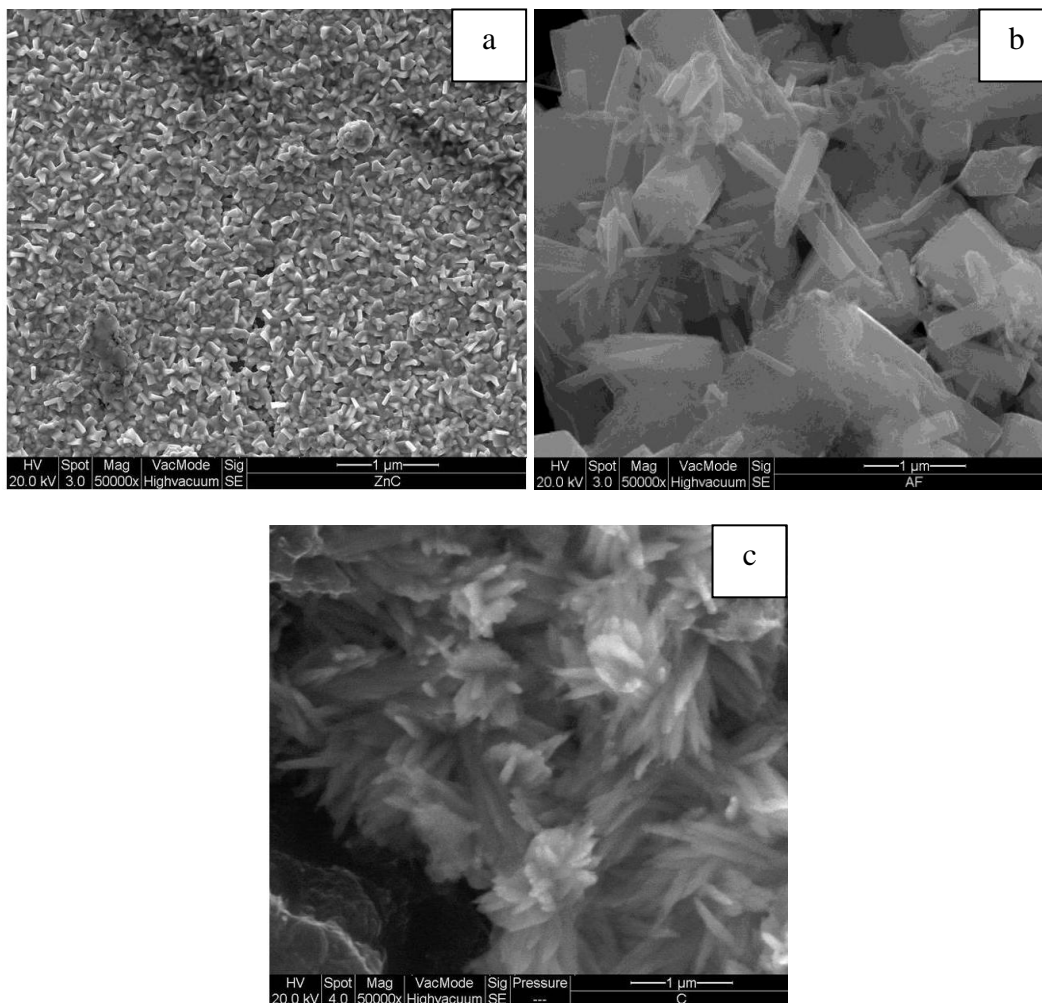


Figure 4.5: SEM micrographs of ZnO structures fabricated on gold coated silicon substrate at (a) 900°C, (b) 1000°C and (c) 1100°C for 2 hrs synthesis time.

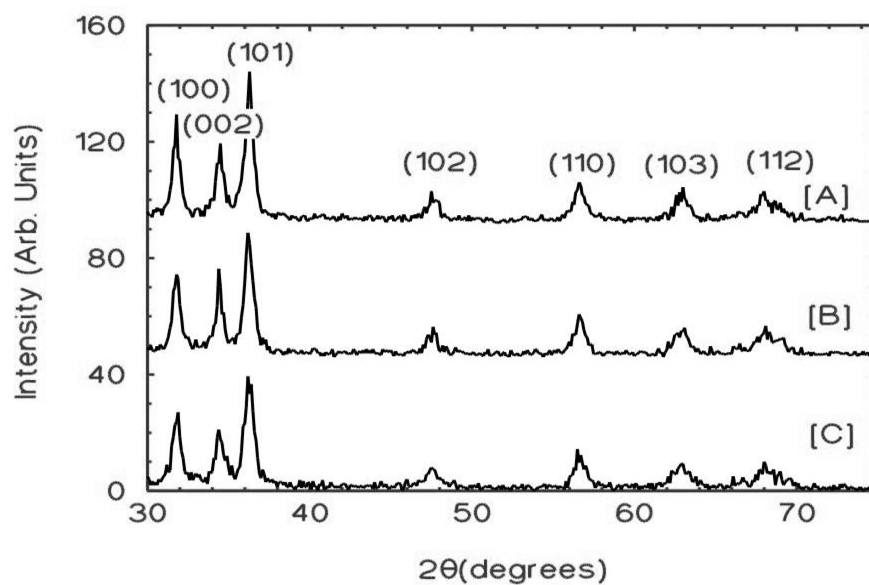


Figure 4.6: XRD spectrum of the as grown samples (a) 900°C, (b) 1000°C and (c) 1100°C.

Table 4.1: List of X-ray diffraction peaks of ZnO nanostructures synthesized at 900°C, 1000°C and 1100°C for 2 hours.

Temperature (°C)	2θ (Degree)	Assigned peak
900	31.68 ⁰	(100)
	34.35 ⁰	(002)
	36.16 ⁰	(101)
	47.10 ⁰	(102)
	55.30 ⁰	(110)
	62.80 ⁰	(103)
	68.00 ⁰	(112)
1000	31.68 ⁰	(100)
	34.35 ⁰	(002)
	36.16 ⁰	(101)
	47.10 ⁰	(102)
	55.30 ⁰	(110)
	62.80 ⁰	(103)
	68.00 ⁰	(112)
1100	31.68 ⁰	(100)
	34.35 ⁰	(002)
	36.16 ⁰	(101)
	47.10 ⁰	(102)
	55.30 ⁰	(110)
	62.80 ⁰	(103)
	68.00 ⁰	(112)

4.3.2 Field electron emission of ZnO Nanostructures

Figure 4.7 to Figure 4.9 show field electron emission properties of the ZnO samples fabricated at different synthesis temperatures in the form of J - E curves. Inset in each graph is the F - N curves of the ZnO nanostructures. The field emission characteristics of the ZnO nanostructures (field emitters) were measured and analyzed using Fowler-Nordheim (FN) equation, describing the electrons passing across an energy barrier under the effect of an electric field at the emitter tip.

$$J = A \left(\frac{\beta^2 E^2}{\phi} \right) \exp \left(\frac{-B\phi^{3/2}}{\beta E} \right) \quad (4.1)$$

Where J denotes the emission current density, β represents the effective field enhancement factor, E refers to the applied field between the cathode and anode; ϕ refer to the work function (5.3 eV for ZnO), A and B are constants ($A= 1.56 \times 10^{-10} \text{ AV}^{-2} \text{ eV}$, $B= 6.83 \times 10^3 \text{ V eV}^{-3/2} \mu\text{m}^{-1}$). The field emission measurement was carried out in a vacuum chamber at pressure of 10^{-5} mBar. The current density is defined as $J=I/A$ where I is the measured emission current and A is the area of emitter. The applied field is defined as $E=V/d$ where V is the applied potential and d is the separation between anode and cathode which was maintained at $150 \mu\text{m}$ throughout the measurement. From the current density versus electric field graph, a parameter known as the turn on field is defined as the electric field to produce a current density of $10 \mu\text{Acm}^{-2}$. Table 4.2 lists all the comparison values of current density, J and turn on field at three different temperatures. Comparing the three values from J - E curves, the turn on field was observed to be increasing as temperature increases. From the FESEM images above, the tips of ZnO nanostructures become sharper as the temperature increases. Hence, the results here lead to the idea that field emission properties have a close relationship with the surface morphology of the samples. Although the turn on fields varies

slightly with morphologies they are rather high from the literature reported before [120]. Xu *et.al* [122] reported field emission from ZnO nanopins with also low turn on field at 19.02 V/ μm . It can be stated that within the last several years, tremendous progress has been reported in field emission applications of ZnO nanostructures. Table 4.4 represents the results on field emission properties of ZnO nanostructures reported, along with the corresponding synthetic methods and field emission performances. All values of turn on fields are much lower compared with our experiment. The field emission from different ZnO nanostructures follows the F-N relationship. The slope fitted to a straight line in the F-N curve corresponds to $B\phi^{3/2}/\beta$, where β is the field enhancement factor. By plotting $\ln(J/E^2)$ versus $1/E$ as shown in the inset, the curve shows more than one slope. Table 4.3 lists all the field enhancement factors for all samples. For sample 900 °C, the calculated enhancement factor, β values are $\beta_1= 279.34$ and $\beta_2= 148.39$. When the temperature increased to 1000°C, the values of $\beta_1= 328.98$ and $\beta_2= 232.20$. If the temperature was elevated to 1100°C, the values of $\beta_1= 398.11$ and $\beta_2= 220.32$. In average, the value of field enhancement factors in this experiment is much lower compared with the previous reports [120, 123, and 126]. It is believed that the lower β values in this experiment are because of the high turn on field discussed earlier. The variations of the values β are influenced by many factors, such as the emitter geometry, crystal structure quality, vertical alignment, and emitter density [116]. It is desirable to have high β values. If it is too low, then the emission current density will be low; if it is too high, then the local electric field around the emitter tips will have an electrostatic screening effect induced by the neighbouring nanowires, which generally lower the β value. In comparison, although the nanostructures have not perfect orientation perpendicular to the substrate in the sample synthesized at 1100°C, but the clear tip is appeared as shown in Figure 4.5 (c). As the most of

nanostructures are straight with good crystal quality, so the excellent field-emission property and the highest average β was gained. Measurements of the emission stability were carried out on the ZnO nanostructures for all samples. As shown in Figure 4.10, the result for 900⁰C shows that the field-emission current density of 2.4 mA/cm² was recorded for 20 minutes at the same applied voltage of 1470 V. There is slightly fluctuation of current at approximately $\pm 1\%$ and the average current did not decrease over this period of 20 minutes. While Figure 4.11 show the stability for field emission at 1000⁰C. The I-t curves was recorded at the initial current density of 7.0×10^{-4} A/cm² which was approximately at 950 V constant applied voltage for 20 minutes. The field emission current has slightly increased and fluctuate at about $\pm 1\%$. Finally, the stable field emission current was tested at sample 1100⁰C as shown in Figure 4.12 for 20 minutes also. The initial current density was set to be 2.0 mA/cm² at about 1000 V. The behaviour looks almost similar with the previous sample with a current fluctuation of about 1%. The average current did not decrease over period of 20 minutes. This indicates that ZnO nanostructures are very stable field electron emitters. The fluctuations in the FE currents are attributed to the adsorption and desorption of the residual gas molecules on the ZnO nanostructures emitter surface [121].

Table 4.2: Comparison of electric field (E) versus current density (J) for different temperature

Temperature ($^{\circ}\text{C}$)	Turn on field ($\text{V}/\mu\text{m}$)	Current density, J (μAcm^{-2})
900	~40	10
1000	~41	10
1100	~44	10

Table 4.3: Field enhancement factors, β of ZnO nanostructures at different temperatures.

Temperature ($^{\circ}\text{C}$)	Field enhancement factor, β	
900	$\beta_1 = 279.34$	$\beta_2 = 148.39$
1000	$\beta_1 = 328.98$	$\beta_2 = 232.20$
1100	$\beta_1 = 398.11$	$\beta_2 = 220.32$

Table 4.4: Turn on field and field enhancement factor values from literature.

Synthesis Method	Turn on field / $\text{V}\mu\text{m}^{-1}$	Field Enhancement Factor/ β	Ref.
Electrochemical deposition	15.5 and 9.5	1188 and 1334	123
Vapor phase growth	6.0 at $0.1 \mu\text{Acm}^{-2}$	847	124
Solution-based method	4.2	2350	125
Carbothermal vapor transport	0.7 at 1mAcm^{-2}	4.11×10^4	126
Metal organic chemical vapour deposition	0.85 at $0.1 \mu\text{Acm}^{-2}$	8328	127

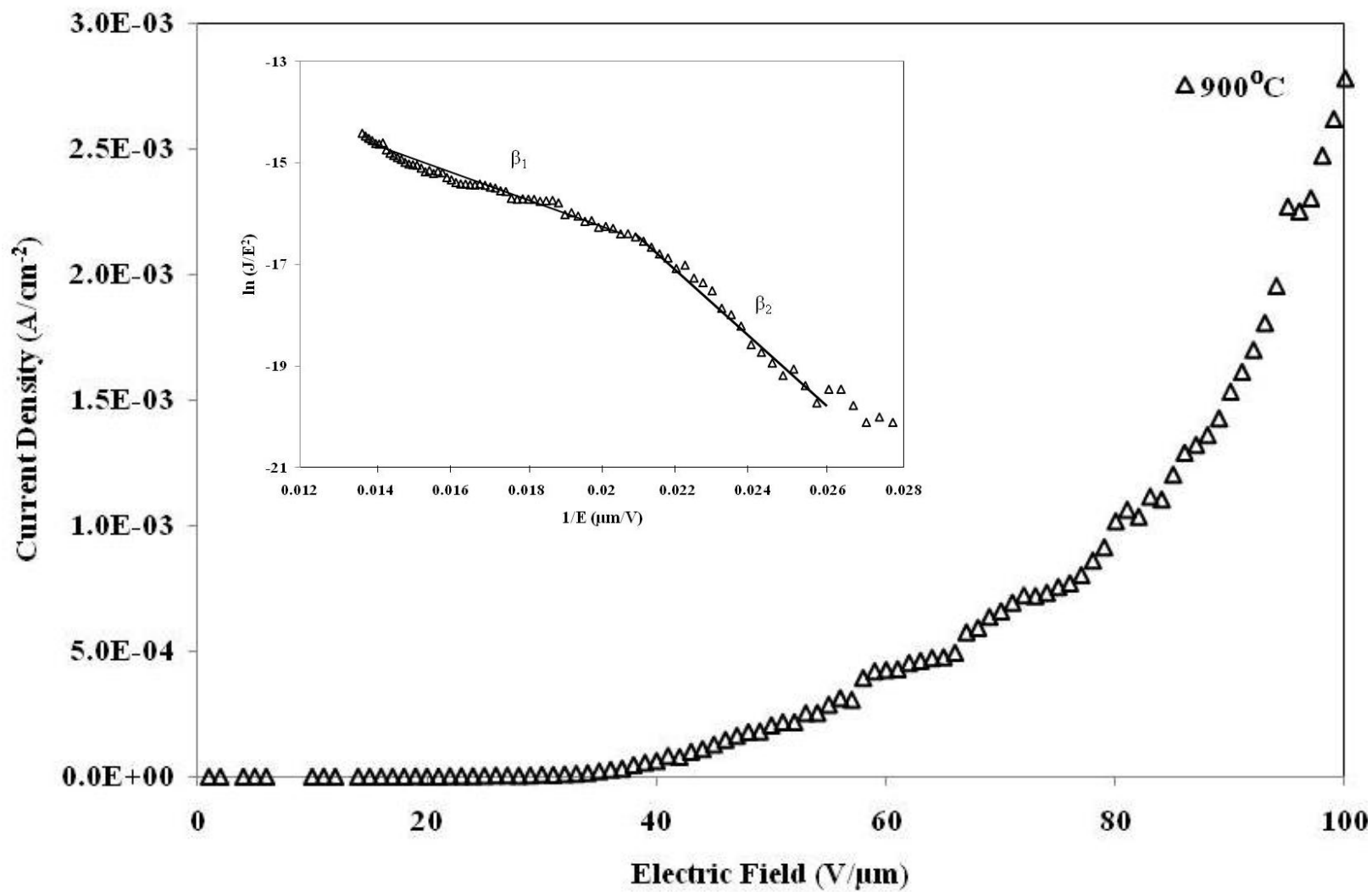


Figure 4.7: The field emission current density J on the applied electric field E of the samples at $900^\circ C$. Inset is the F-N relationship of $\ln(J/E^2) - 1/E$ plot.

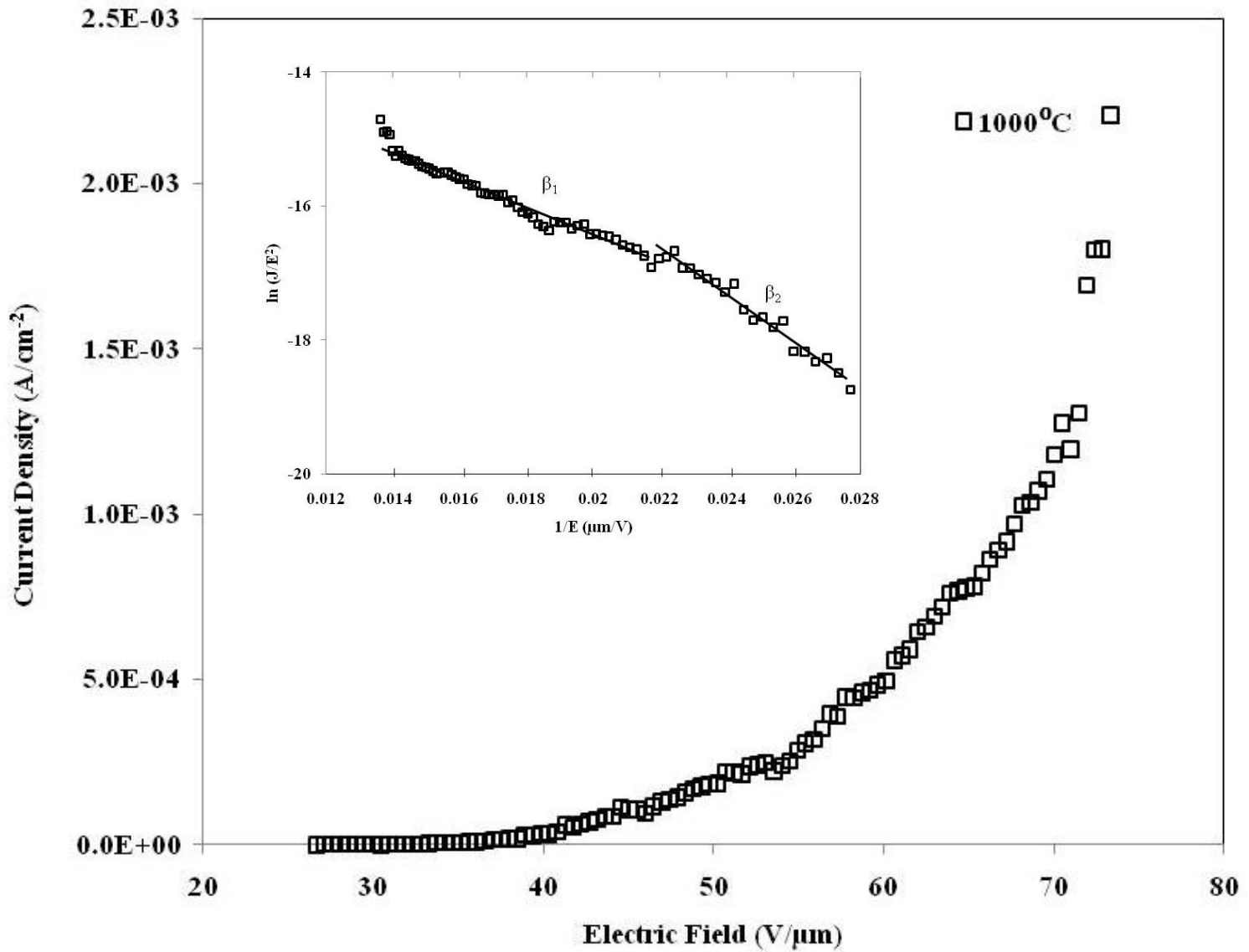


Figure 4.8: The field emission current density J on the applied electric field E of the samples at 1000°C . Inset is the F-N relationship of $\ln(J/E^2) - 1/E$ plot.

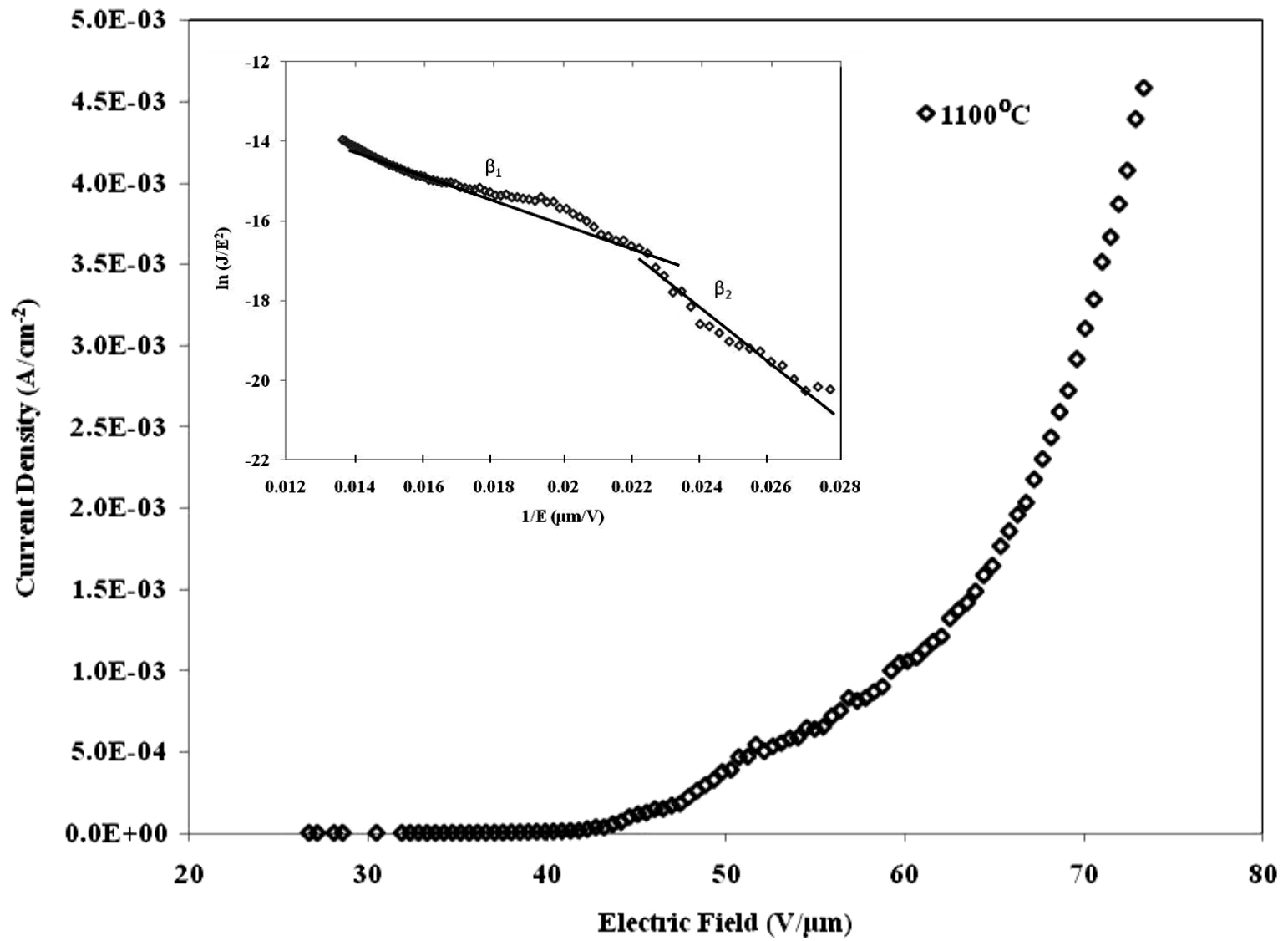


Figure 4.9: The field emission current density J on the applied electric field E of the samples at 1100°C . Inset is the F-N relationship of $\ln(J/E^2) - 1/E$ plot.

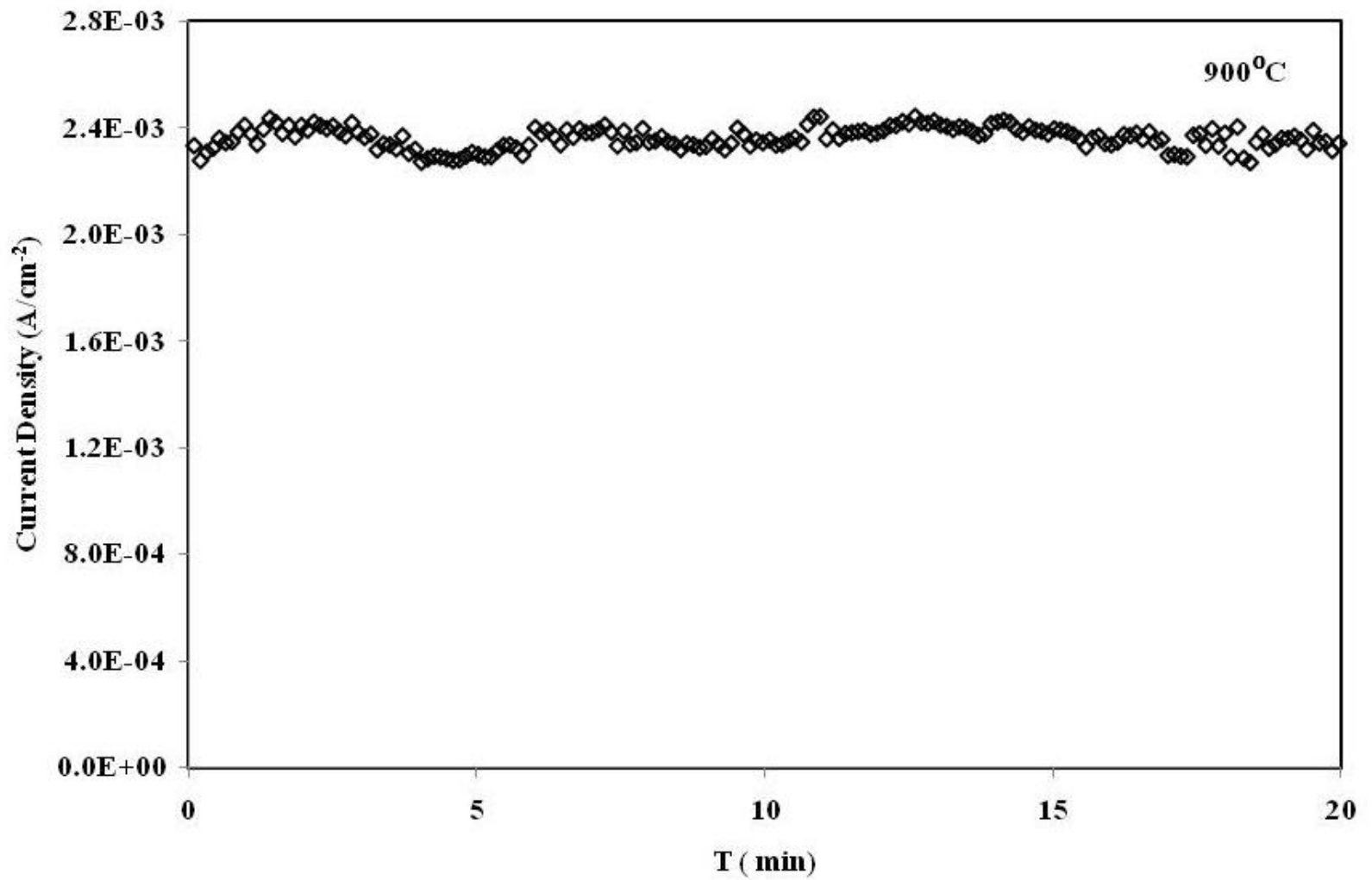


Figure 4.10: Time dependence of the emission current of ZnO nanostructures at constant applied voltage and temperature 900°C.

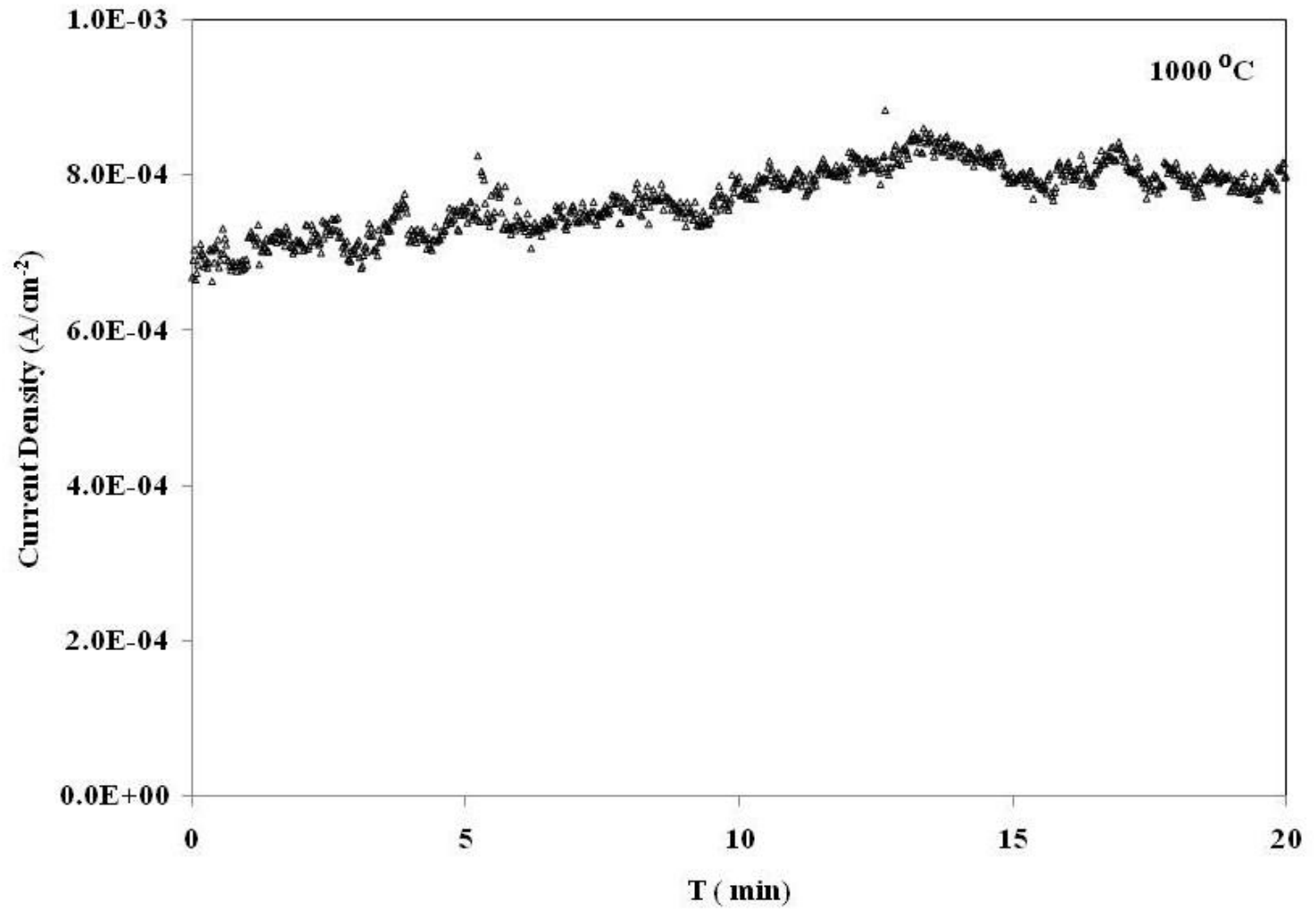


Figure 4.11: Time dependence of the emission current of ZnO nanostructures at constant applied voltage and temperature 1000°C.

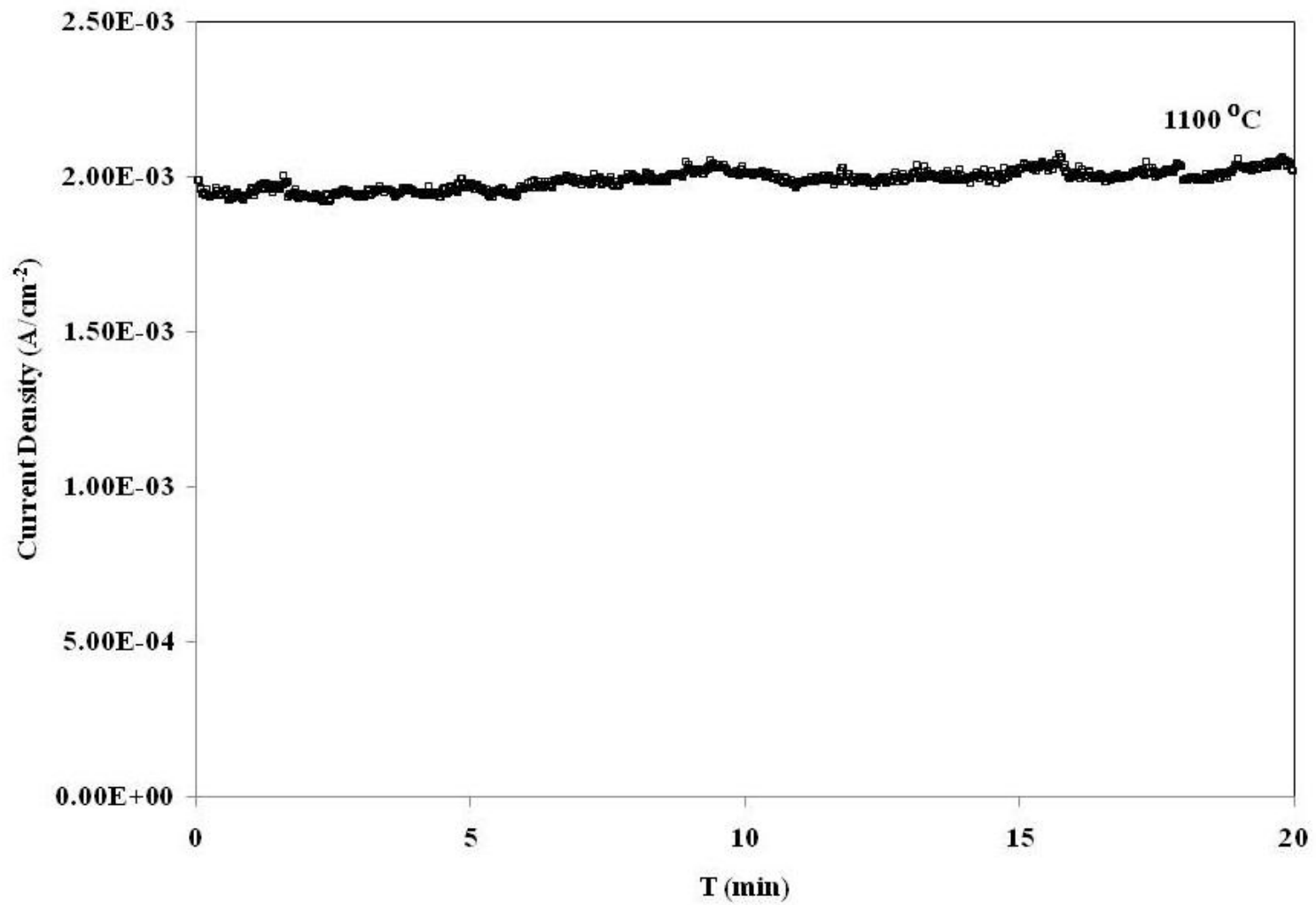


Figure 4.12: Time dependence of the emission current of ZnO nanostructures at constant applied voltage and temperature 1100⁰ C.

4.3.3 Morphology and structural properties of Al-doped ZnO Nanostructures.

ZnO nanostructures were also doped with Al and synthesized at 1100⁰C for 2 hours using carbothermal reduction route. Figure 4.13 shows the representative FESEM image of the fabricated rod-like ZnO nanostructures with the EDX analysis as in Figure 4.14. The absence of Al results in the different in morphology of ZnO nanostructures. Inset of Figure 4.14 reveals the weight% of the elements existed in the formation of rod-like ZnO. In terms of atomic % the values are 45.34% for Zn, 5.71% for Si, 0.78% for Al, 28.79% for O and 19.37% for C. The percentage for ZnO is 74.13% and the percentage of Al incorporated in ZnO is 1.05%. Figure 4.15 shows XRD patterns of the Al-doped ZnO nanostructures. Diffraction peaks of the Al element were not observed in the XRD pattern. The dominant growth plane was the Zn (101) plane located at $2\theta = 36.1^{\circ}$. One way to investigate the efficiency of Al doped ZnO nanorods are by studying the optical properties of the as grown sample. This can be compared with the undoped ZnO nanostructures studied earlier. Table 4.5 list all the XRD peaks of rod-like Al-doped ZnO synthesized at 1100⁰C for 2 hours.

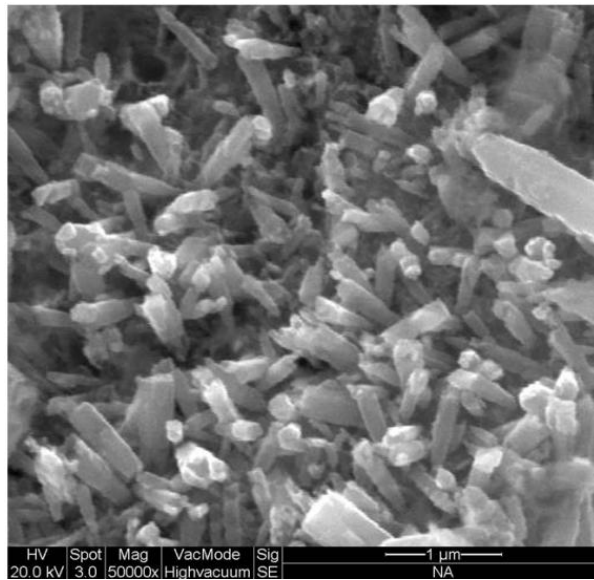


Figure 4.13: FESEM micrograph of Al doped ZnO nanorods synthesized at 1100 ° C for 2 hours.

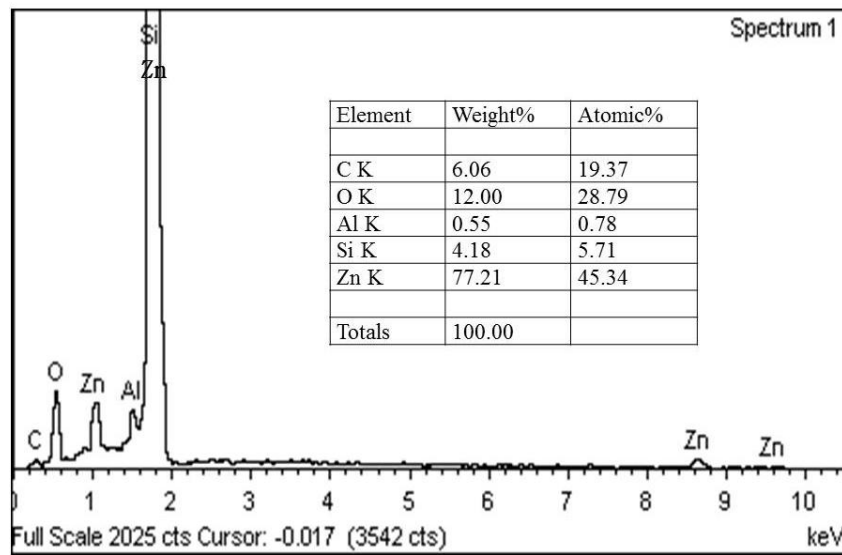


Figure 4.14: EDX analysis of Al doped ZnO nanorods synthesized at 1100 ° C for 2 hours.

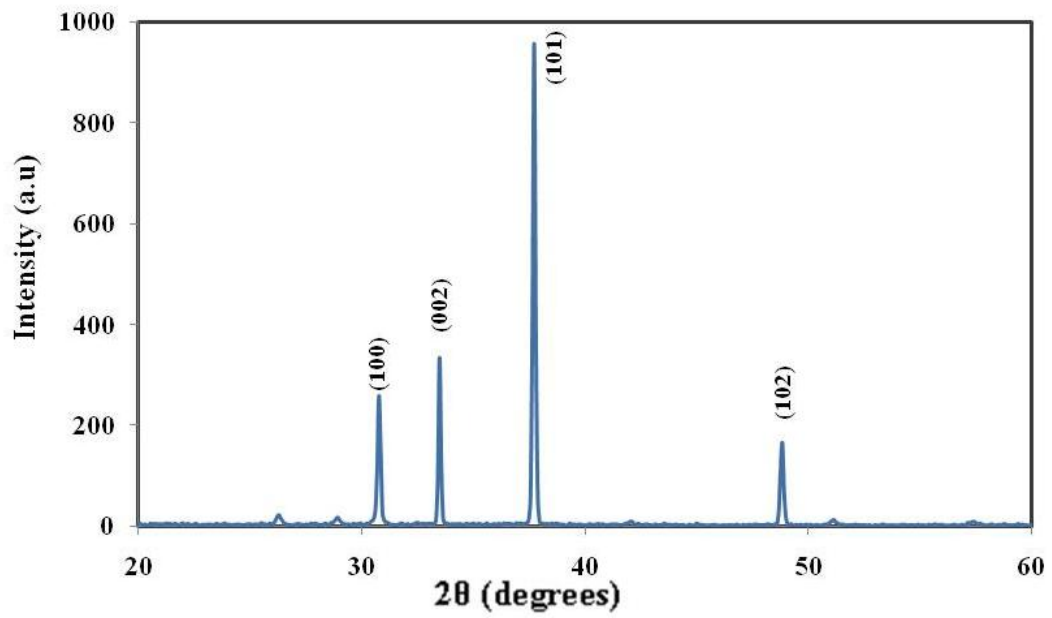


Figure 4.15: XRD pattern of Al doped ZnO microstructures.

Table 4.5: List of X-ray diffraction peaks of rod-like ZnO synthesized at 1100^o C for 2 hours.

Temperature (^o C)	2θ (Degree)	Assigned peak
1100	~31 ^o	(100)
	~34 ^o	(002)
	~36 ^o	(101)
	~47 ^o	(102)

4.3.4 Field electron emission of Al-doped ZnO Nanostructures

Figure 4.16 shows the field-emission current density (J) of the Al-doped ZnO nanorods as the function of the applied field (E). In this study, field emission tests were carried out in a vacuum chamber at pressure of 10^{-5} mBar at 300K. The ZnO nanotips were placed as the cold cathode, and a counter anode with distance of 150 μm . From current density versus electric field graph, it shows that the turn on field which is defined as the electric field required producing an emission current density of $10 \mu\text{Acm}^{-2}$ was $\sim 37 \text{ V}/\mu\text{m}$. The value is slightly lower than the undoped ZnO nanorods synthesized at the same temperature before. This is because, vertical tips of the undoped ZnO nanorods greatly evaluate the electric field around it and therefore the electrons are easier to be extracted out [120]. When electric field was raised to $100 \text{ V}/\mu\text{m}$, the maximum current density was found to be at $2.97\text{mA}/\text{cm}^2$. The field-emission property was also analyzed by applying the Fowler-Nordheim (FN) theory as discussed earlier.

The emission behaviour can be examined from the linearity of curves plotting $\ln(J/E^2)$ versus $1/E$ as shown in the inset of Figure 4.16. It is found that the straight line is in agreement with the FN equation. That is the field emission from the present ZnO nanorods belong to a barrier tunnelling, quantum mechanical process [70]. The result indicates there are more than one slopes. For Al-doped ZnO nanorods, the two values of enhancement factors are $\beta_1 = 457.87$ and $\beta_2 = 269.96$. β is influenced by many factors, such as the emitter geometry, crystal structure quality, vertical alignment and emitter density. The two values of β in this study most probably because of the variation in tip local field by ZnO nanorods. Field emission from Al-doped ZnO nanostructures was also studied by Shalaka et.al [128].

The threshold field measured at $1 \mu\text{Acm}^{-2}$ was observed to be $2.0 \text{ V}/\mu\text{m}$ and $2.3 \text{ V}/\mu\text{m}$. The β from the nonlinear graphs were 9.3×10^3 and 3.9×10^3 . These values are far different from this study.

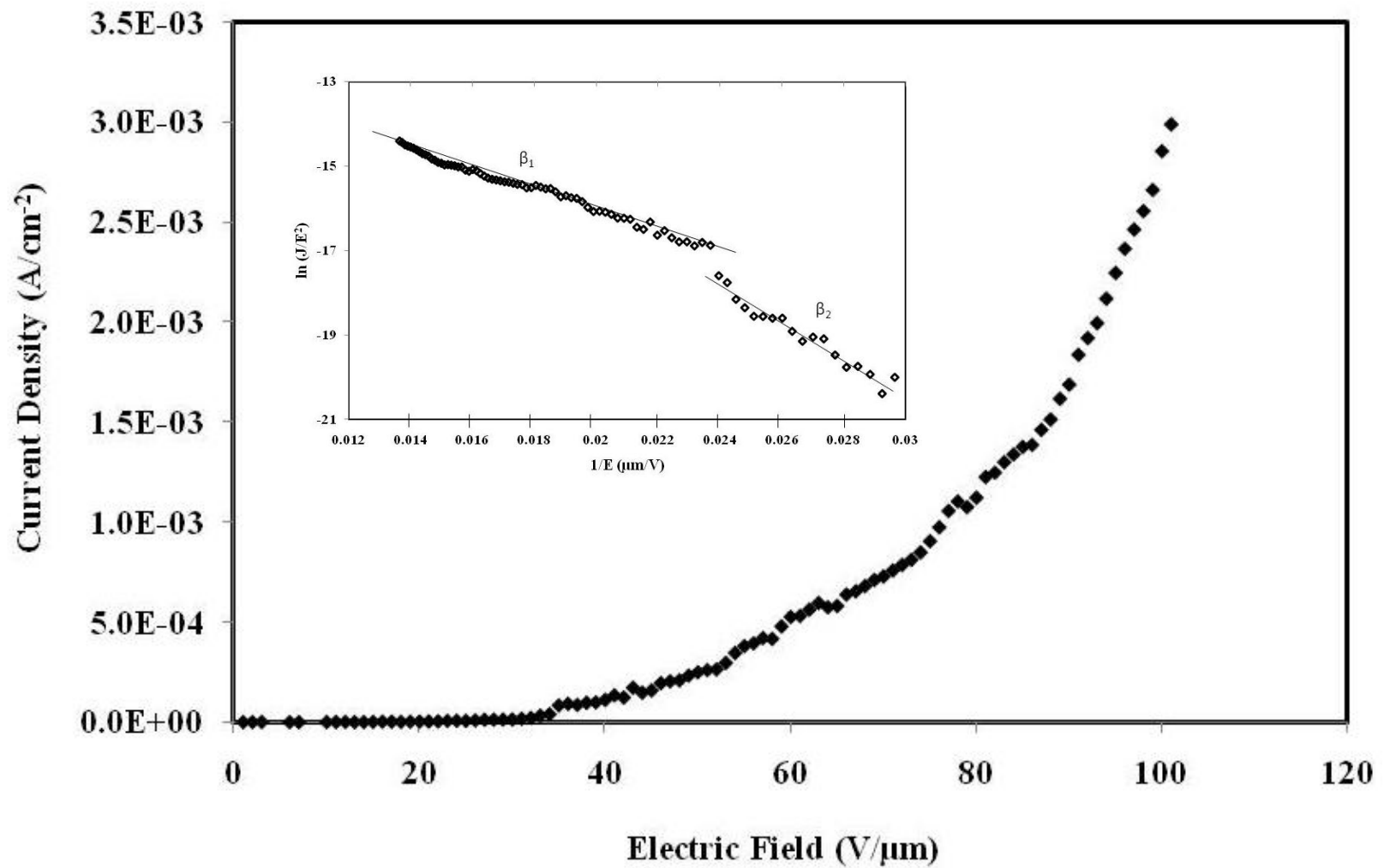


Figure 4.16: The field-emission current density (J) of the Al-doped ZnO nanorods as the function of the applied field (E). Inset is the corresponding F-N curve.

4.4 Characterizations of ZnO nanostructures synthesized using sol-gel technique.

The use of plant extract in the synthesis of nanostructured materials can be a cost effective and eco-friendly approach. This part will report the biosynthesis of zinc oxide nanoparticles using *C. Aurantifolia* extracts. *Spherical zinc oxide nanoparticles were produced using different concentration of zinc acetate which was used as the zinc source. While the nanoparticles changed into different length of nanorods in the variation of pH values. The morphology of the ZnO nanostructures using citrus extract was examined using FESEM, XRD and PL.*

4.4.1 Effect of concentrations on the fabricated ZnO nanostructures

Figure 4.17 shows the FESEM micrographs of ZnO particles synthesized at 90°C for 2 hours at 0.05 M, 0.10 M, 0.15 M and 0.20 M respectively. A non-uniform surface morphology was clearly observable from the lowest concentration as shown in *Figure 4.17(a)*, revealing no particles formed. When the concentration of Zn in citrus extract was increased to 0.10 M as shown in *Figure 4.17(b)*, it can be seen that the particles agglomerated at certain places and the diameters of the particles varies approximately between 0.15µm to 0.35µm. *Figure 4.17(c)* and *Figure 4.17(d)* showed that the particles are homogeneous with good nanostructures. ZnO nanoparticles are mostly in spherical shape. From the FESEM images for ZnO synthesized at 0.15 M and 0.20 M look uniform with structures of about 100 nm. These morphologies are quite similar with Dubey et.al [129], studied ZnO-NPs for the fabrication of enzyme biosensor using 0.45 M zinc nitrate and synthesized at 2 h. The XRD patterns of ZnO nanostructures are shown in *Figure 4.18*.

The XRD pattern at 0.10 M exhibited the XRD pattern similar to 0.15 and 0.20 M. It is found that the peak intensity tends to increase with the increase in zinc acetate concentration. For all samples, peaks from the (100) reflection plane dominated with peaks due to the (101), (102) and (110) appear to be subdued. It seemed that the ZnO NPs has preferential orientation at (100). While the peaks labelled with stars were assigned to be Zn(OH)₂. The Zn(OH)₂ peaks appear to be occurred in all concentrations, only the intensity varies.

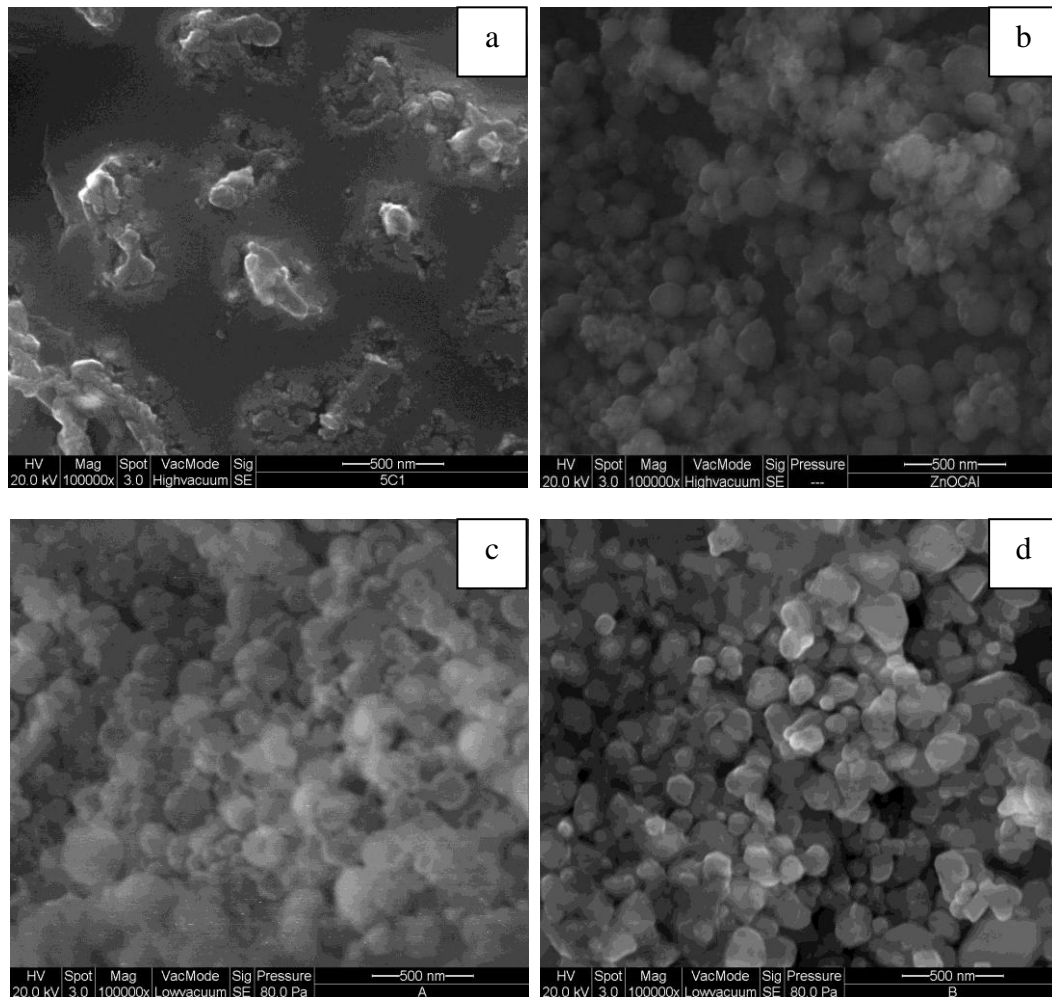


Figure 4.17: FESEM images of ZnO particles using Zinc acetate at concentrations of (a) 0.05 M, (b) 0.10 M and (c) 0.15 M (d) 0.20 M synthesized at 90⁰ C for 2 hours.

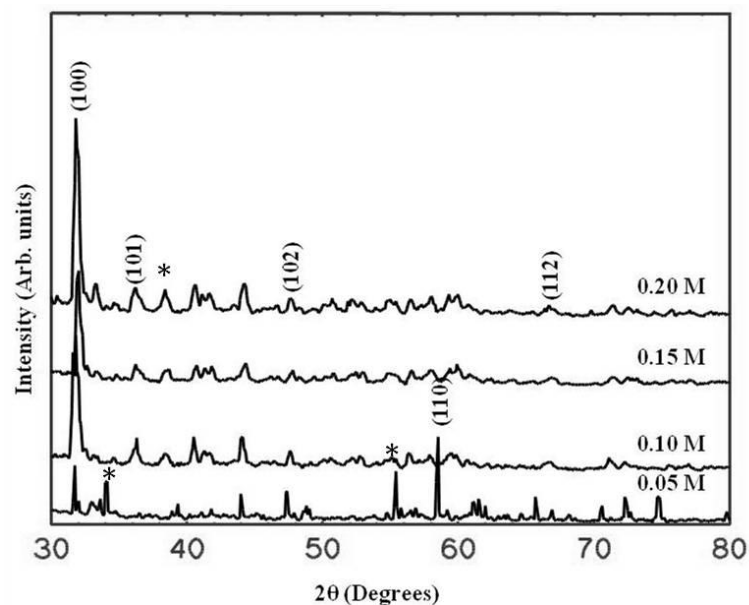


Figure 4.18: XRD pattern of ZnO nanoparticles.

4.4.2 Photoluminescence analysis of ZnO nanoparticles

Figure 4.19 shows the visible PL spectra for the ZnO-NPs synthesized at different Zn acetate concentrations. The overlapping broad peaks were fitted with Gaussian curves. The results are summarized in Table 4.6. Considering the sample synthesized at 0.05 M zinc acetate concentration, peak at 451.5 nm can be attributed to ionized oxygen vacancy [121, 122]. This peak was also present in other samples seemed to be slightly re-shifted with increasing zinc acetate concentration. Peak at about 490 nm was attributed to transition from oxygen vacancy [117] which was also present in all samples but showed a trend of being blue-shifted with increasing zinc acetate concentration. Peak at about 535 nm was attributed to transition from hole trapped at the doubly ionized oxygen vacancy [118]. Lastly, PL peak at about 580 nm was due to oxygen interstitials [120] was present in all samples except at zinc concentration of 0.2 M where a peak attributed to hydroxyl group was observed at 592 nm and it is attributed to structural defect, single ionized vacancy and impurities [122, 123]. Broad yellow band has been cited in many studies due to the fact it is

commonly observed in sample grown by solution methods. Study reveals this band may be attributed to the presence of hydroxyl groups [119].

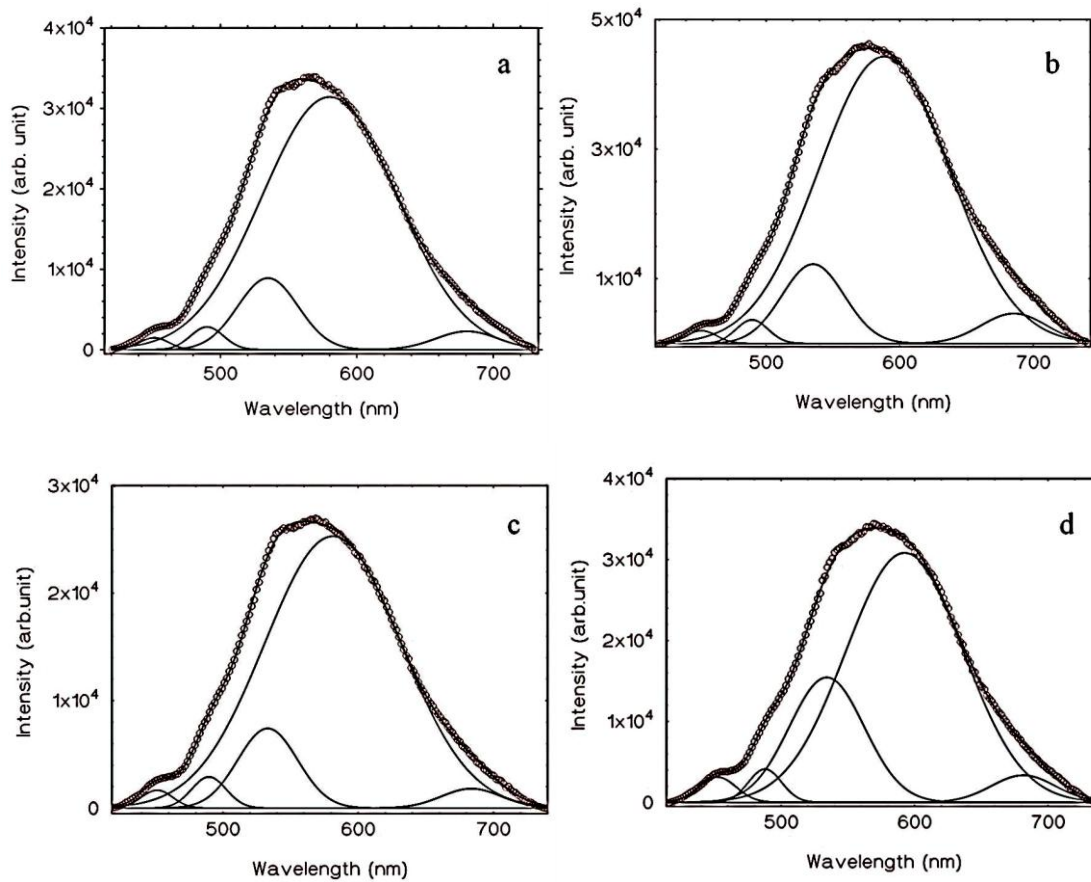


Figure 4.19: PL spectra in the yellow green region fitted to Gaussian curves for samples synthesized using Zn acetate dehydrate at concentration of a) 0.05M, b) 0.10M, c) 0.15M and d) 0.20M.

Table 4.6: The PL peaks for ZnO samples synthesized at different zinc acetate concentration.

Zn Acetate concentration	PL peak (nm)	Proposed transition	Refs.
0.05 M	451.484	Ionized oxygen vacancies	121,122
	490.178	Oxygen vacancy	117
	534.837	hole trapped at V_o^{**}	118
	579.979	oxygen interstitials	120
0.10 M	451.693	Ionized oxygen vacancies	121,122
	489.474	Oxygen vacancy	117
	535.176	hole trapped at V_o^{**}	118
	588.357	oxygen interstitials	120
0.15 M	451.422	Ionized oxygen vacancies	121,122
	489.667	Oxygen vacancy	117
	533.125	hole trapped at V_o^{**}	118
	581.249	oxygen interstitials	120
0.20 M	452.374	Ionized oxygen vacancies	121,122
	487.855	Oxygen vacancy	117
	534.147	hole trapped at V_o^{**}	118
	592.496	hydroxyl groups	119

4.4.3 Effect of pH values on the fabricated ZnO nanostructures

The influence of pH values on the morphology of ZnO nanostructures has also been investigated. The pH value of the solution was adjusted by the addition of sodium hydroxide (NaOH). After filtered and washed, the white precipitate were dried at 100°C for 6 h. Figure 4.20 shows the FESEM images of ZnO nanostructures at three different pH values. Figure 4.20(a) shows there are only microstructures formed without any specific shape. It was observed that the rods start to grow when the solution pH =7.0 and even more rods grown when the solution pH=9.0. The typical lengths of the grown nanorods in Figure 4.20(c) are 6µm to 10µm. Overall, the growth of nanorods was observed to be longer in basic medium than in acidic or neutral medium. The XRD was run on the samples where amorphous XRD spectrum was appeared for solution pH=5.0. On the other hand, Figure 4.21 shows the XRD spectrum for solution pH= 7.0 and pH=9.0. The XRD patterns indicate there are five main peaks associated with ZnO and peak ZnO (101) dominates the highest intensity. While the peak labelled with star (*) indicate the possibility of Zn(OH)₂. It is observed that the peak intensity for pH=7.0 and pH=9.0 do not gives significance different.

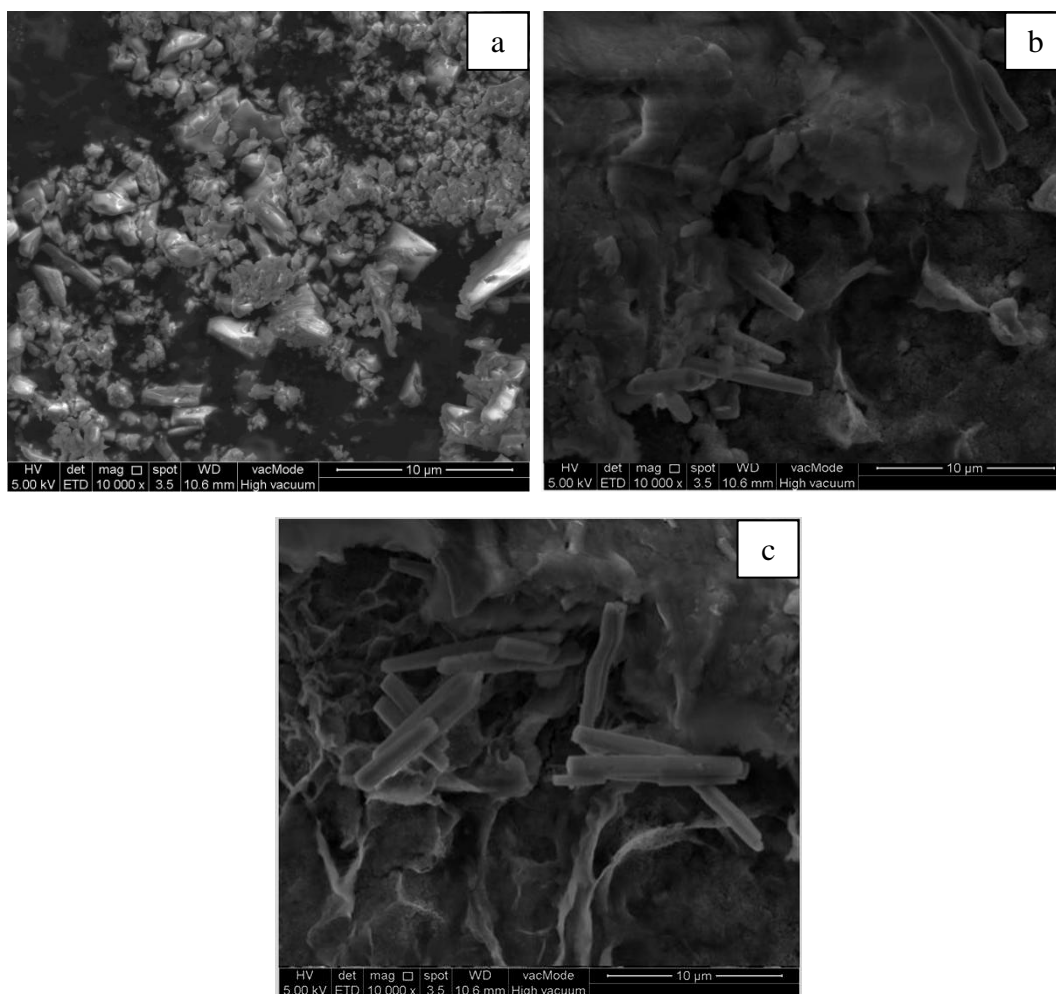


Figure 4.20: FESEM images of unheated ZnO nanostructures synthesized at (a) pH=5.0 and (b) pH=7.0 and (c) pH=9.0 synthesized at 90 ° C for 2 hours. The samples were dried at 100°C for 6 hours.

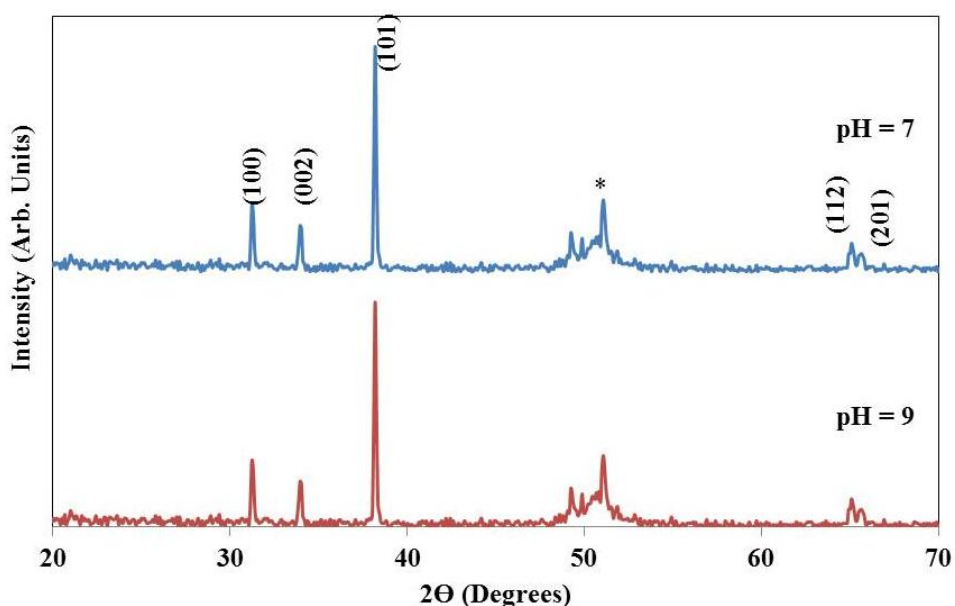


Figure 4.21: XRD patterns of unheated ZnO nanostructures synthesized at pH=7.0 and pH=9.0 at 90 °C for 2 hours.

Further investigations due to the existence of hydroxyl group in the previous samples, the experiments were repeated until final steps. Then, the samples were further heated at 300 °C on the magnetic plate for over 6 hours. Figure 4.22 shows the representative FESEM images of ZnO nanostructures synthesized at different pH values ranging from pH=5.0 to pH=9.0. It can be observed that ZnO nanostructures exhibit similar behaviour in acidic, neutral to alkaline solutions. But the length and diameter varied. In acidic solution (pH = 5.0), the ZnO nanorods have shortest length and diameter. The orientations of the ZnO nanorods are also elsewhere. In alkaline solution (pH=9.0), large straight rods were observed compared to neutral solutions (pH=7.0), the behaviour of the ZnO rods were almost the same except, the nanorods have sharp tips. The aspect ratio of ZnO nanorods is found to increase by raising the pH of solution. The XRD pattern of sol-gel obtained ZnO nanorods at various pH values are shown in Figure 4.23. It is indicated that other XRD pattern of fabricated ZnO nanorods at all different pH values is having similar behaviour.

The main sharp diffraction peaks at $2\theta = \sim 31.6^\circ$, $\sim 34^\circ$, $\sim 36.16^\circ$, $\sim 47^\circ$ and $\sim 62.74^\circ$ fit well with the (100), (002), (101), (102) and (103) planes respectively. The intensity of ZnO (101) peak is at the highest one, which also suggests that the sample exhibits a ZnO(101)-preferred orientation. No characteristic diffraction peaks from other phases or impurities were detected.

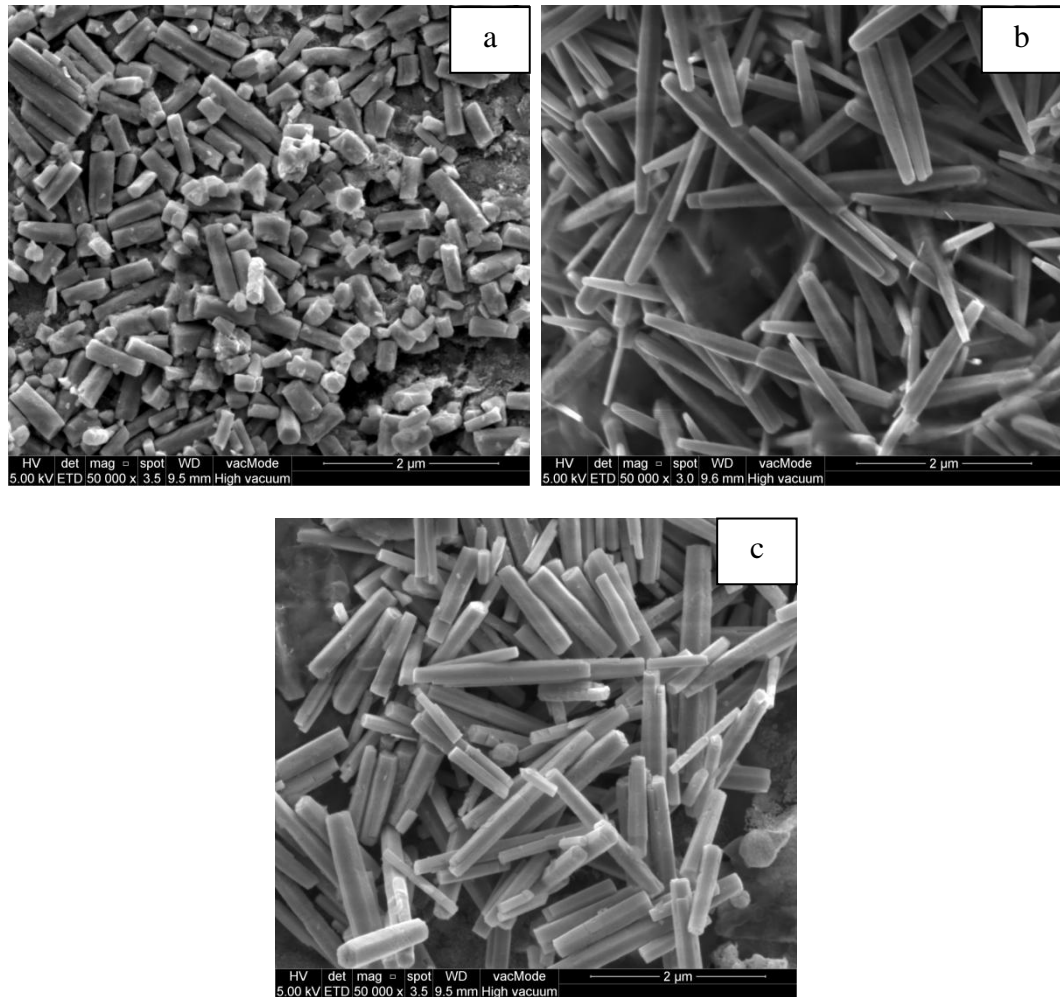


Figure 4.22: The FESEM images of ZnO nanorods using Zinc acetate at (a) pH=5.0 and (b) pH=7.0 and (c) pH=9.0 synthesized at 90°C for 2 hours. The samples were further heated at 300°C on the magnetic plate for over 6 hours.

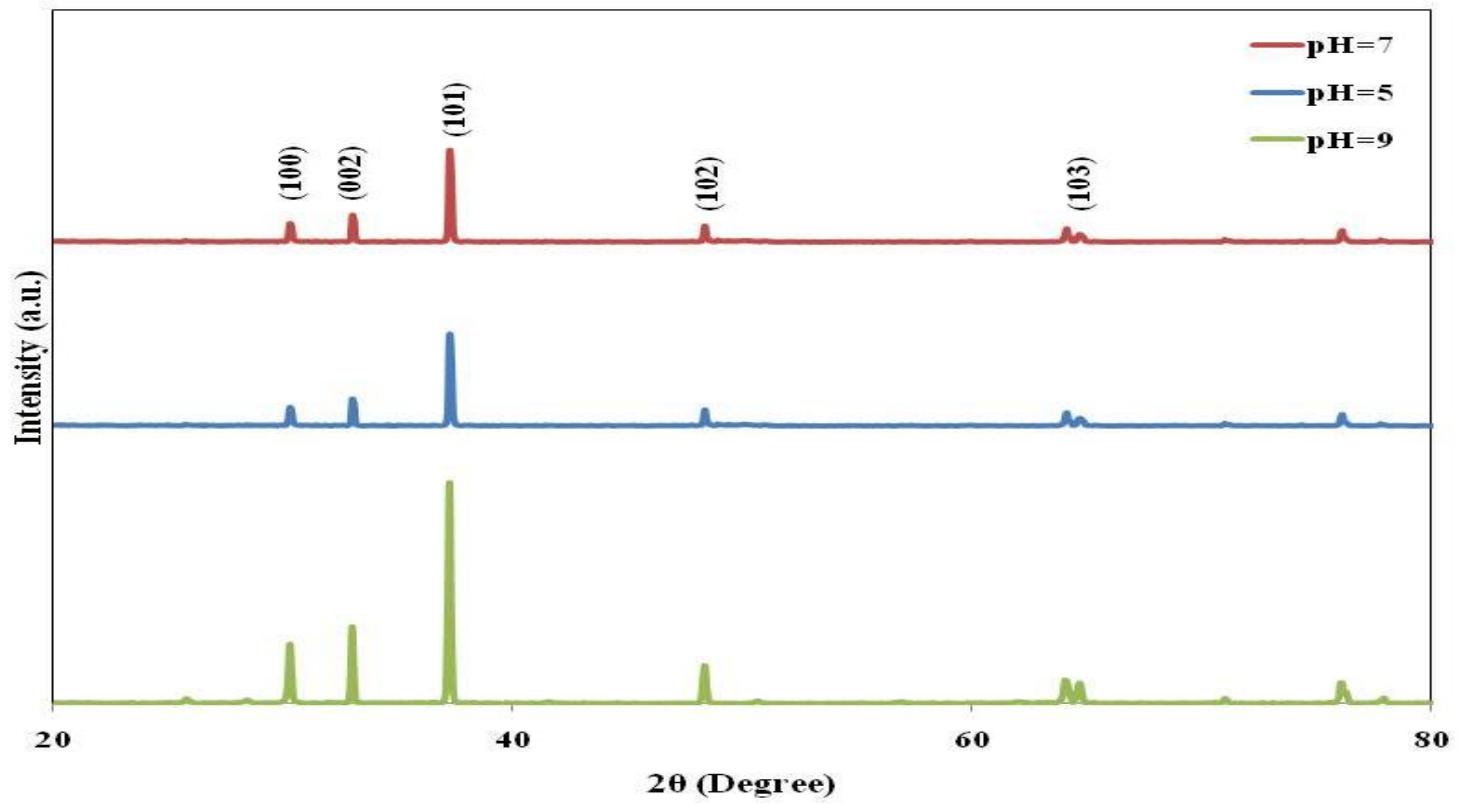


Figure 4.23: XRD pattern of ZnO nanorods

4.5 Summary

The results summarized recent study on SiO₂ and ZnO nanostructures synthesized using carbothermal reduction method. SiO₂ nanowires were synthesized by a direct heating of SiO₂ powders and carbon as silicon source at synthesis temperatures of 900⁰ C, 1000⁰ C and 1100⁰ C and synthesis time of 1 and 2 hours. These SiO₂ nanowires appeared to be inhomogeneous and the orientation is not uniform at low temperatures. While at 1100⁰ C, the nanowires growth was more enhanced with higher yield and more oriented. It was also evident that the usually less number of nanowires were deposited on the substrate if exposed the substrate for a short period of time. In the 1 hour synthesized time, the SiO₂ NWs grows at relatively low density. While the 2 hours synthesis time makes the as-synthesized products formed in high density and most nanowires were entangled with one another that make it hard to estimate the length. Further, the Cu doped SiONWs showed that SiO₂ NWs were randomly dispersed on the surface of silicon wafer.

The above results indicate that Au a high melting point metal serve as an effective catalyst to grow the silicon oxide nanowires using Si wafer and SiO₂ powder as the Si sources. In this mechanism, a liquid eutectic alloy droplet composed of gold and silicone is first formed under the reaction conditions at the evaporation temperature. This liquid droplet served as preferential site for absorption of gas phase reactant and, when supersaturated, the nucleation site for crystallization. Nanowires growth begin after the liquid droplet become supersaturated in reactant material and continues as long as the Au-catalyst alloy remains in a liquid state and the reactant is available. During growth, the Au-catalyst droplet alloy directs the nanowire's growth direction and defines the diameter of the nanowires. Ultimately, the growth terminates when the

temperature is below the eutectic temperature of the catalyst alloy or the reactant is no longer available.

In the same method, ZnO nanostructures were fabricated on the gold coated Si substrate at different deposition temperatures. It can be seen that three kinds of growth morphologies were evident from the different synthesis temperatures. The growth mechanism of the ZnO nanostructures is proposed to be the reduction of ZnO powders by graphite, vapour formation and re-combinations of ZnO vapors to form a liquid droplet. The ZnO droplets were then transported towards the substrate. The field enhancement factors valued two different gradient associated at each deposition temperatures. The Al doped ZnO nanostructures revealed the rod-like structures formed on the silicon substrate. The average field enhancement factor showed higher value compared to undoped structures.

The other results summarized the recent efforts in using *C.Aurantifolia* extract to grow the ZnO nanoparticles. Zinc oxide nanoparticles were rapidly synthesized by treating zinc ions with the citrus extract. The effect of various process parameters like concentration and pH solutions were studied. An interesting green synthesis method has been developed for the preparation of ZnO nanoparticles. This preparatory method is a novel and cost effective method that excludes the use of external stabilizing/capping agents. At 0.05M to 0.20M concentrations, nanoparticles with nearly spherical shape were produced. Photoluminescence study and XRD analysis showed the crystalline nanoparticles formed with the existence of Zn(OH)₂. While in the pH studied range from 5 to 9, the ZnO nanorods with highly crystalline formed on the substrate.

Chapter 5.0 Conclusions

A variety of SiO₂ and ZnO nanostructures were grown by simple methods, carbothermal reduction and sol gel process. In this work, silicon oxide nanostructures and zinc oxide nanostructures fabricated by carbothermal reduction method and sol gel processing were successfully achieved. It was found that the growth of these nanostructures can be control by various parameters including growth temperature, deposition time, pH and concentration of the solution. The morphological, structural, electrical and optical properties of resultant nanostructures characterized by scanning electron microscopy (SEM), X-ray diffractometry (XRD), energy dispersive X-ray spectroscopy (EDX), field emission electron and Photoluminescence (PL) were well studied.

Silicon oxide nanowires were fabricated by the carbothermal reduction route. The obtained silicon oxide nanowires grown were proportionally with the increment in temperature. It was observed the substrate temperature and synthesis time had considerable effects on the size and density of the nanowires. In this study, we found 1100⁰C substrate temperature to be the best growth temperature with the nanowires growth was more enhanced with the highest yield and more oriented. While the 2 hours synthesis time makes the nanowires grow at higher density compared with 1 hour. Meanwhile, the Cu-doped silicon oxide nanowires were randomly growth on the silicon surface. The formations of nanowires on the surface are much denser compared with the undoped SiO₂ NWs discussed earlier.

ZnO nanostructures growth by cabothermal reduction method was successfully fabricated. Variation of temperatures ranging from 900 to 1100⁰ C showed the morphologies of ZnO changed from thin film to ellipsoidal shapes. From the field emission studies, the enhancement factor, β values were observed to be increased if the

temperature increases, although that was only slightly increased. This is due to the factors such as emitter diameter, length of nanostructures and also the orientation of nanostructures. In this case, it is believed due to the change in morphology from rod-like to ellipsoidal shapes which having sharp tips at the end of the structures. The stability for field emission was measured from current-time behaviour. The current for all samples looked similar without any tremendous decrease in current for about 20 minutes. On the other hand, Al-doped ZnO nanostructure was synthesized using the same procedure. The rod-like nanostructures grow on the substrate surface which was much denser than undoped ZnO nanostructures compared at the same temperature. The field electron emission values were recorded. The average enhancement factor value for Al-doped ZnO nanorods shows slightly increment in the value which was 363.9 and the turn on field were reduced to 37 V/ μm

The effect of concentration and pH values were studied using sol gel processing by using *C.Aurantifolia* extract for the first time. ZnO nanostructures fabricated using different concentrations of zinc acetate dehydrate and *Citrus Aurantifolia* extract were successfully fabricated. However, the XRD patterns showed the existence of Zn(OH)_2 on the sample surfaces. From low solution concentrations, a non-uniform surface morphology was clearly observed, while synthesis from solution with higher concentrations enables fabrication of nanoparticles. The PL spectra at room temperature showed a yellow green region with slightly re-shifted. In the last part of these works, the pH values were changed at three different conditions; acidic, neutral and basic. The ZnO nanostructures changed into nanorods and the length changed with the pH condition. Further investigations from the existence of hydroxyl group, the variation of pH values have been repeated until last steps. But, the experiments were elongated to further heat the samples at 300°C on the magnetic plate. It was found that, clear ZnO nanorods formed with good crystal quality as confirmed from the XRD analysis. The

solution concentrations and pH values were significantly affect obtained morphology of the ZnO nanostructures. In future research, the following strategies can be followed. As ZnO possess different kinds of morphologies, it properties can further studies in an application like nanosensors. The biosynthetic method using *C.Aurantifolia* extract in this dissertation can be adopted for other kinds of plant extract such as lemongrass and other types of lemon. The mechanism of the nanostructures grow can be further derived. Thus, the application can be well studied.

REFERENCES

- [1] Lu, W., and Lieber, C. M. (2007). Nanoelectronics from the bottom up. *Nature Materials*, 6 (11), 841-850.

- [2] Huang, M. H., Mao, S., Feick, H., et al. (2001). Room-temperature ultraviolet nanowire nanolasers. *Science*, 292 (5523), 1897- 1899.

- [3] Qian, F., Li, Y., Gradečak, S., Wang, D., Barrelet, C. J., and Lieber, C. M. (2004). Gallium nitride-based nanowire radial heterostructures for nanophotonics. *Nano Letters*, 4 (10), 1975-1979.

- [4] Qin, L. C., Zhao, X., Hirahara, K., Miyamoto, Y., Ando, Y., and Iijima, S. (2000). Materials science: the smallest carbon nanotube. *Nature*, 408 (6808), 50.

- [5] Wang, Tang, Z. K., Li, G. D., and Chen, J. S. (2000). Materials science: single-walled 4Å carbon nanotube arrays. *Nature*, 408 (6808), 50–51.

- [6] Majidi, C., Chen, Z., Srolovitz, D.J., Haataja, M. (2010). Spontaneous bending of piezoelectric nanoribbons: Mechanics, polarization, and space charge coupling. *Journals of the Mechanics and Physics of Solids*. 58, 73-85.

- [7] Sze, S. M., and Ng, K. K. (2006). *Physics of Semiconductor Devices*. New York, NY, USA: John Wiley & Sons.

- [8] Lengyel, I., Jensen, K.F. (2000). A chemical mechanism for in situ Boron doping during silicon chemical vapour deposition. *Thin Solid Films*. 365, 231-241.

- [9] Meng, G.W., Peng, X.S., Wang Y.W., Wang C.Z., Wang X.F., Zhang L.D. (2003). Synthesis and photoluminescence of aligned SiO_x nanowires arrays. *Applied Physics A*, 76, 119.

- [10] Liu Z.Q., Xie S.S., Sun L.F., Tang D.S., Zhou W.Y., Wang C.Y., Liu W., Liu Y.B., Zou X.P., Wang G. (2001). Synthesis of alpha-SiO₂ nanowires using Au nanoparticles catalysts on a silicon substrate. *Journal of Materials Research*, 16, 683.
- [11] Chen, Y. J., Li J. B., Dai, J. H. (2001). Si and SiO_x nanostructures formed via thermal evaporation. *Chemical Physics Letter*, 344, 450.
- [12] Pan, Z. W., Dai, S., & Lowndes, D. H. (2005). Gallium-catalyst SiO nanowires growth. *Tsinghua Science and Technology*, 10, 718-728.
- [13] Song, J., Lee, G., & Ajmera, P. (1995). Chemical and electrical characteristics of low temperature plasma enhanced CVD silicon oxide films using Si,H, and N₂O. *Thin Solid Films*, 270, 512-516.
- [14] Duraia, M. E.-S., Mansurov, Z.A., Tokmolden, S., & Beall, G. W. (2010). Preparation of highly aligned silicon oxide nanowires with stable intensive photoluminescence. *Physica B*, 40, 1176–1180.
- [15] Zhang, L., Xie, W., Wu, Y., Xing, H., Li, A., Zheng, W., et al. (2003). Optical and surface properties of SiO₂ by flame hydrolysis deposition for silica waveguide. *Optical Materials*, 22, 283–287.
- [16] Liu, W.L., Hsieh, S.H., Chen, C.H., Chen, W.J. (2009). Effect of Fe metal on the growth of Silicon oxide nanowires. *Journal Minerals, Metallurgy and Materials*, 3 (16), 317
- [17] Fan, D. H., Zhu, Y. F., Shen W. Z., Lu J. J. (2008). Synthesis and optical properties of hierarchical pure ZnO nanostructures. *Materials Research Bulletin*, 43, 3433–3440.
- [18] Morkoc, H., Carlo, A. D., & Cingolani, R. (2002). GaN-based modulation doped FETs and UV detectors. *Solid-State Electronics*, 46, 157–202.

- [19] Kim, J., Jeong, H., & Park, J.-Y. (2013). Patterned horizontal growth of ZnO nanowires on SiO₂ surface. *Current Applied Physics* , 13, 425-429.
- [20] Baltazar-Rodrigues, J., Lima, J. D., Campos, C., & Grandi, T. (2009). Temperature effects on mechanically alloyed nanometric ZnSe powder. *Powder Technology* , 189, 70–73.
- [21] Kamalasanan, M.N and Chandra, S. (1996). Sol-gel synthesis of ZnO thin films. *Thin Solid Films*, 288, 112-115.
- [22] Paraguay, F. D., Estrada, W. L., Acosta, D. R. N., Andrade, E., and Miki-Yoshida, M. (1999). Growth, structure and optical characterization of high quality ZnO thin film obtained by spray pyrolysis. *Thin Solid Films*, 350, 192.
- [23] Funakubo, H., Mizutani, N., Yonetsu, M., Saiki, A. and Shinozaki, K. (1999). Challenger in fabrication and testing of piezoelectric MEMS with a particular focus on energy harvesters. *Journal of Electroceramics*, 4 (S1), 25.
- [24] Sakurai, K., Kanehiro, M., Nakahara, K., Tanabe, T., Fujita, S. (2000). Effect of oxygen plasma condition on MBE growth of ZnO. *Journal of Crystal Growth*. 209, 522.
- [25] Zhai, T.Y, Fang, S.H., Liao, M.Y., Xu, X.J., Zeng, H.B., Yoshio, B., Golberg, D. (2009). A comprehensive review of one-dimensional metal oxide nanostructures photodetectors. *Sensor*, 9, 6504-6529; doi:10.3390/s90806504.
- [26] Liu, J. Z., Yan, P. X., Yue, G. H., Chang, J. B., Zhuo, R. F., Qu D. M. (2006). Controllable synthesis of undoped/Cd-doped ZnO nanostructures. *Materials Letters*, 60, 3122–3125.

- [27] Lotus, A., Kang, Y., Walker, J., Ramsier, R., & Chasea, G. (2010). Effect of aluminum oxide doping on the structural, electrical, and optical properties of zinc oxide (AOZO) nanofibers synthesized by electrospinning. *Materials Science and Engineering B* , 166, 61–66.
- [28] Cheng, J. P., Zhang, X. B., Luo, Z. Q. (2008). Oriented growth of ZnO nanostructures on Si and Al substrates. *Surface & Coatings Technology*, 202, 4681–4686.
- [29] Wu, C. L., & Huang, Q. L. (2012). Synthesis of Na-doped ZnO nanowires and their photocatalytic properties. *Journal of Luminescence* , 130, 2136–2141.
- [30] Chen, L.L., Ye, Z.Z., Lu, J.G., He, H.P., Zhao, B.H., Zhu, L.P., Paul, K.C., Shao, L. (2006). Co-doping effect and electrical transport in In-N dope ZnO. *Chemical Physics Letters*, 432, 352-355.
- [31] Lee, W., Jeong M.C., Myoung, J.M. (2004). Optical characteristics of Arsenic-doped ZnO nanowires. *Applied Physics letters*, 25, 85.
- [32] Marzouki, A., Falyouni, F., Haneche, N., Lusson, A., Galtier, P., Rigutti, L., Jacopin, G., Tchernycheva, M., Oueslati, M., Sallet, V. (2010). Structural and optical characterizations of nitrogen-doped ZnO nanowires grown by MOCVD. *Materials Letters*. 64, 2112–2114.
- [33] Ilıcan, S., Caglar, Y., Caglar, M., Demirci, B. (2008). Polycrystalline indium-doped ZnO thin films: preparation and characterization. *Journal of optoelectronics and advanced materials*. 10 (10), 2592-2598.
- [34] Chahmat, N., Haddad, A., Ain-Souya, A., Ganfoudi, R., Attaf, N., Aida, M. S., et al. (2012). Effect of Sn Doping on the Properties of ZnO Thin Films Prepared by Spray Pyrolysis. *Journal of Modern Physics*, 3, 1781-1785.
- [35] Suri, P., Panwar, M., Mehra, R. M. (2007). Photovoltaic performance of dye-sensitized ZnO solar cell based on eosin-Y photosensitizer. *Materials Science—Poland*, 25(1), 137–144.

- [36] Lupan, O., Shishiyanu, S., Ursaki, V., Khallaf, H., Chow, L., Shishiyanu, T., Sontea, V. (2009). Synthesis of nanostructured Al-doped zinc oxide films on Si for solar cells applications. *Solar Energy Materials & Solar Cells*. 93, 1417–1422.
- [37] Folwer, R.H. and Nordheim, L. (1928) Electron emission in intense electric fields. *Proceeding of Royal Society of London, Series A*, **119**, 173–181.
- [38] Spindt, C., Holland, C. E., Rosengreen, A. & Brodie, I. (1991). Field emitter array development for gigahertz operation, *Proceeding of IEEE Transation on Electron Devices ED- 38*, ISBN 0018-9383, San Francisco, CA.
- [39] Stratton, R. (1962). Theory of Field Emission from Semiconductors. *Physical Review*, 125 (1) 67-82.
- [40] Baskin, L. M., Lvov, O. L., & Fursey, G. N. (1971). General features of field emission from semiconductors. *Physica Status Solidi (b)*, 47(1) 49-62.
- [41] Forbes, R. G. & Deane, J. H. B. (2007). Reformulation of the standard theory of Fowler-tunneling and cold field electron emission. *Proceeding of Royal Society A.*, 463, 2907-2927.
- [42] Edgcombe, C.J. and Valdr` e, U. (2001) Microscopy and computational modelling to elucidate the enhancement factor for field electron emitters. *Journal of Microscopy*, 203, 188–194.
- [43] Forbes, R. G. (2001). Low-macroscopic-field electron emission from carbon films and other electrically nanostructured heterogeneous materials: hypotheses about emission mechanism. *Solid-State Electronics*, 45, 6, 779-808.
- [44] Qin, X-Z., Wang, W-L., Xu, N-S., Bing, Z. & Forbes, R. G. (2011). Analytical treatment of cold field electron emission from a nanowall emitter, including quantum confinement affects. *Proceeding of Royal Society A*, 467, 2128, 1029-1051, ISSN 1471-2946.
- [45] Lin, C-C., Chang, K-C., Pan, F-M., Kuo, C-T., Liu, M., Mo, C-N. (2007). Growth of carbon nanotube field emitters in the triode structure using anodic aluminum oxide as the template. *Diamond & Related Materials*. 16, 1388–1392.

- [46] Chen, J., Lei, W., Chai, W., Zhang, Z., Li, C., Zhang, X. (2008). High field emission enhancement of ZnO-nanorods via hydrothermal synthesis. *Solid-State Electronics*, 52, 294–298.
- [47] Zhang, G., Wei, L., Chen, Y., Mei, L., Jiao, J. (2013). Field emission property of ZnO nanoneedle arrays with different morphology. *Materials Letters*. 96, 131–134.
- [48] Mosquesra, E., Bernal, J., Zarate, R.A., Mendoza, F., Katiyar, R.S., Morell, G. (2013). Growth and electron field-emission of single-crystalline ZnO nanowires. *Materials Letters* 93, 326–329.
- [49] Ramanathan, S., Chen, Y. C., Tzeng, Y. H. (2010). Zinc oxide nanowire based field emitters. *Physica E*, 43, 285–288.
- [50] Le, H. Q., Goh, G. K., Teng, J. H., Chew, A. B., & Lim, S. K. (2012). Solution epitaxy of patterned ZnO nanorod arrays by interference lithography. *Progress in Crystal Growth and Characterization of Materials* , 58,135–144.
- [51] Marine, W., Patrone, L., Luk'yanchuk, B., Sentis, M. (2000). Strategy of Nanocluster and Nanostructure Synthesis by Conventional Pulsed Laser Ablation. *Applied Surface Science*, 154–155, 345 –52.
- [52] Qin, W. J., Sun, J., Yang, J., & Du, X. W. (2011). Control of Cu-doping and Optical Properties of ZnO Quantum Dots by Laser Ablation of Composite Targets. *Materials Chemistry and Physics*, 130, 425– 430.
- [53] McLoughlin, C., Hough, P., Costello, J., McGlynn, E., & Mosnier, J. (2009). Growth and field emission properties of ZnO nanostructures deposited by a novel pulsed laser ablation source on silicon substrates. *Ultramicroscopy* , 109, 399–402.
- [54] Chao, L. C., Tsai, D. Y., & Shih, Y. R. (2009). ZnO thin films deposited by capillaritron ion beam sputtering deposition. *Nuclear Instruments and Methods in Physics Research B* , 267, 2874–2877.
- [55] Hernández-Fenollosa, M., López, M., Donderis, V., González, M., Marí, B., & Ramos-Barrado, J. (2008). Role of precursors on morphology and optical

properties of ZnS thin films prepared by chemical spray pyrolysis. *Thin Solid Films*, 516, 1622–1625.

- [56] León, J. O.-R., Acosta, D., Pal, U., & Castañeda, L. (2011). Improving electrochromic behavior of spray pyrolysed WO₃ thin solid films by Mo doping. *Electrochimica Acta* , 56, 2599–2605.
- [57] Muthukumar, S., & Gopalakrishnan, R. (2012). Structural, FTIR and photoluminescence studies of Cu doped ZnO nanopowders by co-precipitation method. *Optical Materials* , 34, 1946–1953.
- [58] Meng, F., Yin, J., Duan, Y. Q., Yuan, Z. H., & Bie, L. J. (2011). Co-precipitation synthesis and gas-sensing properties of ZnO hollow sphere with porous shell. *Sensors and Actuators B* , 156, 703-708.
- [59] Liu, B., Zeng, H.C. (2003). Hydrothermal synthesis of ZnO nanorods in the diameter regime of 50 nm. *Journal of the American Chemical Society*, 125, 4430.
- [60] Wang, J.M., Gao, L. (2003). Wet chemical synthesis of ultralong and straight single-crystalline ZnO nanowires and their excellent UV emission properties. *Journal of Materials Chemistry*, 13, 2551.
- [61] Guo, M., Diao, P., Cai, S.M. (2005). Hydrothermal growth of well-aligned ZnO nanorod arrays: dependence of morphology and alignment ordering upon preparing conditions. *Journal of Solid State Chemistry*, 178, 1864.
- [62] Kiomarsipour, N., & Razavi, R. S. (2013). Hydrothermal synthesis and optical property of scale-and spindle-like ZnO. *Ceramics International*, 39, 813–818.

- [63] Sun, X., Chen, X., Den, Z., & Li, Y. (2002). A CTAB-assisted hydrothermal orientation growth of ZnO nanorods. *Materials Chemistry and Physics* , 78, 99–104.
- [64] Besson, S., Ricolleau, C., Gacoin, T.(2000). A new 3D organization of mesopores in oriented CTAB silica films, *Journal of Physical Chemistry B*, 104, 12095–12097.
- [65] Grosso, D., Balkenende, A. R., Albouy, P.A., Lavergue, M., Mazeriois, L., Babonneak, F. (2000). Highly oriented 3D-hexagonal silica thin films produced with cetyltrimethylammonium bromide, *Journal of Material Chemistry*, 10, 2085–2089.
- [66] Cai, Q., Luo, Z.S., Pang, W.Q., Fan, Y.W., Chen, X.H., Cui, F.Z. (2001). Dilute solution routes to various controllable morphologies of MCM-41 silica with a basic medium, *Chemistry of Material*, 13, 258–263.
- [67] Lim, Y., Park, J., Kim, M., & Kim, J. (2006). Effect of carbon source on the carbothermal reduction for the fabrication of ZnO nanostructure. *Applied Surface Science* , 253, 1601–1605.
- [68] Lee, J. S., Lee, S. H., & Choi, S. C. (2009). Improvement of porous silicon carbide filters by growth of silicon carbide nanowires using a modified carbothermal reduction process. *Journal of Alloys and Compounds* , 467, 543–549.
- [69] Wei, S., Qiang, X. B., Bin, Y., Yan, S. H., Xun, S. J., HeLli, W., et al. (2011). Preparation of TiC powders by carbothermal reduction method in vacuum. *Trans. Nonferrous Metal Society of China* , 21, 185-190.

- [70] Wang, Q., Cong, R., Li, M., Zhang, J., & Cui, Q. (2012). A simple method to synthesize α -Si₃N₄, β -SiC and SiO₂ nanowires by carbothermal route. *Journal of Crystal Growth* , 312, 2133–2136.
- [71] Lim, Y., Park, J., Kim, M., & Kim, J. (2006). Effect of carbon source on the carbothermal reduction for the fabrication of ZnO nanostructure. *Applied Surface Science* , 253, 1601–1605.
- [72] Zhou, Z., Zhan, C., Wang, Y., Su, Y., Yang, Z., & Zhang, Y. (2011). Rapid mass production of ZnO nanowires by a modified carbothermal reduction method. *Materials Letters* , 65, 832–835.
- [73] Wang, J., Sha, J., Yang, Q., Ma, X. y., H. Z., Yu, J., et al. (2005). Carbon-assisted synthesis of aligned ZnO nanowires. *Materials Letters* , 59, 2710 – 2714.
- [74] Xiuhua, P., Zhizhen, Y., Jiesheng, L., Xiuquan, G., Yujia, et al. (2003). Fabrication of Sb doped p-type ZnO thin films by pulsed laser deposition. *Applied Surface Science*, 253, 5067–5069.
- [75] Benelmadjat, H., Touka, N., Harieche, B., Boudine, B. et al. (2010). Study of structural and optical properties of Sb doped ZnO thin films deposited by spin coating method. *Optical Materials*, 32, 764–767.
- [76] Palani, I., Okazaki, K., Nakamura, D., Sakai, K., Higashihata, M., & Okada, T. (2012). Influence of Sb in synthesize of ZnO nanowire using sandwich type substrate in carbothermal evaporation method. *Applied Surface Science* , 258, 3611– 3616.
- [77] Lin, P. F., Ko, C. Y., Lin, W. T., & Lee, C. (2007). Effects of processing parameters on ultraviolet emission of In-doped ZnO nanodisks grown by carbothermal reduction. *Materials Letters* , 61, 1767–1770.

- [78] Alias, S., Ismail, A., & Mohamad, A. (2010). Effect of pH on ZnO nanoparticle properties synthesized by sol-gel centrifugation. *Journal of Alloys and Compounds*, 499, 231–237.
- [79] Ba-Abbad, M. M., Kadhum, A. A., Mohamad, A. B., Takriff, M. S., & Sopian, K. (2013). The effect of process parameters on the size of ZnO nanoparticles synthesized via the sol-gel technique. *Journal of Alloys and Compounds*, 550, 63–70.
- [80] Wang, X.Y., Huang, W.G., Sebastian, P.J., Gamboa, S. (2005). Sol-gel template synthesis of highly ordered MnO₂ nanowire arrays, *Journal Power Sources*, 140, 211.
- [81] Xu, H., Qin, D.H., Yang, Z., Li, H.L. (2003). Fabrication and characterization of highly ordered zirconia nanowire arrays by sol-gel template method. *Materials Chemistry and Physics*, 80, 524.
- [82] Zhang, M., Bando, Y., Wada, K. (2001). Sol-gel template preparation of TiO₂ nanotubes and nanorods, *Journal of Materials Science Letter*, 20, 167.
- [83] Zhou, Y.K., Li, H.L. (2002). Sol-gel template synthesis and structural properties of a highly ordered LiNi_{0.5} Mn_{0.5}O₂ nanowire array, *Journal of Materials Chemistry*, 12, 681.
- [84] Yang, Z., Huang, Y., Dong, B., Li, H.L. (2005). Fabrication and structural properties of LaFeO₃ nanowires by an ethanol-ammonia-based sol-gel template route, *Applied Physics A: Materials Science and Processing*, 81, 453.
- [85] Gardea-Torresdey, J. L., Parsons, J. G., Gomez, E., Peralta-Videa, J., Troiani H. E., Santiago P., Yacaman M. J. (2002). Formation and growth of Au nanoparticles inside live alfalfa plants. *Nanotechnology Letter*, 2(4), 397-401.

- [86] Gardea-Torresdey, J. L., Gomez E., Peralta-Videa J. R., Parsons J. G., Troiani H., Jose-Yacamán M. (2003). Alfalfa sprouts: A natural source for the synthesis of silver nanoparticles. *Langmuir*, 19, 1357-1361.
- [87] Shankar S. S., Ahmad A., Sastry M. (2003). Geranium leaf assisted biosynthesis of silver nanoparticles. *Biotechnology Progress*, 19(6), 1627-1631.
- [88] Shankar S.S, Rai A., Ahmad A., Sastry M. (2004). Rapid synthesis of Au, Ag, and bimetallic Au core-Ag shell nanoparticles using Neem (*Azadirachta indica*) leaf broth. *Journal of Colloid and interface Science*, 275(2), 496-502.
- [89] Shankar,S.S., Rai, A., Ahmad, A., Sastry, M. (2005). Controlling the optical properties of lemongrass extract synthesized gold nanotriangles and potential application in infrared-absorbing optical coatings. *Chemistry of Material*, 17(3), 566-572.
- [90] Canizal G., Schabes-Retchkiman P. S., Pal U., Liu H. B., Ascencio J. A. (2006). Controlled synthesis of ZnO nanoparticles by bioreduction. *Materials Chemistry and Physics*, 97(2-3), 321-329.
- [91] Chandran, S. P., Chaudhary, M., Pasricha, R., Ahmad A., Sastry M. (2006). Synthesis of gold nanotriangles and silver nanoparticles using Aloe vera plant extract. *Biotechnology Progress*, 22(2), 577-583.
- [92] Singh, A., Chaudhari, M., Sastry, M. (2006). Construction of conductive multilayer films of biogenic triangular gold nanoparticles and their application in chemical vapour sensing. *Nanotechnology*, 17(9), 2399-2405.
- [93] Shukla, R., Nune, S. K., Chanda, N., Katti, K., Mekapothula, S., Kulkarni, R. R., Welshons, W.V., Kannan, R., Katti, K. V. (2008). Soybeans as a phytochemical reservoir for the production and stabilization of biocompatible gold nanoparticles. *Small*, 4(9), 1425-1436.
- [94] Anuradha, J., Tasneem, A., Abbasi, S. A. (2010). 'Green' synthesis of gold nanoparticles with aqueous extracts of Neem (*Azadirachta indica*). *Research Journal of Biotechnology*, 5(1), 750-759.
- [95] Anuradha, J., Tasneem, A., Abbasi, S. A. (2011). Rapid and reproducible 'green' synthesis of silver nanoparticles of consistent shape and size using *Azadirachta Indica*. *Research Journal of Biotechnology*, 6(1), 69-70.

- [96] Sneha, K., Sathishkumar, M., Lee, S. Y., Bae, M. A., Yun, Y. S. (2011). Biosynthesis of Au nanoparticles using Cumin seed powder extract. *Journal of Nanoscience and Nanotechnology*, 11(2), 1811-1814.
- [97] Lin, L. Q., Wang, W. T., Huang, J. L., Li, Q. B., Sun, D. H., Yang, X., Wang, H. X., He, N., Wang, Y. P. (2010). Nature factory of silver nanowires: Plant-mediated synthesis using broth of *Cassia fistula* leaf. *Chemical Engineering Journal*, 162(2), 852-858.
- [98] Zargar, M., Azizah Abdul Hamid, Fatimah Abu Bakar, Mariana Nor Shamsudin, et.al. (2011). Green Synthesis and Antibacterial Effect of Silver Nanoparticles Using *Vitex Negundo.L. Molecules*. 16, 6667-6676.
- [99] Lin, L. Q., Wang, W. T., Huang, J. L., Li, Q. B., Sun, D. H., Yang, X., Wang, H. X., He, N., Wang, Y. P. (2010). Nature factory of silver nanowires: Plant-mediated synthesis using broth of *Cassia fistula* leaf. *Chemical Engineering Journal*, 162(2), 852-858.
- [100] Lee, S. W., Musa Najiah. (2009). Antimicrobial Property of 2-Hydroxypropane-1,2,3-Tricarboxylic Acid Isolated from *Citrus microcarpa* Extract. *Agricultural Sciences*. 8 (7), 880-886.
- [101] Loizzo M.R., Tundis R., Bonesi M., Menichini F., De Luca D., Colica C., Menichini F. (2012). Evaluation of *Citrus aurantifolia* peel and leaves extracts for their chemical composition, antioxidant and anti-cholinesterase activities. *Journal of the Science and Food Agricultur*, 92(15), 2960-2967.
- [102] Wang, T.T., Yang, L.B., Zhang, B.C., Liu, J.H. (2010). Extracellular biosynthesis and transformation of selenium nanoparticles and application in H₂O₂ biosensor. *Colloids and Surfaces B*, 80(1), 94-102.
- [103] Krishnaraj, C., Jagan E.G., Rajasekar, S., Selvakumar P., Kalaichelvan, P.T., Mohan, N. (2010). Synthesis of silver nanoparticles using *Acalypha indica* leaf extracts and its antibacterial activity against water borne pathogens. *Colloids and Surfaces B*, 76(1), 50-56.

- [104] Chen, B. J., Sun, X.W., Xu, C.X. (2004). Fabrication of zinc oxide nanostructures on gold-coated silicon substrate by thermal chemical reactions vapor transport deposition in air. *Ceramics International*, 30, 1725–1729.
- [105] Abdulgafour, H. I., Hassan, Z., Al-Hardan, N., Yam, F. K. (2010). Growth of zinc oxide nanoflowers by thermal evaporation method. *Physica B*, 405, 2570–2572.
- [106] Zambom, L. D. S., Mansano, R. D., Mousinha. A. P. (2009). Low temperature deposition of silicon oxide and silicon nitride by reactive magnetron sputtering. *Microelectronics journal* 40, 66-69,
- [107] Mendelsberg, R. J., Kennedy, J., Durbin, S. M., Reeve, R.J. (2008). Carbon enhanced blue–violet luminescence in ZnO films grown by pulsed laser deposition. *Current Applied Physics*, 8, 283–286
- [108] Shi W. S., Zheng, Y. F., Peng, H. Y., Wang N., Lee C. S., Lee S.T. (2000). Laser ablation synthesis and optical characterization of silicon carbide nanowires. *Journal of the American Ceramic Society*, 83 (2000) 3228.
- [109] Xu, H. Y., Wang, H., Zhang, Y. C., He, W. L., Zhu, M. K., Wang, B., Yan, H. (2004). Hydrothermal synthesis of zinc oxide powders with controllable morphology. *Ceramics International* 30, 93–97.
- [110] Kaviya, S., Santhanalakshmi, J., Viswanathan, B., Muthumary, J., Srinivasan, K. (2011). Biosynthesis of silver nanoparticles using citrus sinensis peel extract and its antibacterial activity. *Spectrochimica Acta Part A*, 79, 594–598.
- [111] Ardenne, V. M. (1978). The history of scanning electron microscopy and of the electron microprobe (in German). *Optik*, 50, 177-188.
- [112] Pawley, J.B. (1997). Development of Field-emission Scanning Electron Microscopy for Imaging Biological Surfaces. *Scanning*, 19 (5), 324-336.
- [113] Shen, G., Chen, p. C., Ryu, K., and Zhou, C. W. (2009). Devices and chemical sensing applications of metal oxide nanowires. *Journal of Materials Chemistry*, 19, 828–839.

- [114] Chen, C. H., Chang, S. J., Chang, S. P., Tsai, Y. C., Chen, I. C., Hsueh, C. J., Hsu, C. L. (2010). Enhanced field emission of well-aligned ZnO nanowire arrays illuminated by UV. *Chemical Physics Letters*, 490, 176–179.
- [115] Xiao, J., Zhang, G., Bai, X., Wu, Y., Zhang, W., Zhao, X., Guo, D. (2008). Field emission from zinc oxide nanowire arrays grown directly from brass. *Physica E*, 41, 309–314.
- [116] Maiti, U. N., Ahmed, S. F., Mitra, M. K., Chattopadhyay, K. K. (2009). Novel low temperature synthesis of ZnO nanostructures and its efficient field emission property. *Materials Research Bulletin*, 44, 134–139.
- [117] Chen, X. and Ruof, R. F. (2007). Simple and Catalyst-free synthesis of silicon oxide nanowires and nanocoils. *NANO: Briefs report and Review*. Vol.2, No.2, 91-95.
- [118] Dupre, L., Buttard, D., Leclere, C., Renevier, H., Gentile, P. (2012). Gold contamination in VLS-grown Si nanowires: Multiwavelength anomalous Diffraction investigations. *Chemistry of Materials*, 24, 4511-4516.
- [119] Zhu, Z., Chen, T.L., Gu, Y., Warren, J., Richard, M.O. (2005). ZnO Nanowires grown by Vapor-phase transport using Selected Metal Catalysts: A comparative Study. *Chemistry of Material*, 17, 4227-4234.
- [120] Lingjie, W., Zunxian, Y., Jinyang, L., Tailiang, G. (2011). Influence of Morphologies on the Field Emission Performance of oriented ZnO nano-arrays. *Chinese Institute of electronics*, 12, 32.
- [121] Singh, J., Kumar, P., Late, D.J., Singh, T., more, M.A., Joag, D.A., Tiwari, R.S., Hui, K.S., Hui, K.N., Srivastave, O.N. (2012). Optical and field emission properties in different nanostructures of ZnO. *Digest Journal of Nanomaterials and Biostructures*, 7 (2), 795-806.
- [122] Xu, C.X., Sun, X.W. (2003). Field emission from ZnO Nanopins. *Applied Physics Letter*, 83 (18), 3806-3808.

- [123] Cao, B.Q., Teng, X.M., Heo, S.H., Li, Y., Cho, S.O., Li, G.H. and Cai, W.P. (2007). Different ZnO nanostructures Fabricated by a seed layer assisted electrochemical route and their photoluminescence and field emission properties. *Journal of Physical Chemistry, C* 111, 2470-2476.
- [124] Lee, C.J., Lee, T.J., Lyu, S.C., Zhang, Y., Ruh, H. and Lee, H.J. (2004). Field emission from well-aligned zinc oxide nanowires grown at low temperature. *Applied Physic Letter*, 81, 3648-3650.
- [125] Liu, J.P., Huang, X.T., Li, Y.Y., Ji, X.X., Li, Z.K., He, X., Sun, F.L. (2007). Vertically aligned 1-D ZnO nanostructures on bulk alloy substrates: Direct solution synthesis, photoluminescence, and field emission. *Journal Physical Chemistry*, 111, 4990-4997.
- [126] Banerjee, D., Jo, S.H. and Ren, Z.F. (2004). Enhanced field emission of ZnO nanowires. *Advance Materials*, 16, 2028-2032.
- [127] Park, C.J., Choi, D.K., Yoo, J.Y., Yi, G.C. and Lee, C.J. (2007). Enhanced field emission properties from well-aligned zinc oxide nanoneedles grown on the Au/Ti/n-Si substrate. *Applied Physics Letter*, 90, 083107.
- [128] Shalaka, C. N., Farid, J.S., Sandip, S.P., Imtiaz, S.M., Dilip, S.J., Mahendra, A.M., Suresh, W.G. (2009). Field emission properties of Al-doped ZnO nanostructures. *Journal of Nano Research*. 5, 213-237.
- [129] Dubey, K.K., Kumar, D. and Kamaldeep. (2012). Optimization of zinc oxide nanoparticles synthesis to fabricate glucose oxidase sensor. *Advances in Applied Sciences Research*, 3, 3081-3088.